



AFRL-AFOSR-CL-TR-2016-0011

Towards natural transition in compressible boundary layers

Marcello Faraco de Medeiros
FUNDACAO PARA O INCREMENTO DA PESQUISA E APEFEICOAMENTO IN

06/29/2016
Final Report

DISTRIBUTION A: Distribution approved for public release.

Air Force Research Laboratory
AF Office Of Scientific Research (AFOSR)/ IOS
Arlington, Virginia 22203
Air Force Materiel Command

REPORT DOCUMENTATION PAGE				Form Approved OMB No. 0704-0188	
<p>The public reporting burden for this collection of information is estimated to average 1 hour per response, including the time for reviewing instructions, searching existing data sources, gathering and maintaining the data needed, and completing and reviewing the collection of information. Send comments regarding this burden estimate or any other aspect of this collection of information, including suggestions for reducing the burden, to the Department of Defense, Executive Service Directorate (0704-0188). Respondents should be aware that notwithstanding any other provision of law, no person shall be subject to any penalty for failing to comply with a collection of information if it does not display a currently valid OMB control number.</p> <p>PLEASE DO NOT RETURN YOUR FORM TO THE ABOVE ORGANIZATION.</p>					
1. REPORT DATE (DD-MM-YYYY) 27-06-2016		2. REPORT TYPE Final		3. DATES COVERED (From - To) 30-29-2011 to 29-03-2016	
4. TITLE AND SUBTITLE Towards natural transition in compressible boundary layers				5a. CONTRACT NUMBER	
				5b. GRANT NUMBER FA9550-11-1-0354	
				5c. PROGRAM ELEMENT NUMBER	
6. AUTHOR(S) Marcello A. Faraco de Medeiros Germán Andrés Gaviria Martínez				5d. PROJECT NUMBER	
				5e. TASK NUMBER	
				5f. WORK UNIT NUMBER	
7. PERFORMING ORGANIZATION NAME(S) AND ADDRESS(ES) University of São Paulo Rua da Reitoria 1009, Butantã, São Paulo ± SP CEP 05508-900 - Brazil				8. PERFORMING ORGANIZATION REPORT NUMBER	
9. SPONSORING/MONITORING AGENCY NAME(S) AND ADDRESS(ES) Air Force Office of Scientific Research 875 N Randolph St., Ste 325 Arlington, VA 22203 James M. Fillerup				10. SPONSOR/MONITOR'S ACRONYM(S) AFOSR/NA and AFOSR/SOARD	
				11. SPONSOR/MONITOR'S REPORT NUMBER(S)	
12. DISTRIBUTION/AVAILABILITY STATEMENT DISTRIBUTION STATEMENT A. Approved for public release; distribution is unlimited					
13. SUPPLEMENTARY NOTES					
14. ABSTRACT See report					
15. SUBJECT TERMS Wave packet, compressible boundary layer, subsonic flow, nonlinear instability, secondary instability, transition to turbulence, direct numerical simulation, white noise					
16. SECURITY CLASSIFICATION OF:			17. LIMITATION OF ABSTRACT	18. NUMBER OF PAGES 109	19a. NAME OF RESPONSIBLE PERSON Marcello A. Faraco de Medeiros
a. REPORT	b. ABSTRACT	c. THIS PAGE			19b. TELEPHONE NUMBER (Include area code) +55 (0)16 3373 8377

Final report
Towards natural transition in compressible boundary layers

Principal Investigator: Marcello Augusto Faraco de Medeiros
Email: marcello@sc.usp.br

Investigator: Germán Andrés Gaviria Martínez
Email: 4ndres.gaviria@gmail.com

Universidade de São Paulo, Brazil

Grant number: FA9550-11-1-0354
June 2016

Abstract

This final report concerns the results obtained in the project titled: "Towards natural transition in compressible boundary layers", with Grant number FA9550-11-1-0354-P00002, in the period 30-09-2011 to 29-03-2016, with Dr. James M. Fillerup serving as program manager.

In this project, a DNS code was developed to investigate problems on transition in compressible boundary layer on a flat plate. Code validation test were performed for linear and nonlinear stages of transition, in incompressible and compressible regimes. The focus of the present work is to investigate natural transition in compressible subsonic boundary layer modeled by wave packets; and perform a preliminary study of transition generated by white noise.

Three main problems were considered, namely, numerical simulation of the experiment [54] on incompressible boundary layer, the influence of compressibility on wave packet evolution at subsonic Mach numbers and finally, a preliminary study of the evolution of a white noise perturbation in the boundary layer at Mach 0.2 and 0.9.

Comparison between numerical and experimental results [54] are in remarkably good agreement in the linear and nonlinear stages, in both, spatial and Fourier spaces. Simulation of this experiment and the analysis carried out for wave packets in the incompressible boundary layer is not available in the literature. The nonlinear modal analysis performed established definitely the existence of tuned fundamental and subharmonic resonance of H-type and K-type in the packet.

Influence of compressibility in wave packet evolution was here investigated in the boundary layer at Mach 0.7 and Mach 0.9. There are no works reported in the literature on wave packets in compressible subsonic boundary layer. In the linear regime, the oblique modes were the most unstable at Mach 0.9. In the nonlinear regime, strong streaks were observed, associated with low frequency modes that eventually decay downstream. An isolated wave packet at Mach 0.9 presents nonlinear amplification only in the subharmonic band, which may be associated to H-type or detuned resonance. However this packet has a relatively stable character. On the other hand, at Mach 0.9 spanwise interaction of wave packet pairs is more unstable than the isolated case. This scenario evidenced the presence of oblique transition.

Finally, the nonlinear evolution of the same white noise disturbance at Mach 0.2 and Mach 0.9 were observed to be completely different. In the incompressible boundary layer localized lambda vortex structures were observed, that could be associated to the local presence of H-type and/or K-type resonance. In the compressible regime, longitudinal vortex structures distributed across the entire domain seemed to be linked to oblique transition. In the white noise evolution, compressibility seems to have a stronger effect than in the wave packet evolution. In the conditions considered, the wave packet interaction appear to be a better representation of white noise compressible transition scenario.

Publications related: 1. An accepted paper [48] 2. Accepted paper in 46th AIAA Fluid Dynamics Conference, AIAA Aviation and Aeronautics Forum and Exposition 2016. 3. Papers with the complete results obtained for incompressible and compressible boundary layer, are in preparation for submission.

I certified that there were no subject inventions during the performance of this work to declare. The U.S. Government is authorized to reproduce and distribute reprints for government purpose notwithstanding any copyright notation thereon. The view and conclusions contained herein are those of the authors and should not be interpreted as necessarily representing the official policies or endorsements, either expressed or implied, of the Air Force Office of Scientific Research or the U.S. Government.

Contents

1	Introduction	3
1.1	Relevance	3
1.2	Transition routes	4
1.3	Wave packets and natural transition	8
1.3.1	DNS simulations of wave packets	8
1.4	Objectives of this work	9
1.5	Structure of the Report	10
2	Physical problem and computational setup	11
2.1	Governing equations	11
2.2	Numerical Methods	12
2.2.1	Discretization	12
2.2.2	Compact finite differences	13
2.2.3	Numerical Stability	15
2.2.4	Filter	15
2.2.5	Grid stretching	16
2.2.6	Boundary Conditions	16
2.2.7	Moving Frame 3D	19
2.3	Parallelization	20
2.3.1	Perform analysis	21
3	Code validation	25
3.1	Base flow generation	25
3.1.1	Boundary layer profiles	25
3.2	Hydrodynamic instability tests	28
4	DNS simulation of experimental wave packet in an incompressible boundary layer	33
4.1	Numerical set-up	33
4.1.1	Choice of reference experiment	33
4.2	Disturbance Generation	34
4.2.1	Grid independence tests	37
4.3	DNS results	39
4.3.1	Linear wave packet	39
4.3.2	Comparison of numerical with experimental wave packet	39
4.4	Nonlinear modal analysis of DNS results	46
4.4.1	Subharmonic bands	46
4.4.2	Fundamental bands	52

4.5	Effective experimental conditions	55
4.5.1	Pressure gradient	55
4.5.2	Amplitude calibration	57
4.5.3	Amplitude effect	58
4.6	Seed	59
5	Wave packet in subsonic boundary layer	61
5.1	Numerical set-up	61
5.2	Wave packet in a boundary layer at Mach 0.7	62
5.2.1	Linear wave packet	62
5.2.2	Nonlinear wave packet	63
5.2.3	Amplitude effect	67
5.2.4	Phase locking	69
5.3	Wave packet in a boundary layer at Mach 0.9	70
5.3.1	Linear wave packet	70
5.3.2	Nonlinear wave packet	74
5.4	Interaction between wavepackets in a boundary layer at Mach 0.9	79
5.4.1	Pair of wave packets separated by $d = 30$	79
5.4.2	Pair of wave packets separated by $d = 60$	83
6	Transition generated by white noise	88
6.1	Generation of white noise disturbance	88
6.2	White noise evolution at Mach 0.2	89
6.3	White noise evolution at Mach 0.9	93
7	Conclusions and remarks	97
7.1	Conclusions	97
7.2	Suggested work	98
	References	99

Chapter 1

Introduction

Natural transition is the term coined in literature [34, 16] to refer the transition to turbulence process as it occurs in real (uncontrolled) conditions, generated by perturbations with random spectral content and moderate amplitudes of the order of 1% of the free-stream velocity. Transition to turbulence in boundary layers is triggered by infinitesimal perturbations, that begin to be amplified by the flow from the critical Reynolds number up to the transition point, which indicates the turbulence onset. In the transition region, the flow acts as a band-pass filter, amplifying through linear and nonlinear mechanisms unstable bands of modes. Temporal and three-dimensional complex variations on the flow are observed, as was firstly evidenced in the pioneer experiment [63]. In real conditions, disturbances can not be completely removed, and are always present affecting the flow in the form of thermal, mechanical and acoustic perturbations, surface irregularities, free stream turbulence among others. Natural transition is very sensitive to flow characteristics and disturbance parameters, such as, amplitude, spectrum and source of perturbation, [78]. It is a very intermittent phenomenon, difficult to measure and reproduce.

Due to complexity of the problem, investigations on natural transition considers several simplified approaches, for example, two-dimensional waves interacting with a low amplitude band of three-dimensional modes [81, 23, 8], transition induced by free-stream turbulence [10, 65], white noise [95, 77] and wave packet, which is the focus of this work.

Use of wave packet as a model for natural transition is justified by its broadband spectrum and experimental observations, where wave packets can be identified in the time-velocity signals induced by free stream turbulence [73, 30] and by artificially excited white noise [77]. Through Fourier analysis, separated modes in the wave packet can be monitored to identify linear and nonlinear interactions, and relate results with observations in natural transition.

1.1 Relevance

In many practical situations control of the transition point is crucial, as well as the determination of flow properties in the transition regime. In some cases, it is needed to promote turbulence as in chemical mixing, combustion or to avoid separation. Delay of turbulence onset is important for extension of laminar flow, because it is related with lower skin-drag and higher lift coefficients. Investigations on a Airbus A320, [47], evidence that skin friction drag is responsible for about 50% of total drag, from this percentage 25% is generated on the wings. Depending on the specific part of the airplane, is possible to achieve different levels of drag reduction. An extreme case is the drag of the fin, that can be reduced in 38% resulting in a saving of 1.3% in fuel consumption. In subsonic aircraft, fuel represents around 27% of DOC (Direct Operational Cost), in supersonic aircraft represents 35%.

Extension of laminar region can be done with control systems or by wing shape optimizations. Cost and

technical requirements of control systems, suggest that drag reduction based on laminar wings would give more benefits, however their design is a challenge, because limitations in understanding the transition process difficult refined optimizations. Accurate drag estimations depend on practical and accurate methods, to reduce time in design cycles. The dimensionless drag count coefficient is a measure of drag. At cruise, drag count varies between 200 to 400. For subsonic cruise 1 drag count is equivalent to 100kg, for supersonic cruise 1 drag count is equivalent to 5% of the payload. The accuracy desired for drag calculation is 10 drag counts for subsonic, 4 for transonic cruise and 1 for supersonic cruise, [83]. Methods used in aircraft industry can have errors on estimations on drag on the order of 10%. Transonic cruise presents even higher deviations [83]. The formulation of accurate and practical methods is based on a detailed understanding of the transition process, that remains as an open problem.

Usually engineering problems are solved by means of empirical correlations or semi-empirical methods [18], as for example e^N method [88], that is one of the most employed . This solutions produces acceptable results on engineering applications but does not explains the transition phenomenon.

1.2 Transition routes

Depending mostly on perturbation amplitude there are two main routes of transition to turbulence, bypass transition and modal amplification [24]. Bypass transition occurs at high perturbation amplitudes and the flow changes abruptly from laminar to turbulent, this route will not be considered in this work. In modal route, the flow pass through several stages, changing flow properties and developing complex vortical structures gradually in controlled experiments, as sketched in figure 1.1.

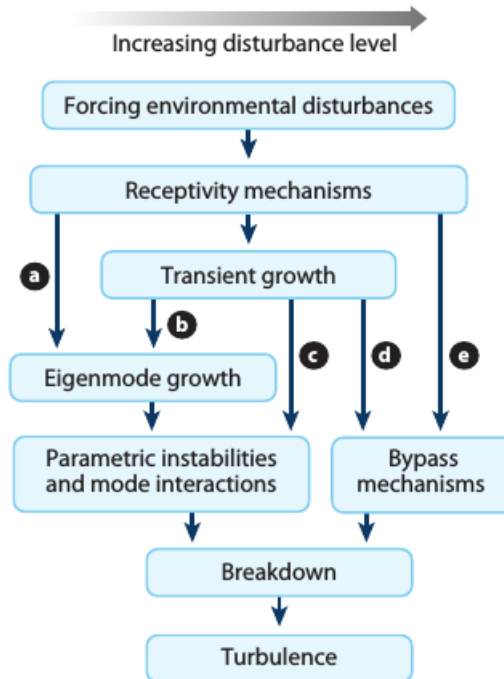


Figure 1.1: Paths to turbulence in boundary layers. (Reproduced from [24]).

The simplest case of hydrodynamic instability on a boundary layer is considering a monochromatic perturbation with infinitesimal amplitude, in relation to the free-stream velocity. This stage is also known as primary instability and is described by the Linear Stability Theory (LST). It occupies around 80% of the transition region, generating 2D structures for Mach numbers < 0.7 or 3D structures for higher Mach numbers. This theory is derived from the linearization of Navier Stokes equations, and arrives on the Orr-Sommerfeld equation [15, 70], this equation is in terms of disturbance u' , which results from subtract the perturbed flow \bar{u} from the base flow:

$$u' = \bar{u} - u_{base} \quad (1.1)$$

The ansatz for the solution of the Orr-Sommerfeld equation is a harmonic wave described by:

$$u' = \exp(-i\omega t + \alpha_x x + \beta z) \quad (1.2)$$

In the spatial approach, $\alpha = \alpha_x + i\alpha_i$, the frequency ω and spanwise wave number $\beta = \frac{2\pi}{\lambda_z}$ are real and considered as parameters, then, α comes from the flow response. Theoretical results of linear instability for boundary layer can be summarized in the instability diagram (figure 1.2). The flow acts as a band-pass filter, amplifying the unstable band of frequencies, defined by the inner region of the diagram. This amplification generates the so called Tollmien-Schlichting waves (TS-wave), which amplitude increases in downstream up to the end of the unstable region, as sketched in figure 1.2. The points where disturbance start to grow and to decay are know as first and second branch respectively This waves were predicted theoretically at the beginning of 1930 decade [85, 68] and confirmed experimentally in the classic experiment of [73] in the first low turbulence wind tunnel. Previous attempts to detect TS-waves failed due to relative high noise level in the wind tunnels. Results only were published after the Second World War. Tollmien-Schlichting waves have a bi-dimensional wave front, are characterized by the growth rate α_i , streamwise wave number α_x . Oblique waves with spanwise number β have a same behavior and propagates with an angle ψ with phase velocity c_p .

From DNS variables, this parameters can be calculated as:

$$\psi = \text{atan} \frac{\beta}{\alpha_x}, \quad \alpha_x = \frac{d\theta(x)}{dx}, \quad \alpha_i = -\frac{d[\ln(A(x))]}{dx}, \quad c_p = \frac{\omega}{\alpha_x} \quad (1.3)$$

For an oblique wave with spanwise wave number β , the phase speed is given by [36]:

$$c_p = \frac{\omega \alpha_x}{\alpha_x^2 + \beta^2} \quad (1.4)$$

A mode can be identified by the parameters (ω, β) or in terms of the harmonics (n, k) of a given fundamental mode (ω_0, β_0) .

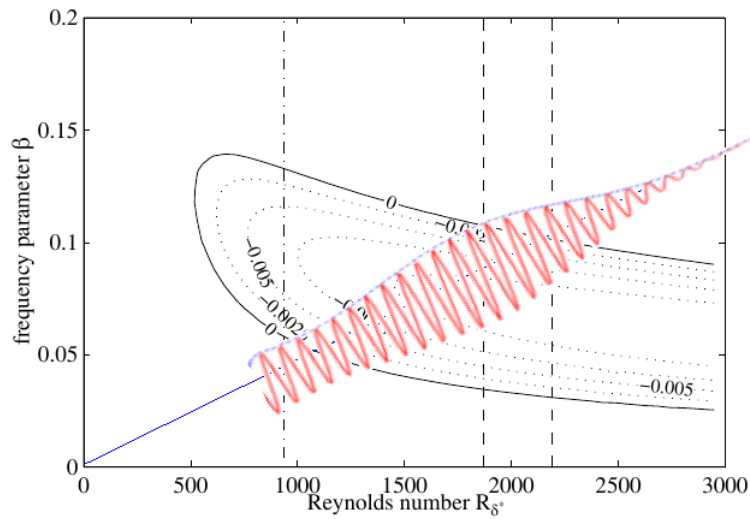


Figure 1.2: Tollmien-Schlichting wave in the diagram instability. Reynolds number is based on boundary layer displacement $\delta^*(x)$ and non-dimensional frequency.

At higher disturbance amplitudes, around 0.06% – 0.1% of the free stream velocity, moderate nonlinear effects rise, strong amplification in a short spatial region by growth rates increase substantially with respect to linear growth rates. Three-dimensional vortical structures are generated, with a defined spatial and temporal periodicity. Also skin drag coefficient increases and velocity profiles suffers deformation.

Under controlled disturbances, three nonlinear mechanisms have been discovered, fundamental or K-type [39, 33], subharmonic or H-type [35, 36], both identified in experimental observations and oblique resonance (O-type) discovered numerically, initially for compressible boundary layer at Mach 1.6 by [7] and for incompressible boundary layer by [71]. They were reported in 1962, 1977 and 1992 respectively.

Another kind of nonlinear amplification is proposed by [94, 93], which establishes that nonlinear resonance occurs when waves have same phase velocity. This kinds of nonlinear amplification are known as secondary instability. These mechanisms separately can lead to a complete breakdown to turbulence [67, 79]. An isolated bi-dimensional TS-wave can not promote transition, at least low amplitude oblique waves are needed. It is not clear if this mechanisms are present in natural transition, how they coexist and interact or if there are unknown nonlinear mechanisms. This mechanisms are important because in more complex cases, as wave packets and natural transition, they have been identified. For disturbance amplitude larger than %5 of the free-stream velocity, strong nonlinear effects are dominant and turbulent spots are generated, interact to achieve fully turbulent regime.

Subharmonic breakdown is triggered by a threshold amplitude of the mode $(1, 0)$, which resonates with the mode $(1/2, \pm 1)$. In this mechanism, vortical structures with staggered pattern are generated. Velocity amplitude varies in the range 0.2% to 0.6%, and depending on its specific value, spatial vortex periodicity changes.

Fundamental resonance is initiated by the interaction of a primary wave $(1, 0)$ and a pair of oblique waves $(1, \pm 1)$ at a low amplitude. The primary mode has a catalytic role, because energy transferred to the oblique waves comes from the flow, not from the 2D mode, which keeps its energy almost without variation. In this mechanism are generated vortical structures aligned, it develops in a short region and generates peaks in velocity signal, during the process harmonics also are generated and amplified. It is

more explosive than subharmonic resonance. During resonance process, both modes reach the same phase velocity, this is known as phase locking. For this kind of resonance there are only a few results in literature for incompressible boundary layer.

In the subharmonic resonance, threshold amplitude and phase locking have analog behavior than in fundamental resonance.

Oblique transition is generated by the nonlinear interaction of the pair of oblique waves $(1, \pm 1)$. In this resonance, there is not threshold amplitude. Modes grows linearly and when reach high amplitudes they transfer energy to a steady mode $(0, \pm 2)$, also harmonics $(0, 2k)$ are generated. Linear and nonlinear behavior are difficult to separate. Several works, [51, 50] shows that oblique breakdown is a viable path to turbulence on supersonic boundary layers.

Compressibility can change stability properties of a given flow. Research of transition in compressible boundary layer is delayed of its incompressible counterpart, due mainly to experimental difficulties and the problem complexity by the increase of variables and parameters. There are only a few experiments of controlled transition on supersonic boundary layers, experiment of [74] for Mach 2 is commonly used as main reference for low supersonic Mach numbers. Investigations on nonlinear transition in compressible boundary layers starts at the ends of the 1980s, with studies on secondary instability. This coincides with a noticeable improvement in the calculation capacity and the cost reduction of the computational resources. Since then, the amount of numerical investigations is increasing. Also in these years, numerical approaches are formulated, capable of reproducing moderate nonlinear behavior of the Navier-Stokes equations, like the PSE theory, (Parabolized Stability Equations) [6]. This methods were applied to compressible boundary layers to investigate the initial stages of nonlinear regime of transition [12]. In subsequent years, several systematic studies were performed on secondary instability at subsonic [19, 49], and supersonic boundary layers [57]. Also, [84] calculated secondary instability for compressible boundary layer at several Mach numbers. In recent theoretical works, spatial modes are investigated [86], the effect of heat transfer on Klebanoff modes [64], and more recently, a new mode was discovered for compressible boundary layer [87]. Compressibility alters stability properties of a given flow. According to LST [45, 27, 46, 60], at subsonic Mach numbers the unstable region is similar to the incompressible case. The main differences are in a reduction of the growth rates and of the critical Reynolds numbers [60]. In contrast to incompressible boundary layers, for $Mach \geq 0.7$ the 3D disturbances with angle of propagation $45^\circ < \psi < 60^\circ$ are more unstable than 2D waves [92], the effect is strongest in the range $2 < Mach < 3$.

At subsonic Mach numbers compressibility has the overall effect of stabilizing and as a direct consequence, the transition region is longer [48]. However, the set of most unstable modes can change, depending on the specific value of the Mach number, due to several effects, some of them, described below.

Results on secondary instability mechanisms [19], shows that for subsonic Mach number subharmonic resonance is importantly reduced with increasing Mach number and decreasing Reynolds number i.e. it is need a longer region to develop than the incompressible counterpart. Fundamental resonance is stronger than subharmonic, and more intense with angle [84].

At fixed Reynolds number and depending on the amplitude of the fundamental wave and the spanwise wave number, compressibility may appear stabilizes or destabilizes [19], however this is a particular case of the value of Mach number. In subharmonic resonance there is a preferred band in spanwise wave numbers [57]. In subsonic boundary layers heat transfer has a stronger effect on linear instability than in supersonic ones [69, pag. 467]. By adding heat into the boundary layer, unstable region increases, heat removal has stabilizing effect [38].

Methods for transition prediction used in industry are mainly based on linear amplification and only limited nonlinear effects are included, for example, by coupling Navier-Stokes equations to the e^N method [97], or using nonlinear models of natural transition, [41]. Sometimes additional effects, such as the compressibility [37] are also taken into account.

1.3 Wave packets and natural transition

In research on natural transition, the wave packets have been used as a model, because their broadband spectral composition can represent the spectrum of an uncontrolled disturbance. Also wave packet format is observed in the time-velocity signal in experiments on natural transition, induced by free stream turbulence [73, 30] and by artificially excited white noise [77].

Early works on wave packets were experimental, establishing the main characteristics of packet evolution. [89] reveals selective nonlinear amplification in the streamwise direction. Next experiments focused on linear evolution [29] to compare results with a linear model [28]. Later, [14] perform measurements of the complete transition process, from linear amplification up to formation of turbulent spots. In [13] analysis for separated modes is applied, to identify nonlinear amplification. Subsequent experiments focuses in several aspects of moderate nonlinear regime, [54] investigates the origin of modes generated nonlinearly, the phase effect of the perturbation [53] and the effect of magnitude of the modulation [52]. Results of [3] shows that the pressure gradient has a large influence on evolution that packet format. In these works, bands of nonlinearly amplified modes suggest presence of secondary instability mechanisms, both, fundamental and subharmonic. Usually, in the experiments and simulations of wave packets, frequency spectrum of the perturbation is carefully controlled, less attention is given to the spanwise spectrum.

In the literature, the growth of these waves has been attributed to subharmonic instability of the C or H type. Nevertheless, the conclusion is generally based only on the fact that these waves fall close to the subharmonic band, and that the dominant spanwise wave number is close to that obtained for subharmonic resonance for controlled (unmodulated wave) transition [14, 54, 79]. It is clear in the literature that the dominant subharmonic mode in the packet does not have exactly half the frequency of the dominant primary fundamental mode in the packet. The frequency ratio is closer to 2/3 and is often associated with detuned subharmonic resonance [9], but such resonance would normally be associated with two modes symmetric with respect to the actual subharmonic frequency. This state of affairs led to suggestions that a difference mechanism could be at play [96], namely phase locking mechanism [94]. It is apparent that the issue is not yet settled. It would appear that comparison of actual growth rates would be a much more definite evidence for conclusion, but this was never shown in the literature, except in the experiments of [16], which performed such an analysis for waves modulated only in the streamwise direction. [16] produced the streamwise modulation by combining 2 or 3 waves of different frequency and the subharmonic waves were also artificially excited. With this strategy, the problem of identification of detuned resonance in the modulated wave system was circumvented because the degree of detuning was established by the excitation, not by the evolution. Although being an important step into modulated waves, the analysis carried out in [16] is still limited relative to the wave packet composed by a continuous spectrum.

1.3.1 DNS simulations of wave packets

Probably [20] is the first direct numerical simulation (DNS) for transitional boundary layers, focused on explore quality of numerical solutions by comparison with results of linear theory and related experimental observations. [22] quantifies the effect of assumptions used for derivation of LST, as non-parallelism. Due to computational limitations, [21] performed first simulations of two-dimensional wave packets. Early three-dimensional DNS simulations of transition in compressible boundary layers, performed along the decade

of 1990s, were focused on explore the potential of numerical approach. Also into developing accurate numerical methods for this kind of problem and improving computational performance, using parallelization [31].

In the literature, there are three main reference experiments of wave packets in incompressible boundary layer, [29], [14] and [52]. The first two experiments were reproduced using DNS simulations, by [40, 76] and [96] respectively, for numerical investigation. A numerical analysis of the experiment [52] is not found in literature.

Some observations at Mach 0.5, considering white noise [58], nonlinear growth [91], transition on an air-foil [44] and secondary instability mechanisms [17] suggest that up to Mach 0.5 there are no remarkable differences in initial nonlinear stages of transition on compressible boundary layer. Then for $\text{Mach} > 0.5$, compressibility effects rises on the transition process.

A remarkable fact of the DNS simulations is the prediction of the oblique transition mechanism, not observed previously in experiments. In the last fifteen years DNS simulations concentrated on initial nonlinear stages and fully developed turbulence [17]. More recently focus is on determination of details in the transition process at several Mach numbers, considering changes in the three dimensional structures and the effect of a selected parameter, such as wall temperature and geometry.

Initial works of wave packets on compressible boundary layers are for hypersonic flows [25], and DNS simulations at Mach 1.3 [61], Mach 2 [51], Mach 3 [50] and several for higher Mach numbers [26, 80].

Despite a great number of engineering applications be in high subsonic and transonic regime, lot of the investigations on wave packet evolution concentrate on either, incompressible and supersonic boundary layers. Research of wave packet evolution in subsonic boundary layer is very poor. A more general comprehensive review of DNS used as research tool in turbulence can be found in [56].

1.4 Objectives of this work

Natural transition develops through different routes, depending mainly, on specific characteristics of spectral content and amplitude of the perturbation. This routes may include secondary instability mechanisms, that could coexist interchanging dominance along transition stages depending on specific conditions. Probably unknown scenarios are also present, this could generate intermittency and formation of turbulent spots. Investigation of the aspects are the focus of actual research.

The present work has two principals objectives, to develop a DNS code focused in problems of transition in subsonic boundary layer on a flat plate and to investigate natural transition in subsonic regime, modeled by wave packets and a preliminary study considering white noise. Three main problems were considered, numerical simulation of the experiment [54] on incompressible boundary layer, the influence of compressibility on wave packet evolution at subsonic Mach numbers and finally, a preliminary study of transition induced by white noise in a boundary layer at Mach 0.2 and 0.9.

The numerical results are analyzed in the context of current nonlinear theories for monochromatic waves, to establish the nonlinear regime that the packet undergo.

1.5 Structure of the Report

Report is organized as follows. Chapter 2 describes the governing equations and boundary conditions tested and eventually used. The numerical procedure is also described, including the time and space discretization, filter, grid stretching and parallelization, among other aspects. In Chapter 3, the validation tests performed on the code are presented. This includes tests in the linear regime of TS-waves as well as nonlinear regimes. The nonlinear regimes include fundamental and subharmonic instabilities, and oblique transition. Results of incompressible and compressible subsonic boundary layers available in the literature were used for comparison.

In Chapter 4 results for DNS simulation of the experiment [54] are presented. Detailed comparison on physical and Fourier spaces is shown, a nonlinear modal analysis is performed and several relevant calculations are developed. Chapter 5 is devoted to results for wave packets at Mach 0.7 and 0.9, including interaction between packets at Mach 0.9. Chapter 6 presents results and preliminary analysis for transition generated by white noise at Mach 0.2 and 0.9. Finally, Chapter 7 is dedicated to conclusions, final remarks and suggested future work.

Chapter 2

Physical problem and computational setup

2.1 Governing equations

Navier Stokes equations for compressible flow at subsonic Mach numbers are solved numerically in a rectangular integration domain considering the non-conservative formulation, in terms of density ρ , velocity components u_i and internal energy e . All variables are non-dimensionalized by the displacement thickness δ_0^* at a reference position in streamwise direction, free-stream value of velocity U_∞^* and density ρ_∞^* .

$$\frac{\partial \rho}{\partial t} = -\rho \frac{\partial u_i}{\partial x_i} - \frac{\partial \rho}{\partial x_i} u_i, \quad (2.1)$$

$$\frac{\partial u_j}{\partial t} = \frac{\partial u_j}{\partial x_i} u_i - \frac{1}{\rho} \frac{\partial p}{\partial x_j} + \frac{1}{\rho} \frac{\partial \tau_{ij}}{\partial x_i}, \quad (2.2)$$

$$\frac{\partial e}{\partial t} = -\frac{\partial e}{\partial x_i} u_i - \frac{p}{\rho} \frac{\partial u_i}{\partial x_i} + \frac{1}{\rho} \tau_{ij} \frac{\partial u_j}{\partial x_i} - \frac{1}{\rho} \frac{\partial q_i}{\partial x_i} = 0. \quad (2.3)$$

The viscosity tensor is defined as

$$\tau_{ij} = \frac{\mu(T)}{Re} \left[\frac{\partial u_i}{\partial x_j} + \frac{\partial u_j}{\partial x_i} - \frac{2}{3} \delta_{ij} \frac{\partial u_k}{\partial x_k} \right] \quad (2.4)$$

the heat flux term is given as

$$q_i = -\frac{\mu}{(\gamma - 1) Re Pr M_\infty^2} \frac{\partial T}{\partial x_i}. \quad (2.5)$$

The Reynolds, Prandtl and Mach numbers are defined as:

$$Re = \frac{\rho_\infty^* U_\infty^* \delta_0^*}{\mu_\infty^*} \quad Pr = \frac{\mu_\infty^* c_p^*}{k^*} \quad M_\infty = \frac{U_\infty^*}{c_\infty^*} = \frac{U_\infty^*}{\sqrt{\gamma p_\infty^* / \rho_\infty^*}} \quad (2.6)$$

with μ_∞^* , c_p^* and γ the reference dynamic viscosity, the specific heat and the ideal gas constant. Temperature and internal energy are related by:

$$e = \frac{T}{(\gamma^2 - \gamma) M_\infty^2} \quad (2.7)$$

To complete the set of equations required to solve the Navier-Stokes equations system, the ideal gas hypothesis is considered, to relate the pressure p with the internal energy and density

$$p = (\gamma - 1)\rho e \quad (2.8)$$

Finally viscosity is modeled considering the Sutherland's law

$$\frac{\mu^*}{\mu_\infty} = \mu(T) = \frac{1 + C}{T + C} T^{\frac{3}{2}} \quad (2.9)$$

with $C = \frac{110k}{T_\infty^*}$, and $T_\infty^* = 300K$. The relation between dimensional variables denoted with (*) and nondimensional ones is:

$$\begin{aligned} \rho &= \frac{\rho^*}{\rho_\infty^*}, & p &= \frac{p^*}{p_\infty^* U_\infty^{*2}}, & x_i &= \frac{x_i^*}{\delta_0^*}, \\ T &= \frac{T^*}{T_\infty^*}, & u_i &= \frac{u_i^*}{U_\infty^*}, & t &= \frac{t^* U_\infty^*}{\delta_0^*}, & e &= \frac{e^*}{U_\infty^{*2}}. \end{aligned}$$

2.2 Numerical Methods

A DNS code was developed focused on problems of transition in boundary layer at subsonic Mach numbers. The code is implemented in *Fortran90* and parallelized using MPI (Message Passage Interface). Routines of LAPACK library are used to solve linear equation systems.

2.2.1 Discretization

For spatial discretization a compact finite differences scheme was constructed with spectral like resolution, based on [43]. Scheme is 4th order accuracy and is composed by a tridiagonal stencil to reduce computational cost. These schemes allow high order discretizations with a lower number of grid points than required in explicit methods. It also allows maintain a desired accuracy over a range of length scales. The time integration is performed with a standard 4th order Runge Kutta method:

$$y_{n+1} = y_n + \frac{1}{6}(k_1 + k_2 + k_3 + k_4) \quad (2.10)$$

with:

$$k_1 = \Delta t f(t_n, y_n) \quad (2.11)$$

$$k_2 = \Delta t f(t_n + \frac{1}{2}\Delta, y_n + \frac{1}{2}k_1) \quad (2.12)$$

$$k_3 = \Delta t f(t_n + \frac{1}{2}\Delta, y_n + \frac{1}{2}k_2) \quad (2.13)$$

$$k_4 = \Delta t f(t_n + \Delta, y_n + k_3) \quad (2.14)$$

Uniform grid is used in streamwise and spanwise directions, grid is stretched in wall normal direction to increase resolution near the wall and resolve gradients correctly. Details can be found in [5, 4].

2.2.2 Compact finite differences

For transition to turbulence problems it is needed to calculate variations of the flow in a wide range of scales, usually in a range of 6 orders of magnitude, then, spectral-like schemes are interesting. In a uniform grid a first derivative can be approximated as (2.15)

$$\beta f'_{i-2} + \alpha f'_{i-1} + f'_i + \alpha f'_{i+1} + \beta f'_{i+2} = c \frac{f_{i+3} - f_{i-3}}{6h} + b \frac{f_{i+2} - f_{i-2}}{4h} + a \frac{f_{i+1} - f_{i-1}}{2h}. \quad (2.15)$$

The coefficients a , b , c , α , e β are chosen to set the order of stencil with respect to the truncated Taylor series.

$$\text{Second order: } a + b + c = 1 + 2\alpha + 2\beta, \quad (2.16)$$

$$\text{Fourth order: } a + 2^2b + 3^2c = 2 \frac{3!}{2!} (\alpha 2^2 \beta), \quad (2.17)$$

$$\text{Sixth order: } a + 2^4b + 3^4c = 2 \frac{5!}{4!} (\alpha 2^4 \beta), \quad (2.18)$$

$$\text{Eigth order: } a + 2^6b + 3^6c = 2 \frac{7!}{6!} (\alpha + 2^6 \beta), \quad (2.19)$$

$$\text{Tenth order: } a + 2^8b + 3^8c = 2 \frac{9!}{8!} (\alpha + 2^8 \beta). \quad (2.20)$$

Relations (2.16) to (2.20) can be used to construct up to 10^{th} order stencils. By means of error analysis it is possible to calculate the modified wave number w' as a function of real wave number w for each finite difference scheme (2.21)

$$w'(w) = \frac{a \sin(w) + (b/2) \sin(2w) + (c/3) \sin(3w)}{1 + 2\alpha \cos(w) + 2\beta \cos(2w)}. \quad (2.21)$$

In [43] a 4^{th} order pentadiagonal schemes with spectral-like resolution are constructed, using relations (2.16) and (2.17) and imposing the condition:

$$w'(w_1) = w_1, \quad w'(w_2) = w_2, \quad w'(w_3) = w_3. \quad (2.22)$$

To reduce computational cost associated with a pentadiagonal systems to tridiagonal one, on the right hand side of the equation 2.15, two approximations were considered, namely, tridiagonal schemes with stencil of 5 and 7 points ($\beta = 0$). Both 4^{th} order and then relations (2.16) e (2.17) are used. The 5 point stencil imposing

$$c = 0, \quad w'(w_1) = w_1. \quad (2.23)$$

7 point stencil is:

$$w'(w_1) = w_1, \quad w'(w_2) = w_2. \quad (2.24)$$

The modified wave number and phase speed $c_p = w'/w$ for schemes derived here in comparison with usual schemes are shown in figures (2.1) and (2.2) respectively.

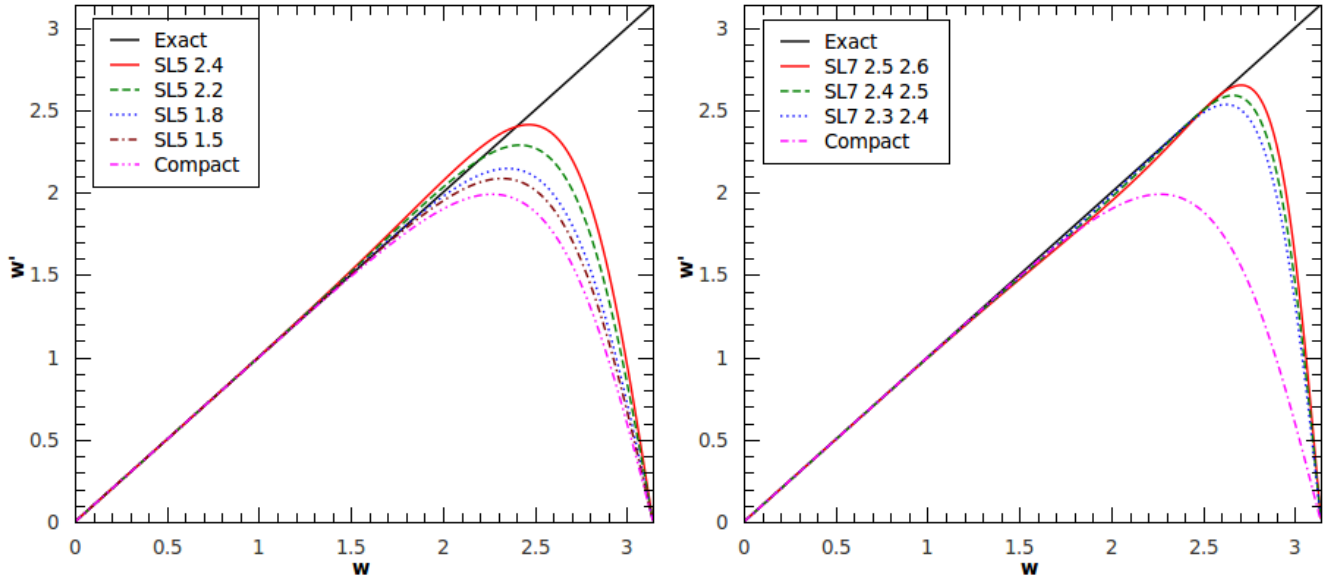


Figure 2.1: Modified wave number for several schemes. (a) 5 points stencil for $w_1 = 1.5$; $w_1 = 1.8$; $w_1 = 2.2$ and $w_1 = 2.4$. (b) 7 points stencil to $w_1 = 2.3$, $w_2 = 2.4$; $w_1 = 2.4$, $w_2 = 2.5$; $w_1 = 2.5$, $w_2 = 2.6$. Comparison with tridiagonal sixth order scheme. (Reproduced from [5]).

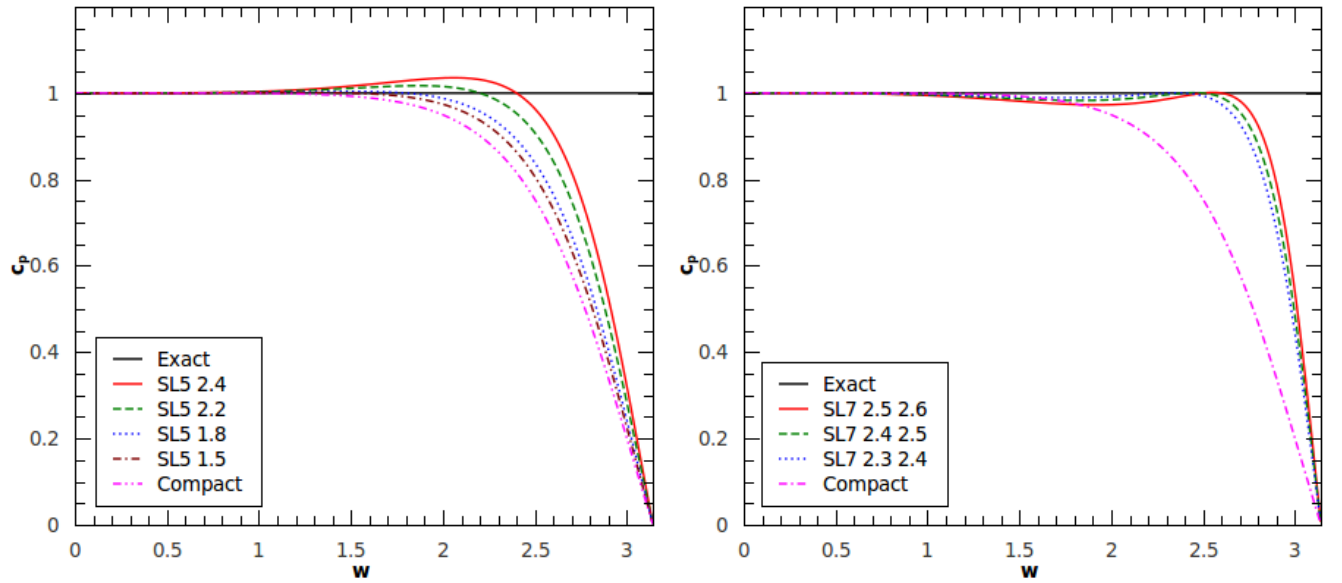


Figure 2.2: Phase velocity for several schemes. (a) 5 points stencil for $w_1 = 1.5$; $w_1 = 1.8$; $w_1 = 2.2$ and $w_1 = 2.4$. (b) 7 points stencil to $w_1 = 2.3$, $w_2 = 2.4$; $w_1 = 2.4$, $w_2 = 2.5$; $w_1 = 2.5$, $w_2 = 2.6$. Comparison with tridiagonal sixth order scheme. (Reproduced from [5]).

From the modified wave number curves and phase velocity for 5-point stencil, it was chosen $\omega' = 1.8$, because have the best approximation. By substitution into restrictions (2.16, 2.17, 2.21), the resulting stencil is:

$$\alpha = 0.364957272268410, \quad \beta = 0; \quad a = 1.57663818151227, \quad b = 0.153276363024547 \quad c = 0 \quad (2.25)$$

This stencil was employed in all simulations performed in the present work.

2.2.3 Numerical Stability

For the convective Navier-Stokes equations this integration scheme is stable up to CFL (Courant-Friedrichs-Lewy) number around 1.3. The convection and diffusion stability condition are defined as:

$$\Delta t \leq \frac{CFL}{\left[\frac{\frac{1}{M_\infty} + u_{max}}{\Delta x} + \frac{\frac{1}{M_\infty} + v_{max}}{\Delta y} + \frac{\frac{1}{M_\infty} + w_{max}}{\Delta z} \right]} \quad (2.26)$$

$$: \quad \Delta t \leq \frac{1}{\frac{6}{Re} \left[\frac{1}{\Delta x^2} + \frac{1}{\Delta y^2} + \frac{1}{\Delta z^2} \right]} \quad (2.27)$$

2.2.4 Filter

Spurious oscillations are generated by flow transients, numerical boundary conditions, grid stretching among others factors, this nonphysical oscillations may be amplified affecting numerical solution. To control spurious oscillations a 10^{th} order low pass filter [90] is applied in each time iteration at the inner points of the domain. In the spanwise direction, a periodic filter is used to be compatible with the periodic boundary condition. The filtering level is controlled with the parameter $-0.5 \leq \alpha_f \leq 0.5$, low values of α_f correspond to higher filtering. In all simulations presented here $\alpha_f = 0.49$ was considered in all directions, which means almost no filter. The linear filter is defined by:

$$\alpha_f \bar{\phi}_{i-1} + \bar{\phi}_i \alpha_f \bar{\phi}_{i+1} = \sum_{n=0}^N \frac{a_n}{2} \phi_{i+n} + \phi_{i-n} \quad (2.28)$$

Coefficients for a tenth order filter are:

$$\begin{aligned} a_0 &= \frac{193 + 126\alpha_f}{256} & a_1 &= \frac{105 + 302\alpha_f}{256} & a_2 &= 15 \frac{-1 + 2\alpha_f}{64} \\ a_3 &= \frac{45 - 2\alpha_f}{512} & a_4 &= 5 \frac{-1 + 2\alpha_f}{256} & a_5 &= \frac{1 - 2\alpha_f}{512} \end{aligned} \quad (2.29)$$

2.2.5 Grid stretching

For the simulations performed in this work, two grids in y-direction were considered. First with $y_{max} = 20$, $ny = 51$ and a more refined grid, $y_{max} = 60$, $ny = 151$, both, shown figure 2.3.

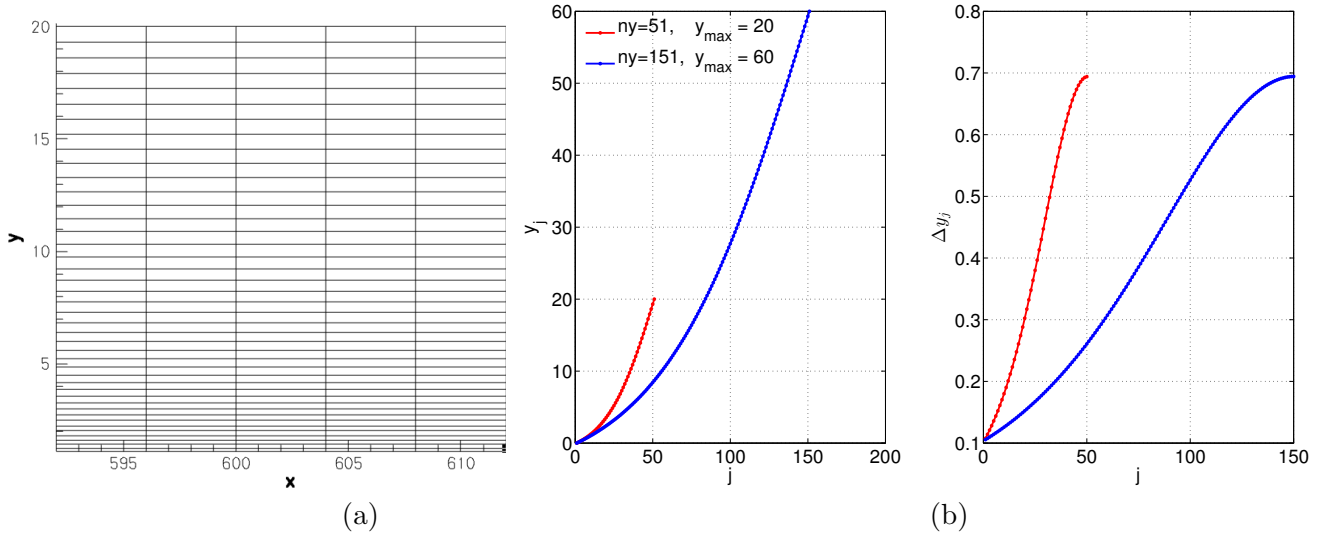


Figure 2.3: (a) Grid stretching in computational domain and (b) grid definition.

2.2.6 Boundary Conditions

Initially characteristic boundary conditions were considered to be used in the boundary layer simulations. As a code test, two types of characteristic boundary conditions [62] were applied to the Poiseuille flow, imposing reflecting and non-reflecting outflow boundary conditions. Results shown in figures 2.4, 2.5 reveals a good agreement, including details in the contour levels at the outflow. This approach calculates the numerical boundary conditions based on considerations and approximations of Navier-Stokes equations. This kind of boundary conditions was not used in the boundary layer, because have parameters strongly dependent of the problem that could influence simulations of transition to turbulence.

Reflecting Outflow

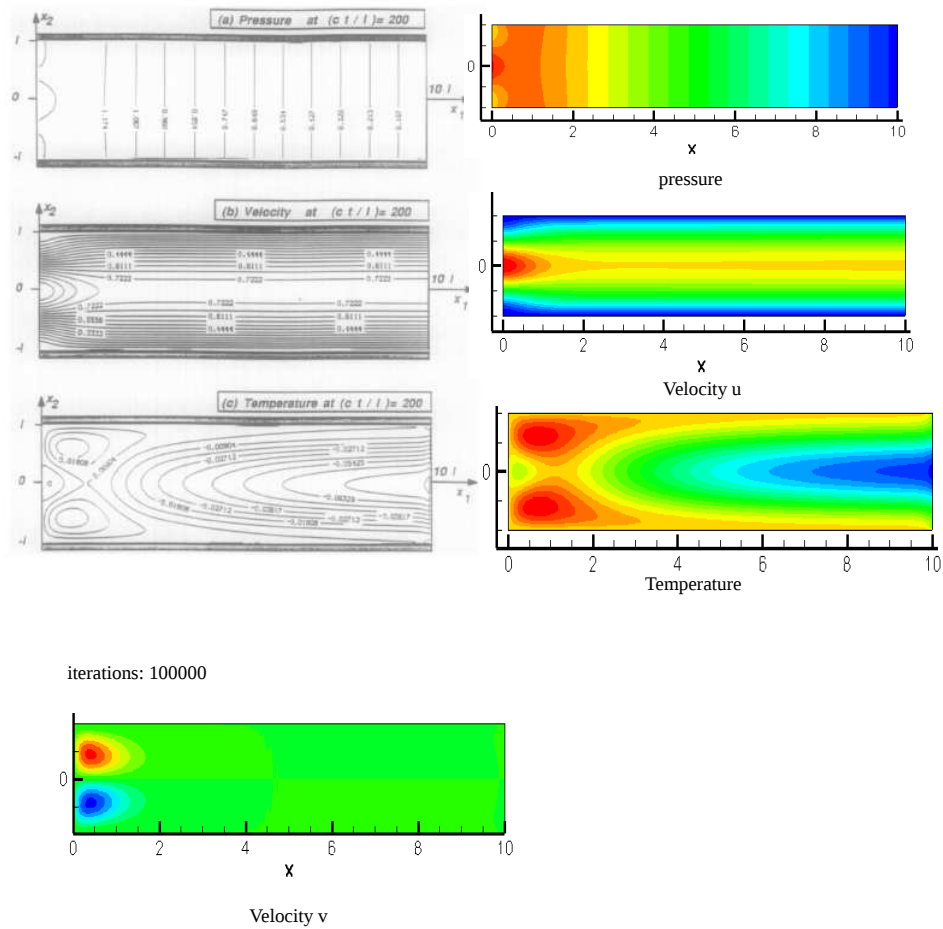


Figure 2.4: Comparison with DNS simulation of characteristic boundary conditions, using reflecting outflow, applied to Poiseuille flow. Reference figures (not colored), are reproduced from [62].

Non-Reflecting Outflow

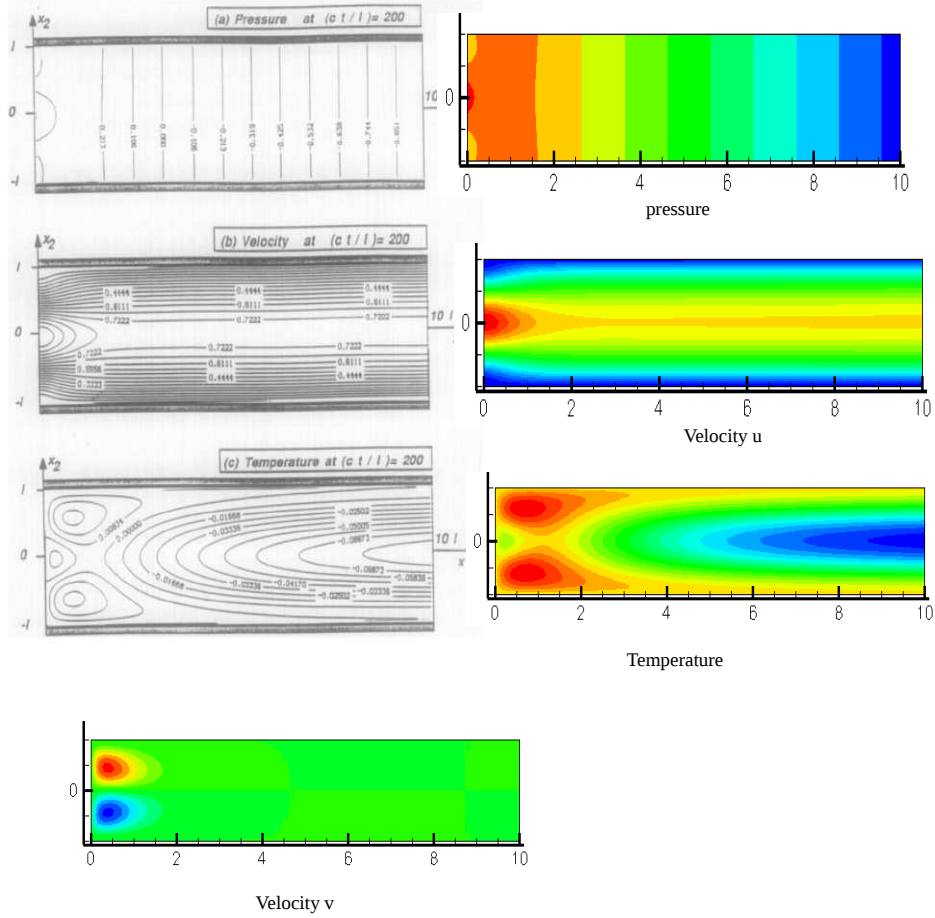


Figure 2.5: Comparison with DNS simulation of characteristic boundary conditions, using non-reflecting outflow, applied to Poiseuille flow. Reference figures (not colored), are reproduced from [62].

The base flow is obtained with a two-dimensional DNS simulation of the entire flat plate. At the inflow, uniform flow condition is imposed. At the outflow pressure is fixed, and the other flow variables are extrapolated using null second derivative. Also a buffer zone is included to avoid reflections into the integration domain. On the wall, a no-slip condition is applied to the velocity components, isothermal wall is used for the temperature, density is calculated with a compatibility condition for the pressure. Finally at the upper boundary, Neumann condition is applied to the velocity components and the pressure is fixed. In three dimensional simulations, periodic boundary condition is used in the spanwise direction.

The simulation is run until variations of the integrated variables are of order 10^{-12} . To represent free flow condition at the leading edge of the plate, a domain extension upstream the plate is included with free-slip condition at the wall, as sketched in figure 2.6. With this set up, some undesired and nonphysical pressure gradient which results in small velocity profiles deformations are avoided.

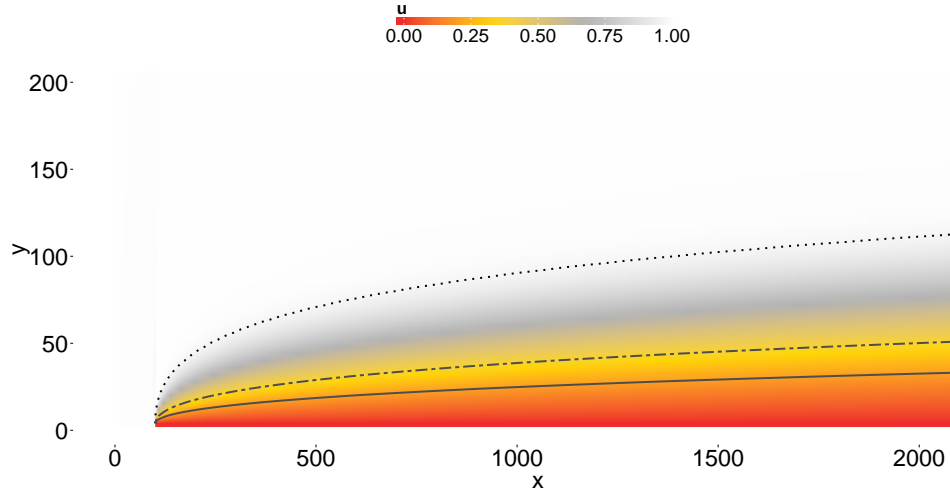


Figure 2.6: Boundary layer profiles generation. Upstream the leading edge of the plate a wall is included with free-slip condition to avoid nonphysical gradients. Figure is stretched in y direction to facilitate visualization $0.6\delta^*$ (-), $1.1\delta^*$ (-.-) and δ_{99} (...) .

2.2.7 Moving Frame 3D

To reduce computational domain and hence, the number of grid points a three dimensional moving frame was implemented. During simulation the domain is increased in downstream and spanwise, and reduced upstream, to perform calculation only in the region occupied by the wave packet. In figure 2.7 are shown three different physical domains superposed to evidence differences. Several tests performed show that there are no significant differences in the packet region or at the boundaries, in physical and Fourier spaces, between the simulation with and without moving frame.

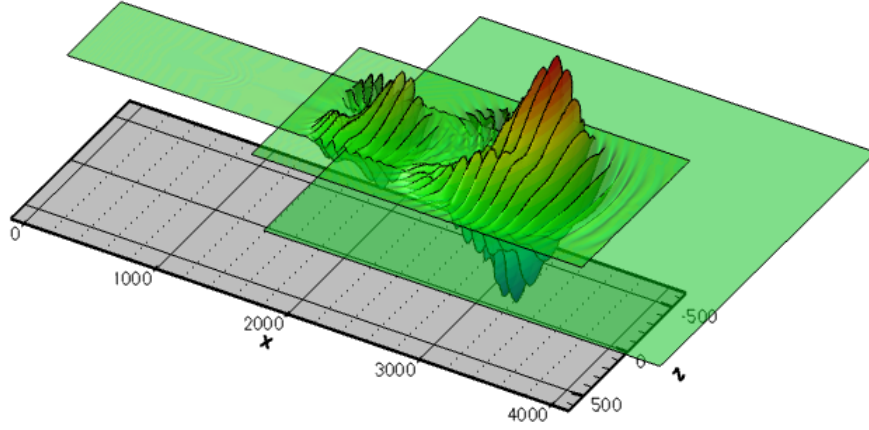


Figure 2.7: Moving frame 3D.

2.3 Parallelization

The code was parallelized employing domain decomposition by using library [1]. This implementation allows to divide the computational domain into $N \times 1$ or $N \times M$ blocks, sometimes named as slab and pencil decomposition respectively, as sketched in figure 2.8. In this kind of decomposition each processor stores a sub-domain, that contains all axis points in one direction, so that all derivatives in this direction can be calculated in parallel.

To calculate the derivatives in the other directions, orientation of the decomposition is changed. The orientation change is performed by transposition operations which involves communication between process, using *mpi_alltoall* routine, which is the principal source of overhead in this kind of parallelization. Depending on the computer architecture employed, an optimal decomposition exists, that minimizes the communication time. The parallelization used in this work do not introduce any additional error at the sub-domain boundaries, as occurs for other parallelization approaches [75], however the overhead in communication operations increase with the number of processors.

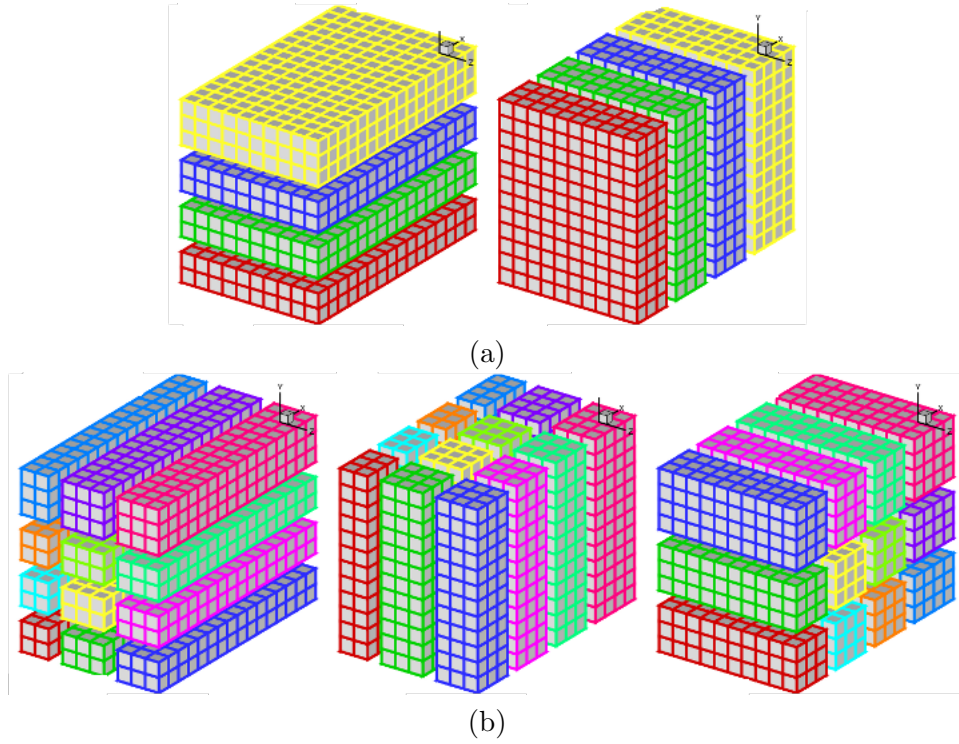


Figure 2.8: (a) Slab (b) pencil decomposition. (Reproduced from [1].)

2.3.1 Perform analysis

There are two kinds of tools to determine program performance, profiling and tracing. Profiling tools allow to collect global data from statistical sampling of events during execution of the program, *gprof* is an open-source tool of this kind. Tracing tools, as for example Vampir-trace, collect detailed data during execution. This kind of tools are more precise, but larger data files than in profiling tools are generated and can produce substantial computing overhead. To determine the computational performance of the current DNS simulations were used *gprof* for the sequential execution and Vampir-Trace for parallel execution.

Sequential execution

Using *gprof*, the code structure can be decomposed into blocks, as shown in figures 2.9, 2.10. Each box corresponds to a function of the code. Inside the boxes there are 3 numbers indicating percentage of total computational time employed by a particular function. Second number, between parentheses, indicates the amount of work done by the function and the third number is the number of calls of the function. Numbers outside the boxes are the percentage of work passed to the next function and number of calls. From this diagram can be concluded that 50% of the computational time is employed into spatial derivatives calculation and the most expensive function is *dgtsv* of [42] used to solve the tridiagonal system of the finite differences method, due to intensive calls. Time per/iteration per/grid point is of order of $5\mu s$.

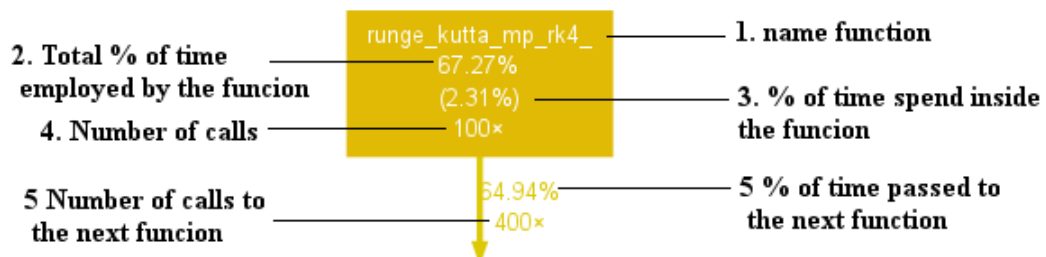


Figure 2.9: Execution diagram and computational cost obtained with gprof.

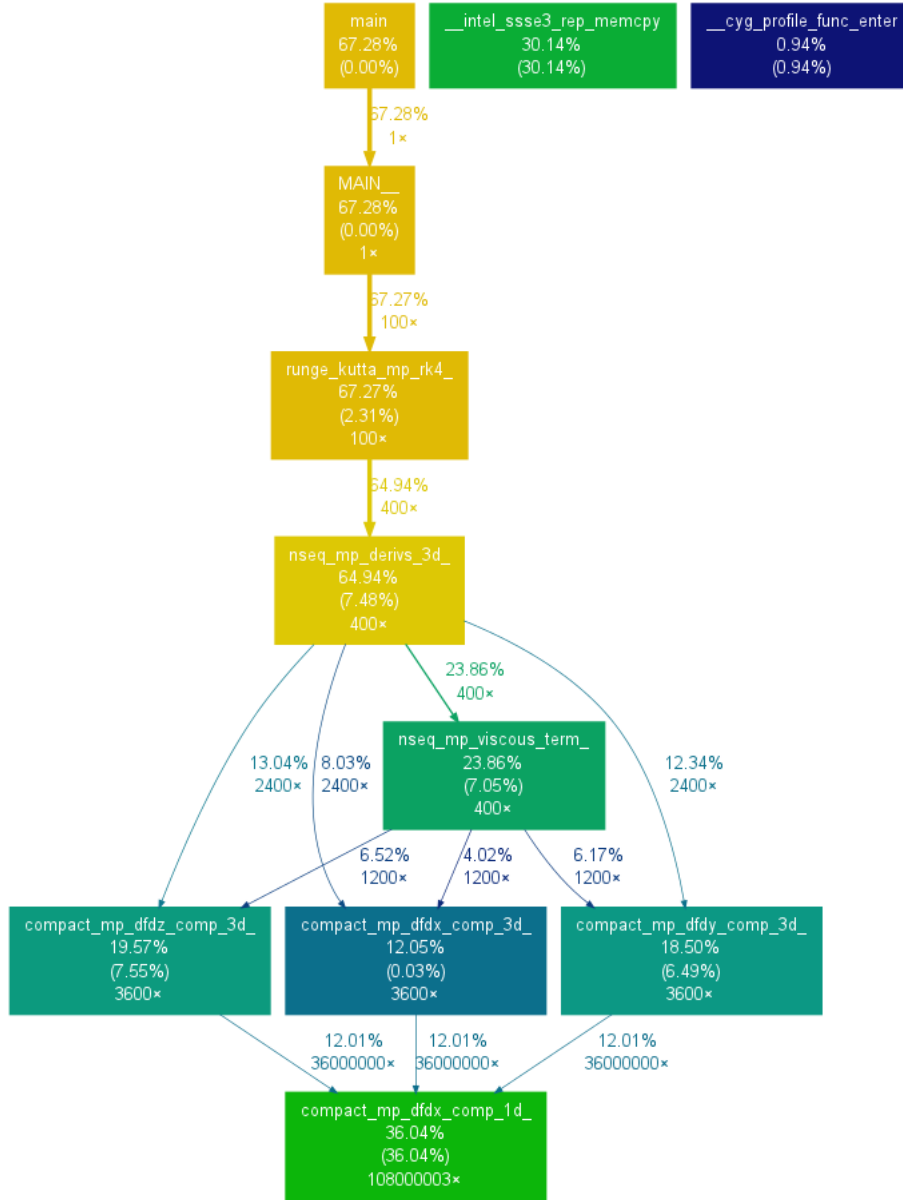


Figure 2.10: Execution diagram and computational cost obtained with *gprof*.

Parallel execution

By using *vampir* detailed diagrams (figure 2.12) of the communication between processors can be obtained, they allows to find errors, bottlenecks and plan optimizations. However this tasks require detailed work, only preliminary tests were performed for illustration. To evaluate performance of a parallelized program there are several metrics, for the DNS code, the most relevant metric is the speedup. Speedup measures efficiency of time reduction by increasing number of processors. Ideally, if n processors are used, the computational time is reduced by $\frac{1}{n}$. Use of parallelization requires communication between processors. In figure 2.11 a test up 130 processor was carried out for the DNS code, showing a reasonable performance. However, scalability has strong dependence of the computer architecture and physical communication

channel between processors. The study used in general less than 40 processors for which the performance is better.

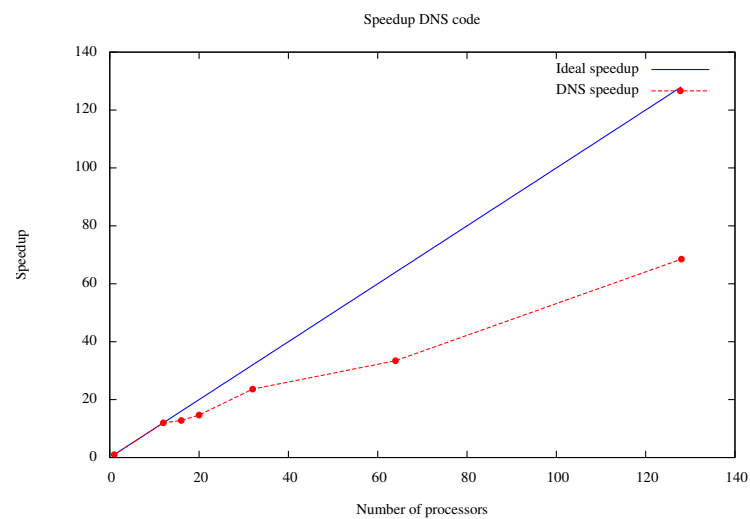


Figure 2.11: Speedup of DNS code.

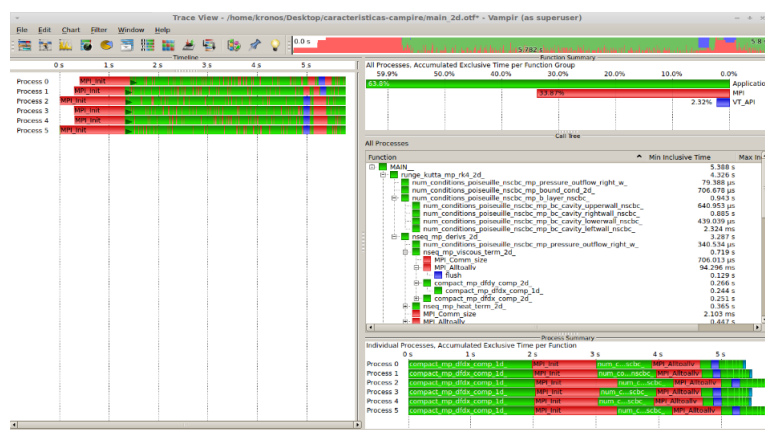


Figure 2.12: Diagrams of profiling obtained with *vampir*, showing details of communication routines.

Chapter 3

Code validation

The developed DNS code has been used successfully applied to study several hydrodynamic instability problems in cavity flow [5, 4] and boundary layer [48]. In this chapter, code validation tests are presented at several regimes of transition for subsonic boundary layer. Initially, comparisons of boundary layer profiles with theoretical results are shown. The next sections are devoted to comparisons between DNS simulations and results of the literature for primary and secondary instabilities.

3.1 Base flow generation

The base flow considered is a subsonic boundary layer over a flat plate, it is calculated with a two-dimensional DNS simulation starting from an uniform flow until stationary regime is reached with variations on integrated variables of the order go 10^{-12} .

3.1.1 Boundary layer profiles

To compare the boundary layer profiles generated with DNS simulations, the Stewartson equations, for compressible boundary layer (see [2]), were solved.. The differential equation system to be solved in terms of similarity variables F and T is:

$$\frac{d}{d\eta} \left(\frac{\chi}{Pr} \frac{dT}{d\eta} \right) + F \frac{dT}{d\eta} + (\gamma - 1) M^2 \chi \left(\frac{d^2 F}{d\eta^2} \right)^2 = 0 \quad (3.1)$$

$$\frac{d}{d\eta} \left(\chi \frac{d^2 F}{d\eta^2} \right) + F \frac{d^2 F}{d\eta^2} = 0 \quad (3.2)$$

with $\chi = \rho' \mu'$. The boundary conditions are:

$$T|_{\eta=0} = T_w, \quad \frac{dF}{d\eta}|_{\eta=0} = 0, \quad F|_{\eta=0} = 0 \quad (3.3)$$

For $\eta \rightarrow \infty$:

$$T = 1, \quad \frac{dF}{d\eta}|_{\eta \rightarrow \infty} \rightarrow 1 \quad (3.4)$$

Flow variables are recovered using the transformation:

$$\eta = \sqrt{\frac{Re}{2x}} \int_0^y \rho(x, \tilde{y}) d\tilde{y} \quad (3.5)$$

$$u = \frac{dF}{d\eta}, \quad v = T(\eta u - F) \sqrt{\frac{1}{2xRe}} \quad (3.6)$$

$$T = T(\eta), \quad \rho = 1/T, \quad e = \frac{1}{\gamma M^2(\gamma - 1)} + \frac{1}{2}(u^2 + v^2)\rho \quad (3.7)$$

To include Sutherland's law, χ is given by:

$$\chi = \frac{1+C}{T+C} \sqrt{T} \quad \frac{d\chi}{dT} = \chi \left\{ \frac{1}{2T} - \frac{1}{T+C} \right\} \quad (3.8)$$

Then, the system of equations 3.1 and 3.2 becomes:

$$\frac{d^3 F}{d\eta^3} = -\frac{1}{\chi} \frac{d^2 F}{d\eta^2} \left\{ \frac{d\chi}{dT} \frac{dT}{d\eta} + F \right\} \quad (3.9)$$

$$\frac{d^2 T}{d\eta^2} = -\frac{1}{\chi} \left\{ \frac{d\chi}{dT} \left\{ \frac{dT}{d\eta} \right\}^2 + Pr F \frac{dT}{d\eta} + Pr(\gamma - 1) M^2 \chi \frac{d^2 F}{d\eta^2} \right\} = 0 \quad (3.10)$$

The Blasius solution [92] is the theoretical result for incompressible boundary layer. In figure 3.1 are compared the velocity profiles in terms of the similarity variable $\eta = y \sqrt{\frac{Re}{2x}}$.

Also is shown the asymptotic value of the wall-normal velocity component, v , calculated with the three solutions.

The shape factor $H = \delta^*/\theta$, calculated with the Blasius and Stewartson solutions, and DNS simulation are respectively: $H_{Blasius} = 2.591566$, $H_{Stw} = 2.597096$, $H_{DNS} = 2.594004$. Flow parameters used in DNS simulations were Mach 0.2 and $Re=835$, $Pr = 0.71$.

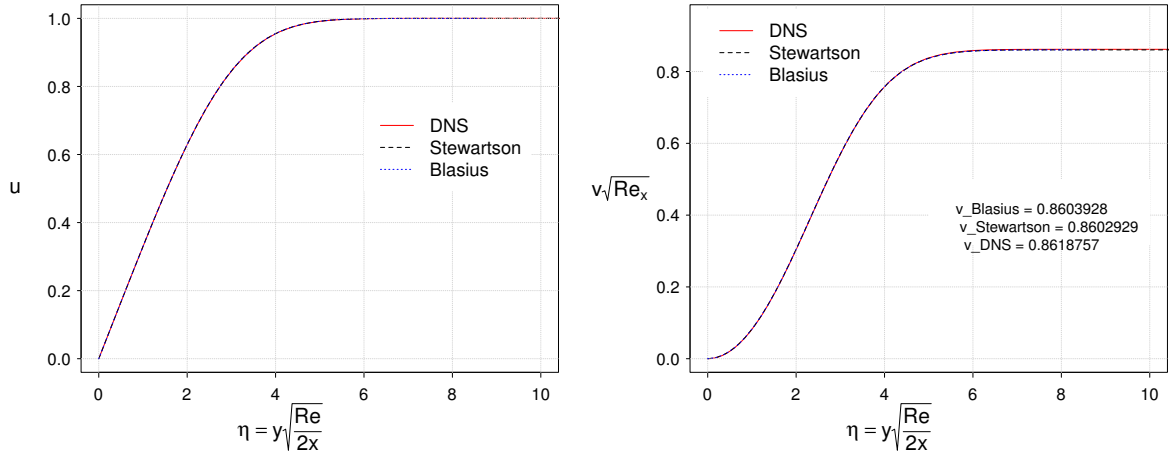


Figure 3.1: Comparison of Blasius profiles for velocity components, u , v , with Stewartson solution and DNS. Comparison of asymptotic values for v are in a very good agreement.

In Figure 3.2 is shown the thermal boundary layer for adiabatic wall condition, calculated with Stewartson solution and computed with DNS. The value of the adiabatic wall temperature T_{ad} , [92, pag. 511], also is compared by using the theoretical relation

$$T_{ad} = T_{\infty} \left(1 + r \frac{\gamma - 1}{2} M^2 \right) \quad (3.11)$$

with r the recovery coefficient, that for laminar boundary layer becomes $r \approx \sqrt{Pr}$.

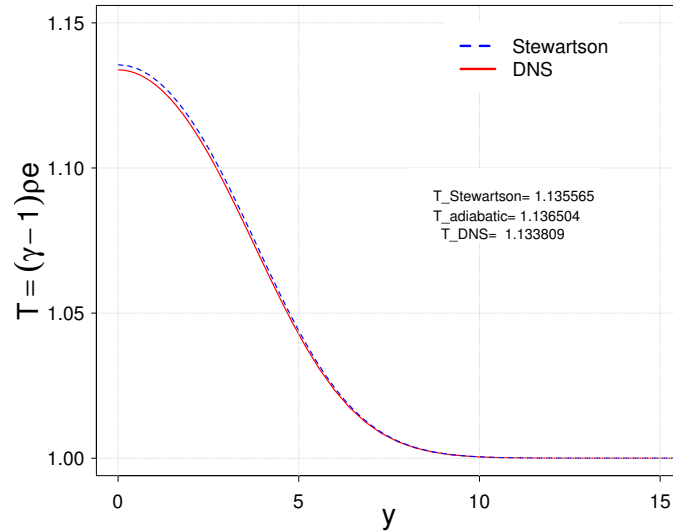


Figure 3.2: Temperature profile for adiabatic wall and comparison of values calculated from DNS, Stewartson solution and theoretical value at Mach 0.9.

All the comparisons performed are in a very good agreement with the theoretical results.

3.2 Hydrodynamic instability tests

[40] presents results of a DNS simulation for a TS-wave, to investigate the effect of unconsidered factors in LST, as non-parallelism. In figure 3.3 is shown a comparison of amplification curve, for a TS-wave with $F = 120$. The perturbation is introduced into the flow by using a localized periodic blowing and suction disturbance, applied at the wall normal component of velocity as :

$$v_{wall} = A_{1,0} \cos(\alpha_x(x - x_0)) \cos(\omega t) \quad (3.12)$$

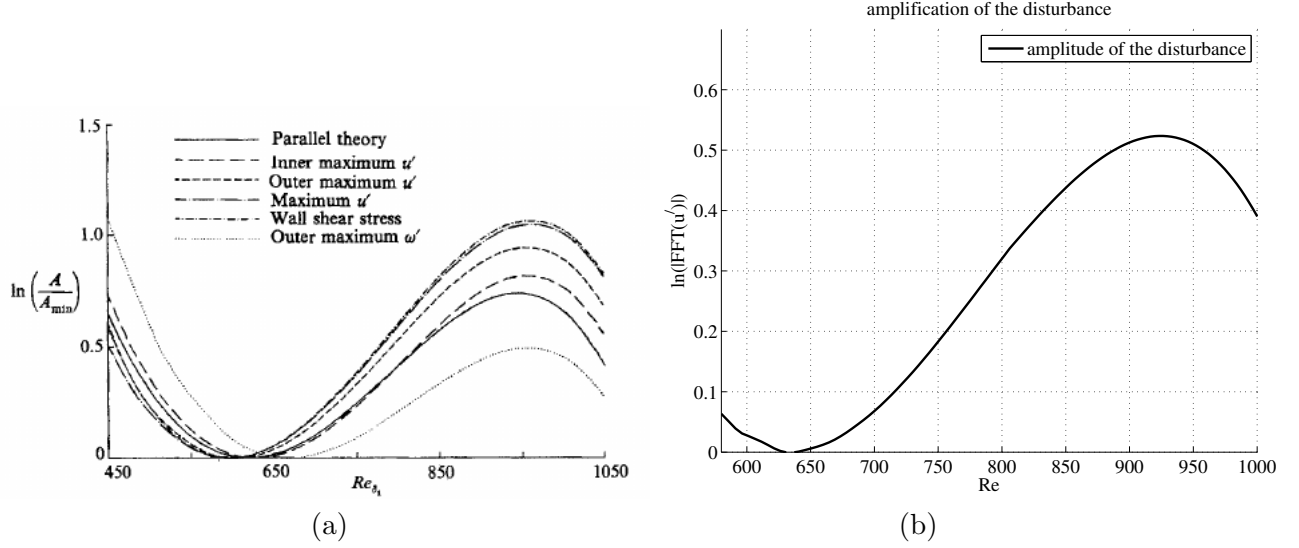


Figure 3.3: Tollmien-Schlichting amplification curves for incompressible boundary layer. (a) Reproduced from [40, pag. 331] and (b) DNS simulation.

Results for fundamental resonance on incompressible boundary layer are scarce in the literature. For comparison with DNS, [66] was used as reference. The perturbation function is defined as

$$v_{wall} = A_{1,0} \cos(\alpha(x - x_0)) \cos(\omega t) + A_{1,1} [\cos(\alpha(x - x_0) \pm \beta z)] \cos(\omega t) \quad (3.13)$$

Comparison of the amplification curves shown in figure 3.4(a) are in a very good agreement, for fundamental, oblique and harmonic mode. The vortical structures generated (figure 3.4(b)) are aligned as expected. In the spectrum shown in figure 3.4(c), can be seen the generation of harmonics, in frequency and spanwise modes.

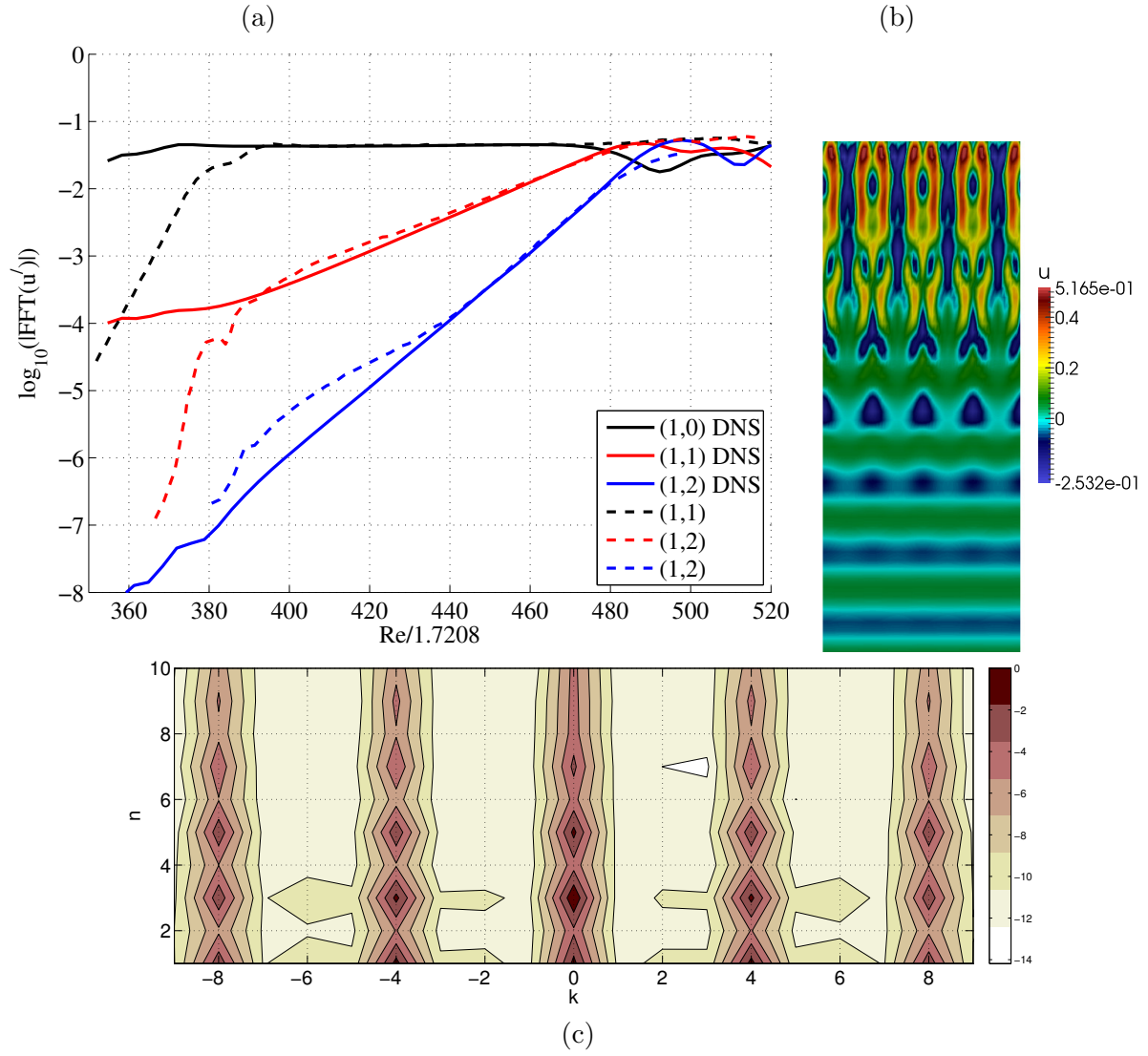


Figure 3.4: DNS simulation of Fundamental resonance. (a) comparison of amplification curves with [66], (b) Aligned vortical structures. (c) Amplification of harmonics.

In the subharmonic resonance, [36] was considered as reference case. The considered disturbance is:

$$v_{wall} = A_{1,0} \cos(\alpha_x(x - x_0)) \cos(\omega t) + A_{1/2,1} [\cos(\alpha(x - x_0) \pm \beta z) \cos((\omega/2)t)] \quad (3.14)$$

In figure 3.5(a) are compared the amplification curves for fundamental and oblique mode. Resultant vortex array (figure 3.5(b)) is organized in a staggered pattern, as expected for this mechanism. Finally in the spectrum (figure 3.5(c)), can be observed the generation of harmonics in frequency and oblique modes.

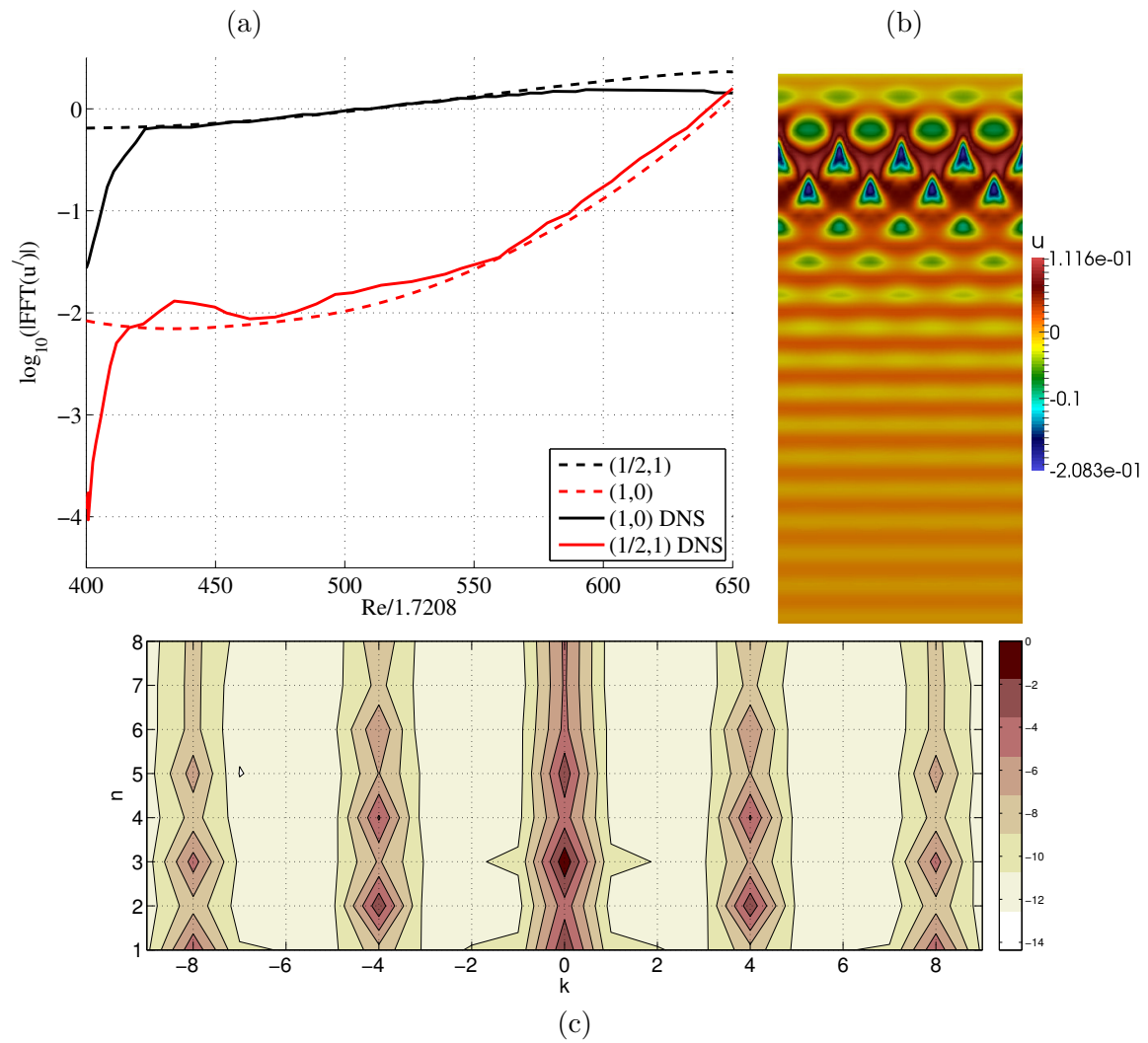


Figure 3.5: Comparison of Subharmonic resonance from [36] and DNS simulation. (a) Amplification curves, (b) staggered vortex pattern and (c) spectral content.

To test the code at nonlinear regime in compressible boundary layer, the subharmonic case at Mach 0.8 [49] was simulated successfully. Comparison of the amplification curves are shown in figure 3.6(a).

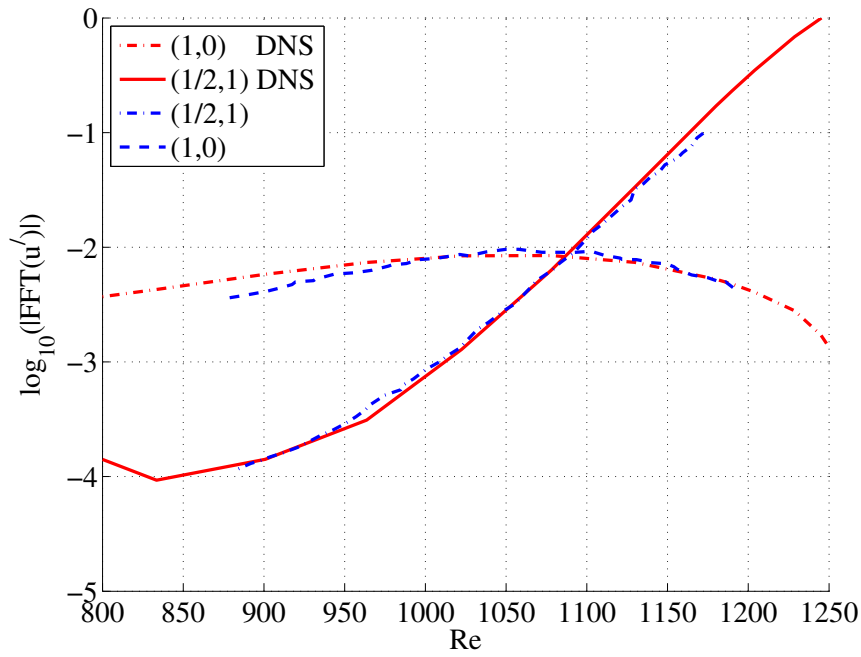


Figure 3.6: Comparison of fundamental and subharmonic waves reported in [49] and calculated with DNS.

Finally, the case reported by [32], for oblique resonance was performed, using as perturbation:

$$v_{wall} = A_{1,1}[\cos(\alpha(x - x_0) \pm \beta z)] \cos(\omega t) \quad (3.15)$$

The comparison of amplification curves for several modes, shown in figure 3.7(a) evidences a good agreement of DNS simulations with reference results. Longitudinal vortical streaks are generated (figure 3.7(b)) and in the spectra, it is observed amplification of the modes $(0, 2)$, typical of this kind of nonlinear resonance.

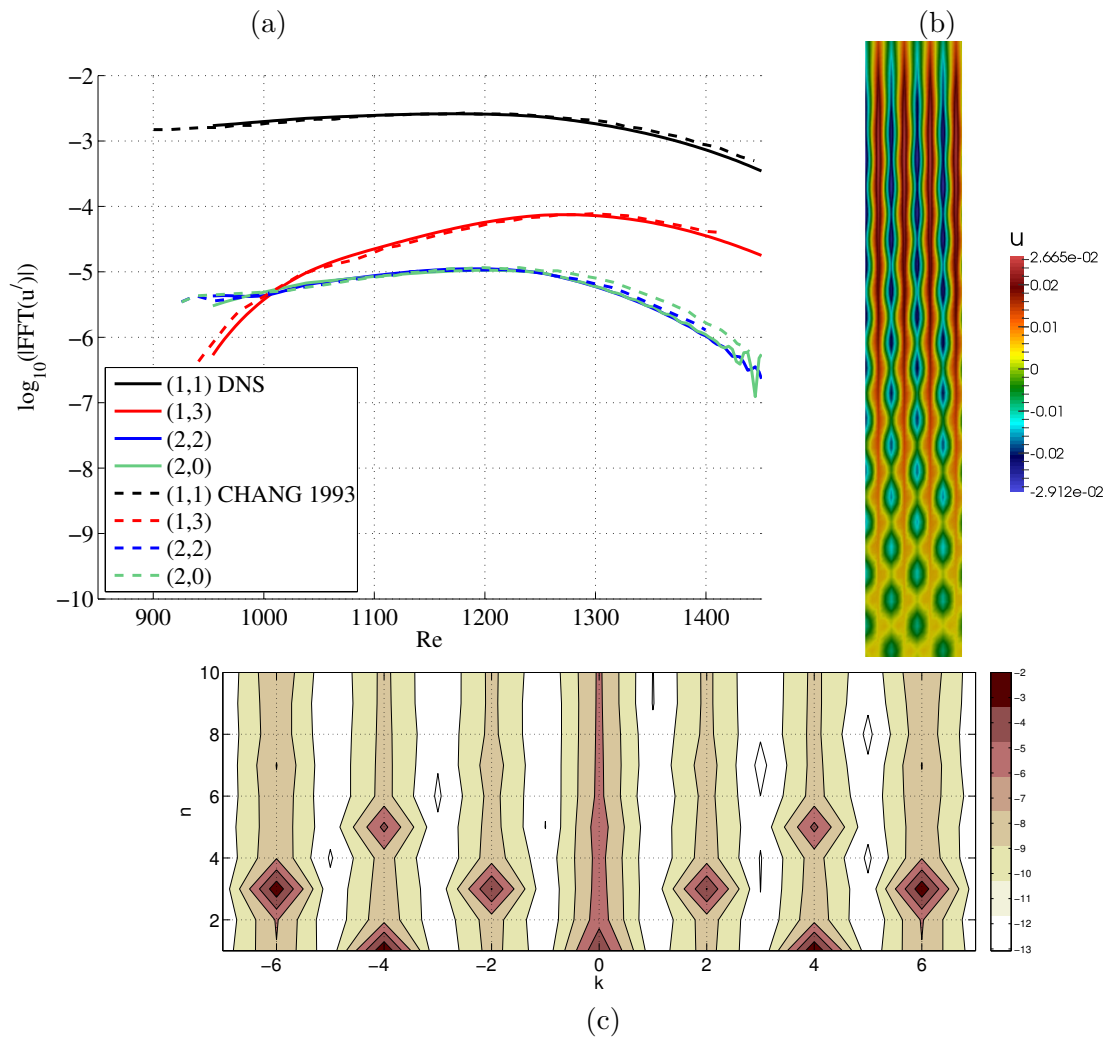


Figure 3.7: Comparison of amplification curves (a) for oblique transition reported in [32] and calculated with DNS. (b) Streaks in xz plane (c) spectrum $(k\beta_0, n\omega_0)$.

Chapter 4

DNS simulation of experimental wave packet in an incompressible boundary layer

4.1 Numerical set-up

4.1.1 Choice of reference experiment

In the literature, there are three main reference experiments of wave packets in incompressible boundary layer. In these experiments, the disturbance is introduced in the flow by a defined acoustic time signal driving a loudspeaker that was located at the center of the plate and communicated to the fluid with a small hole. [29] focused in the linear evolution for comparison with the theoretical linear model [28], which is valid for low amplitudes of the packet. In that experiment, the wave packet amplitude is of the order of 0.05% of the free-stream velocity, measured close to the outer amplitude peak of the Tollmien-Schlichting wave, in $y = 1.1\delta^*(x)$. The disturbance is a rectangular pulse in time, with amplitude and width as parameters. Initial subharmonic amplification is also observed in the last measurements points. In [14], the evolution from the linear wave packet to the formation of turbulent spots is investigated. In the evolution the packets amplitudes varies from 0.4% to 27% of the free stream velocity measured close to the inner amplitude peak of the Tollmien-Schlichting wave in $y = 0.6\delta^*(x)$. The disturbance was produced by a single period of a sinusoidal wave of frequency $24Hz$, chosen to coincide with the most linearly unstable 2D mode in the experimental arrangement. Later in [13], an analysis for individual modes is carried out on the experimental data which identifies nonlinear growth of the oblique modes. There, these modes are separated in three bands of frequencies, considering as reference the frequency of 2D linear dominant mode. The first band is centered around half the reference frequency (the subharmonic band), the second band contains modes around the reference frequency (the fundamental nonlinear band) and the third band represents higher frequency modes. Results show strong nonlinear amplification for these modes, however no attempt was made to find an explanation for the origin of the nonlinear fundamental modes.

In [54] low amplitude packets from %0.1 to 1% of the free-stream velocity measured close to the inner amplitude peak of the Tollmien-Schlichting wave are tracked to focus on subharmonic amplification, effect of phase [53] and later on amplification of modes related to fundamental resonance [52]. Disturbance is generated by the superposition of 80 Fourier modes, using $f_0^* = 5Hz$ as fundamental frequency and covering the unstable linear band. In [54] the measurement streamwise positions are between 400mm and 1300mm, spaced by 100mm.

The parameters of the experiments of [14] and [54] are shown in table 4.1, where index 0 refers to the position where the excitation was introduced, z_d indicates the spanwise domain and $\%u_{Re_{1450}}$ a percentage estimate of disturbance amplitude close to the perturbation source (an indication of the initial amplitude of the disturbance), at the experimental position with local Reynolds number $Re \sim 1450$, which corresponds to the positions $x^* = 1600mm$ and $x^* = 600mm$ on each experiment respectively. The experiments display similar non-dimensional conditions, but [53, 54] presents substantially lower excitation amplitudes. As a consequence of amplitude choice in both experiments, the last experimental measurement points have similar local Reynolds number Re_{max} , but, in [14] turbulent spots are observed in this position, while in [54] moderate nonlinear behavior is observed. Some of these experiments have been reproduced numerically for comparison and to extend its results. [29] experiment is simulated by [40, 76] and [14] experiment is simulated by [96]. A DNS simulation of the experiment [54] is not available in literature at present. It is expected that lower amplitude excitation are better representations of real aircraft conditions. Because of this, the experiment of [53] was chosen as a reference for the current study. Moreover the experimental data was available to this study and had more information on the weakly nonlinear regimes which was the focus of the current work.

Table 4.1: Experimental Parameters

	Experiment Cohen (1991)	Experiment Medeiros (1999)
U_∞	6.65m/s	17.3m/s
x_0^*	800mm	203mm
ν^*	$1.49 \times 10^{-5} m^2/s$	$1.49 \times 10^{-5} m^2/s$
δ_0^*	$2.13 \times 10^{-3} m$	$7.195 \times 10^{-4} m$
Re	1035	835
Re_{max}	2150	2114
x_{max}^*	3500mm	1300mm
z_d^*	$\pm 40cm$	$\pm 18cm$
$\%u_{Re_{1450}}$	0.4%	0.2%

4.2 Disturbance Generation

Usually, in experiments and simulations of wave packets, the frequency spectrum of the perturbation is carefully controlled, while less attention is given to the spanwise spectrum, which experimentally is also more difficult to control. In the present simulations, the perturbation is constructed with the superposition of a selected band of frequencies and spanwise modes, all with the same energy, covering the linear unstable band defined by the stability diagram .

For the simulation, 80 frequencies are considered, $N_n = 80$, and 80 symmetric spanwise wave numbers ($N_k = 40$), in addition to the corresponding two-dimensional modes. The time signal of the excitation was identical to that used by [54]. In the physical space, the resulting signal in time and spanwise direction is a function similar to $\frac{\sin(x)}{x}$. In the streamwise direction the disturbance had a shape of one period of the coseno function. The perturbation is applied in the wall normal velocity component. In summary, the so called pulse excitation used in the current study is then defined as

$$v' = A_{3D} \sum_{n=1}^{N_n} \sum_{k=-N_k}^{N_k} [\cos(\alpha_0(x - x_0) \pm k\beta_0 z) \cos(n\omega_0 t)] \quad (4.1)$$

with A_{3D} the amplitude of each modes.

Using the dimensional parameters given in table 4.1 for the experiment [53], the non-dimensional flow parameters used in the DNS simulation are $Re = 835$ and $Pr = 0.71$. Although experimental the Mach number is 0.05, in the DNS simulation Mach 0.2 was used, because by increasing Mach number the numerical time steps can be increased and a lower number of iterations are needed to complete the simulation. This value has already been used in other works on transitional incompressible boundary layer (e.g [67]). We also performed tests at lower Mach numbers and demonstrated that the results of $Mach = 0.2$ are essentially incompressible. Tests also performed in this study show that at Mach 0.3 some significant compressible effects arise. With the reference parameters used in the simulation, the experimental measurement domain in non-dimensional variables was defined by:

$$\begin{aligned} x_0 &= 284 \\ 0 \leq x &\leq 1300mm/\delta_0^* = 1808 \\ 0 \leq y &\leq 0.6\delta^*(x) \\ L_z &= 36cm/\delta_0^* = 250 \\ f_0 &= 5Hz \times (u_\infty/\delta_0^*) = 2.0796 \times 10^{-4} \\ \omega_0 &= 2\pi f_0 \times (u_\infty/\delta_0^*) = 0.0013066 \\ \beta_0 &= 2\pi/(36cm/\delta_0^*) = 0.0126 \\ y &= 0.6\delta^*(x) \end{aligned}$$

From these values the computational domain was defined considering extra size dimensions to avoid boundary condition effects into the region of interest. The integration domain is:

$$\begin{aligned} 0 \leq x &\leq 2000 \\ 0 \leq y &\leq 20 \approx 2.5 \times \delta_{99}(x = 2000) \\ -1.75 \frac{2\pi}{\beta_0} \leq z &< 1.75 \frac{2\pi}{\beta_0} \end{aligned}$$

The boundary layer thickness δ_{99}^* can be written in terms of δ_0^* as $\delta_{99}^* = 5\sqrt{\frac{x}{Re}}\delta_0^*$.

Test were performed to ensure that this domain was sufficiently large to represent a semi-infinite flat plate immersed in the a uniform flow. In the experiment, the time signal perturbation was composed by a superposition of 80 Fourier modes with fundamental frequency $f_0^* = 5Hz$. In the non-dimensional variables of the DNS simulation, the perturbation frequency band is: $0 \leq \omega \leq 80\omega_0 = 0.10453$ The spanwise wave number band is $-40\beta_0 \leq \beta \leq 40\beta_0$, equivalent to $-0.504 \leq \beta \leq 0.504$.

In the computational domain in the streamwise direction, the perturbation has a format given by one period of the coseno function, $\cos(\alpha_0(x - x_0))$, with $x_0 = 284$ the center of the perturbation in non-dimensional variables. $\alpha_0 = 2\pi/32$ was chosen to be a representative streamwise wave number of the most linearly unstable mode in the Reynolds number range studied. Figure 4.1 shows the perturbation in physical and Fourier space.

Some important relations are

$$Re_{\delta^*(x)} = 1.7208\sqrt{xRe}, \quad F = 10^4 \frac{\omega}{Re}, \quad Re_x = xRe \quad (4.2)$$

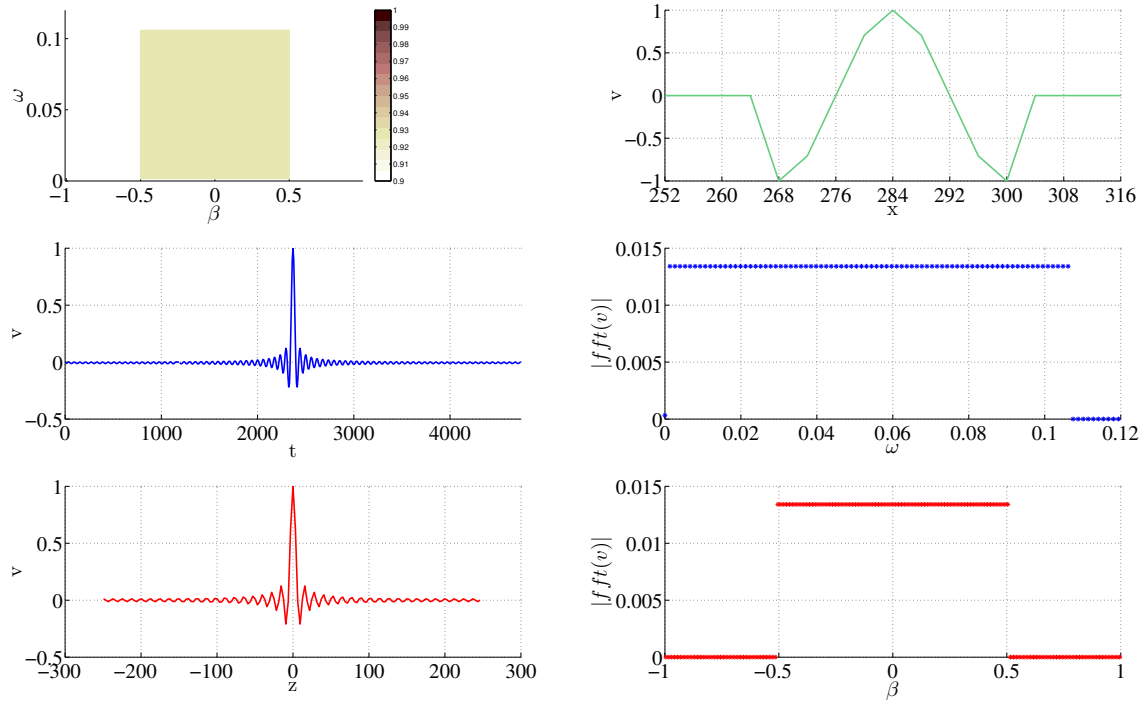


Figure 4.1: Perturbation composition, (a) two-dimensional spectrum, (b) format in streamwise direction, (c) and (d) time signal and spectral composition. Spanwise perturbation (e) and spectrum (f).

In the x - z plane the perturbation has the format:

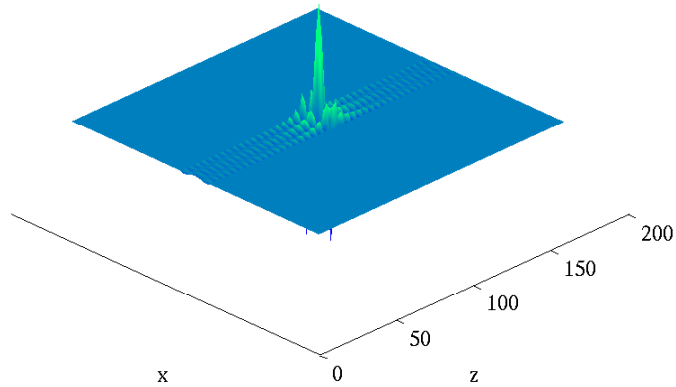


Figure 4.2: Perturbation format in x - z plane.

4.2.1 Grid independence tests

Grid resolution in x and z direction are more demanding for nonlinear than for linear regime of transition in boundary layer [82]. In the streamwise direction three grid resolutions were tested for wave packet simulations, namely, $dx = 4$, $dx = 2$ and $dx = 1$. For wave packet, however, tests performed show substantial grid dependence in the the nonlinear regime for $dx = 4$. In the figure 4.3 results are shown along the streamwise direction for a fixed spanwise position as well as along the spanwise direction for a fixed streamwise position. The comparison of resultados for the two grids show that for $dx = 2$ the results are fairly grid independent up to later stages of the weakly nonlinear regime, which is the focus of the current work. In the following simulations, a grid with $dx = 1$ was employed for the calculations. A more refined grid was not possible to simulate with our current computational resources, due to high computational and storage cost. In the wall normal direction tests were performed for TS-waves in the defined computational domain (see figure 4.4), and can be concluded that for $y_{max} = 20$ the grid $ny = 51$ is converged. In spanwise direction, the resolution of 4 points per-wavelength was sufficient for grid independence (figure 4.5). The grid employed in the wave packet simulations was $nx = 2001$, $ny = 51$, $nz = 280$. The value of nz was chosen to have resolution of four points per wave length in the mode $40\beta_0 = 0.504$, which is the higher spanwise wave number considered in the experiment.

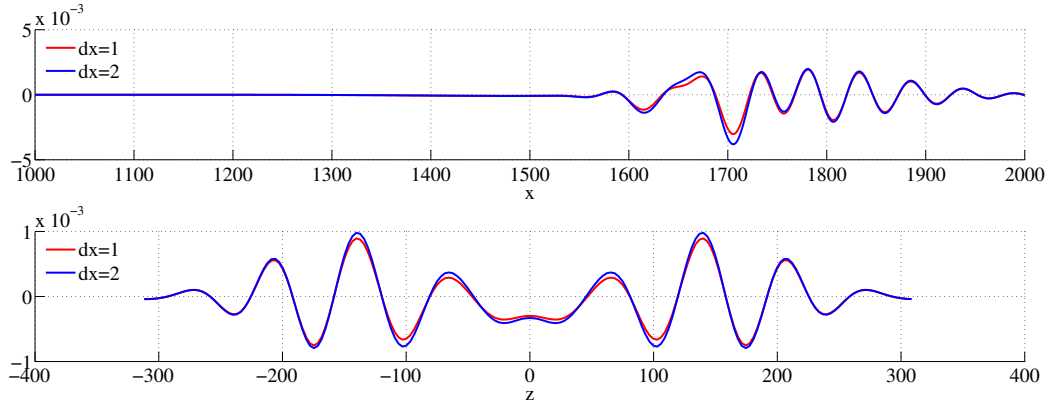


Figure 4.3: Test for grid independence in wave packet simulations.

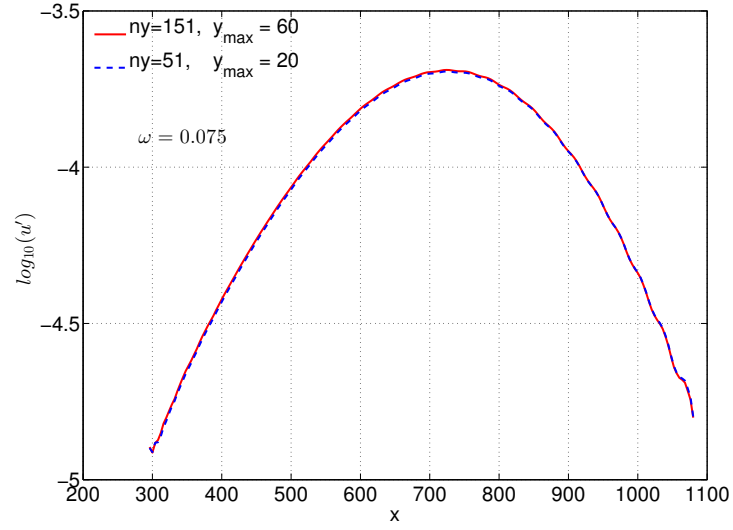


Figure 4.4: Test for grid independence in y-direction for a TS-wave, $\omega = 0.075$ in computational setup for experiment simulation.

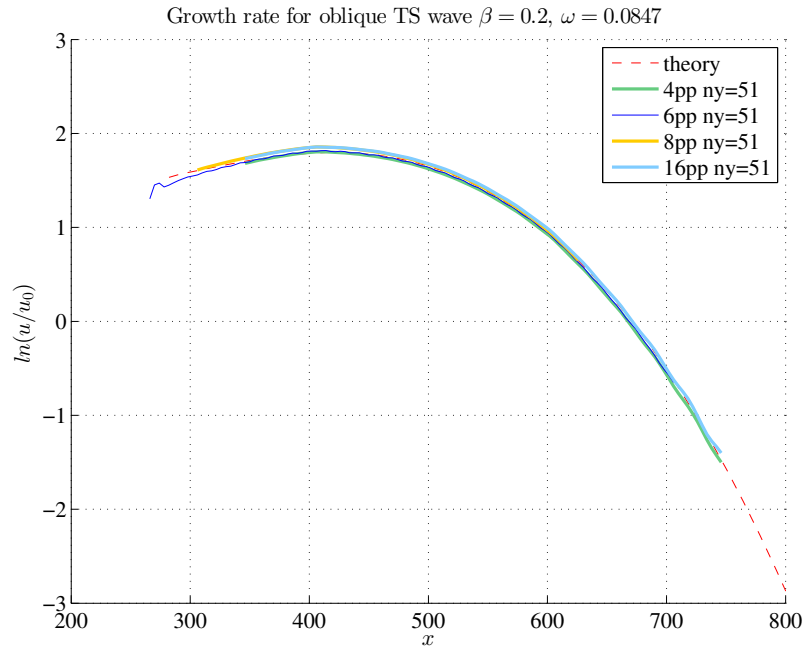


Figure 4.5: Grid independence tests in spanwise direction for an oblique wave with $\omega = 0.0847$ and $\beta = 0.2$.

4.3 DNS results

This section is organized as follows. First a small amplitude packet was simulated to produce a linear evolution of a packet to serve as a reference for the nonlinear studies that followed. This constitutes the next subsection. Then the experiments of [53] were reproduced numerically to demonstrate that the simulations were a good representation of the actual physical observations. Next, the numerical results were analyzed in detail to try to establish firm conclusions regarding the nature of the nonlinear regime observed and the possible differences from the here-called controlled transition. Finally possible causes for some small differences between the numerical and experimental results were investigated.

4.3.1 Linear wave packet

A low amplitude (linear) packet evolution is shown in figure 4.6. Perturbation amplitude is below 10^{-5} . In incompressible boundary layer the packet displays the characteristic crescent shape with a weak modulation in spanwise and streamwise directions. Results in the spectral space can also be obtained, and are discussed in the next section (figure 4.11 (a)), together with results for the nonlinear wave packet, for which the linear one serves as reference. In the global nondimensional variables, the frequency of most amplified mode decays in downstream, as can be seen in figure 4.7.

4.3.2 Comparison of numerical with experimental wave packet

For numerically reproducing experimental results of hydrodynamic instability it is crucial to reproduce the same excitation amplitude. Here this was achieved by adjusting the numerical excitation amplitude to match the experimental results at some position in the linear regime. In the experiment, the linear stages of the packet evolution are observed up to 600mm. For the nonlinear simulation, the excitation amplitude was adjusted to match the experimental results at $x=600\text{mm}$.

In figure 4.10, at the experimental measurements points, the streamwise velocity time signal at the center-line is compared for experimental and numerical results. The agreement is remarkable, in particular in view of the very small amplitudes of the signals, about 0.1% of the free stream velocity. Significant differences are found only in the last positions, where strong nonlinear action is present. Yet, even at these stations the agreement can be considered good in general.

Figure 4.8, shows nonlinear evolution in physical space on planes parallel to the wall. A weak three-dimensional structure becomes stronger as the nonlinear effects increase downstream. Differences between linear and nonlinear regimes are clearly shown in figure 4.9.

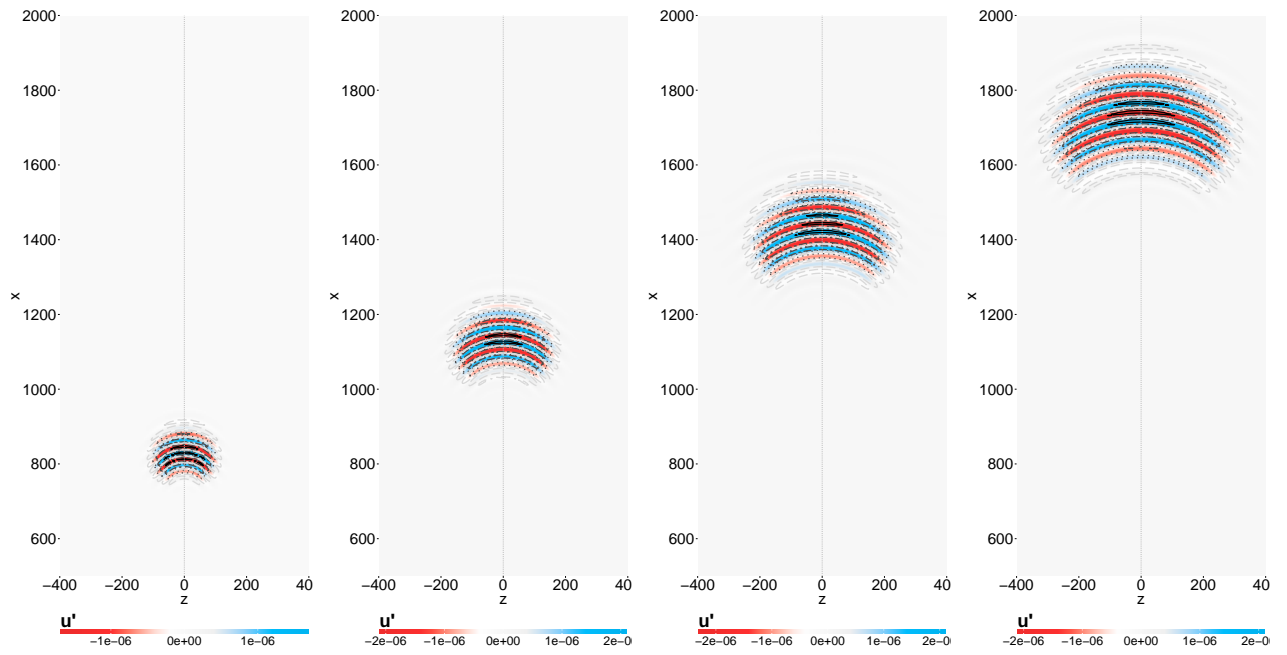


Figure 4.6: Linear wave packet at Mach 0.2, in $y = 0.6\delta^*$. Contour levels at 90% (—) , 50% (-.-), 30% (...) and 10% (- -) of the amplitude peaks in the packet.

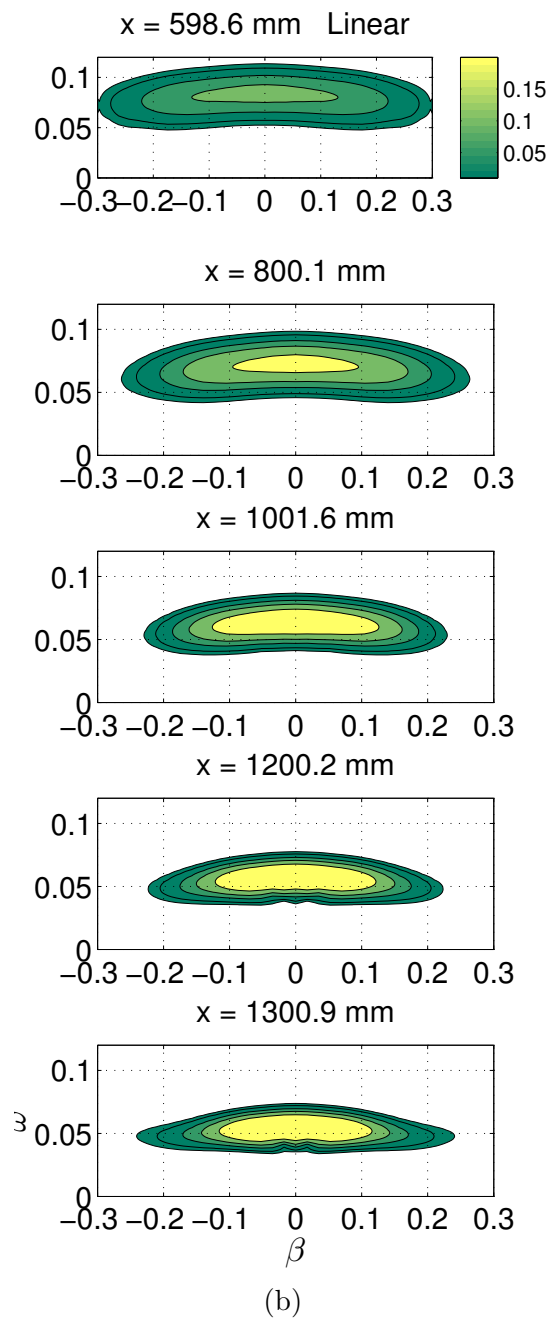


Figure 4.7: Spectrum evolution of linear wave packet. In global dimension... frequency of the most amplified mode decays in downstream.

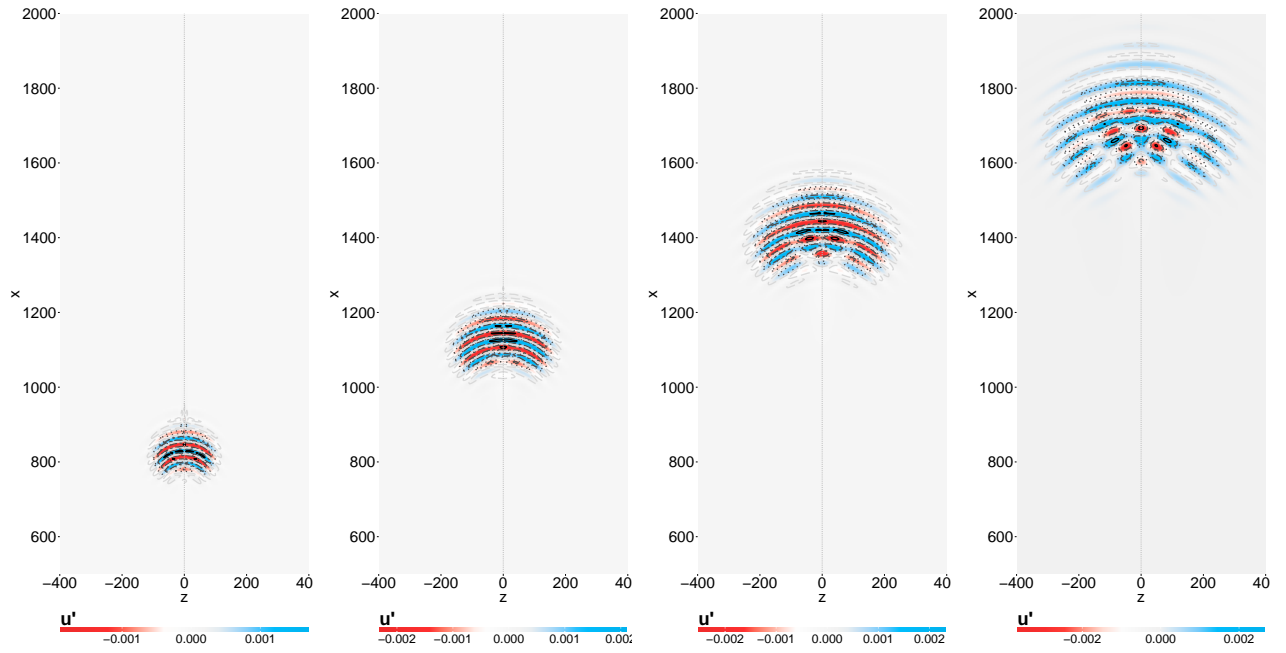


Figure 4.8: Nonlinear wave packet evolution at Mach 0.2, at $y = 0.6\delta^*$. Contour levels at 90% (—) , 50% (— · —), 30% (...) and 10% (— —) of the amplitude peaks in the packet.

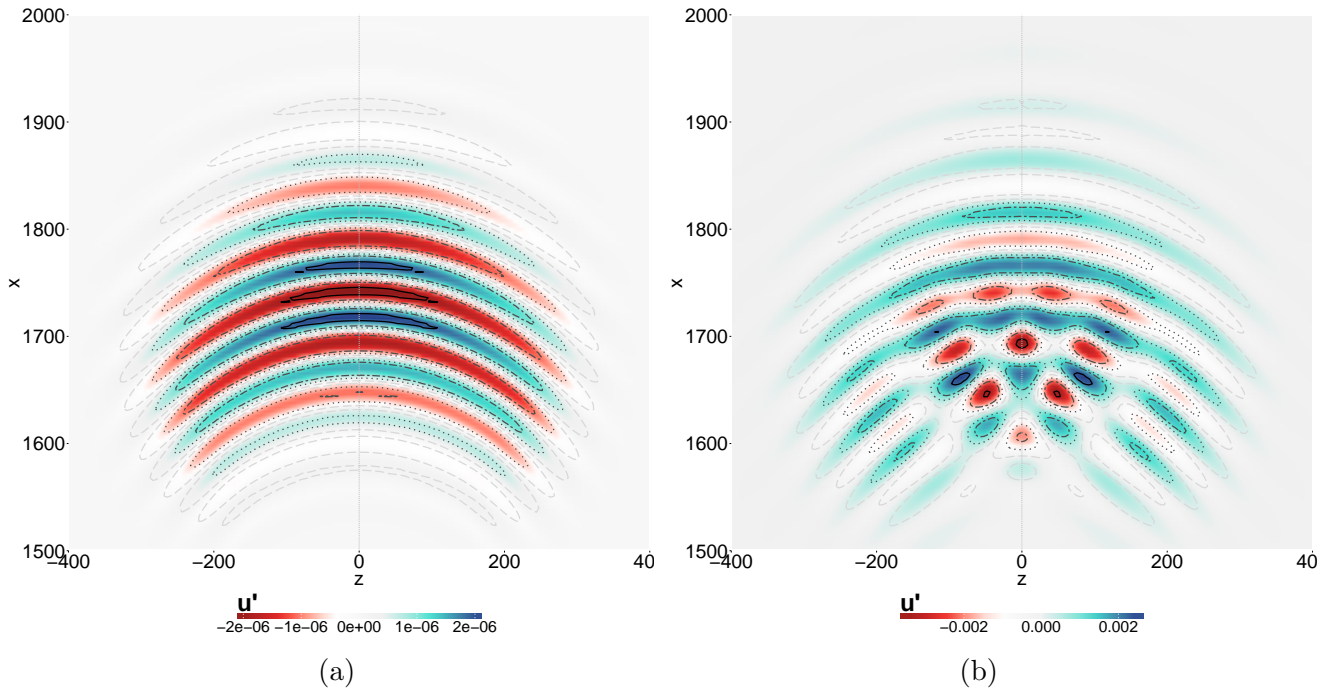


Figure 4.9: Comparison of linear (a) and nonlinear (b) wave packet at advanced position at $y = 0.6\delta^*$. Contour levels at 90% (—) , 50% (— · —), 30% (...) and 10% (— —) of the amplitude peaks in the packet.

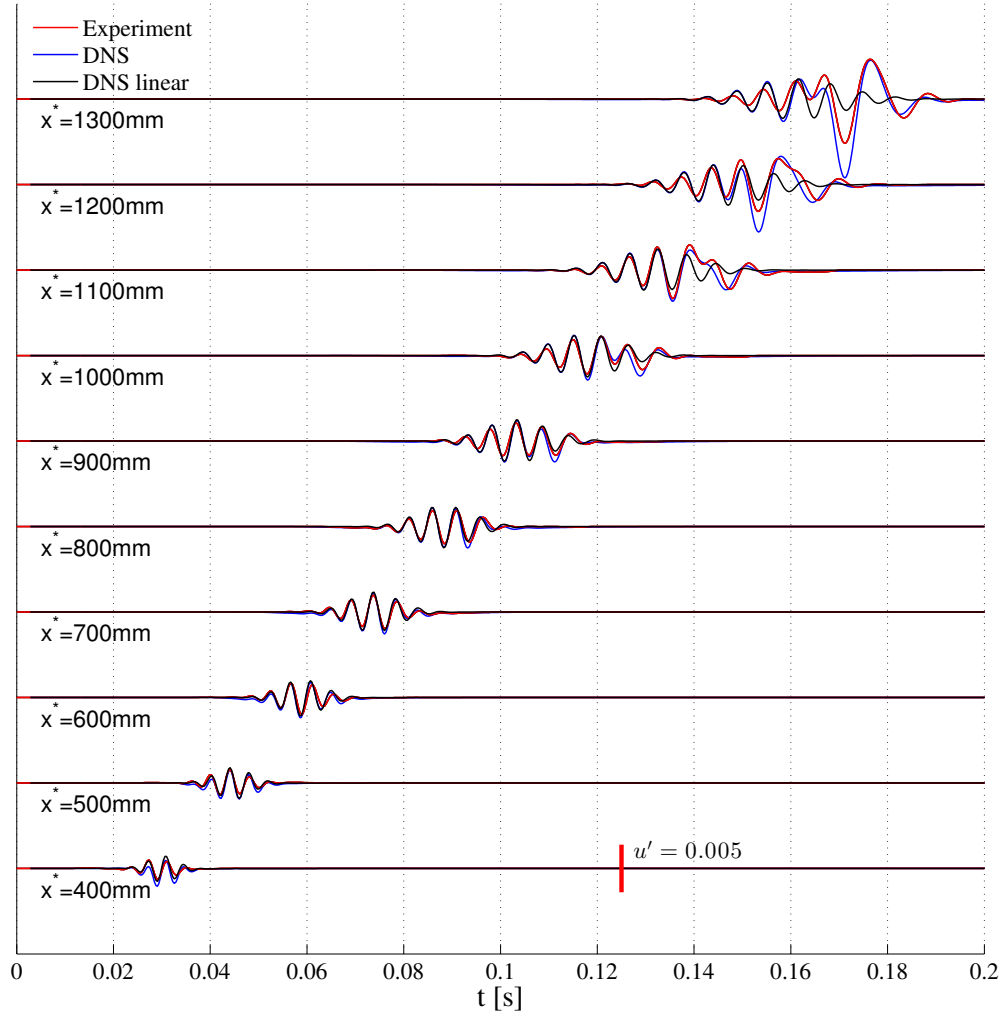


Figure 4.10: Comparison of velocity time signal at the centerline, at all experimental measurement points [53] with DNS simulation.

In figure 4.11 the spectral evolution is compared for DNS linear, DNS nonlinear and experimental wave packet, considering local nondimensional variables, using as reference length $\delta^*(x)$. Better comparisons are also provided in figure 4.12 for $x^* = 1200mm$. Comparison of DNS simulation with experiment in spectral domain also shows, in general, a good agreement. However, there are some significant differences, namely, experimental asymmetry and nonlinear fundamental and low frequency modes that are weaker in the simulations. These differences will be addressed later in the analysis.

An important aspect in performing the analysis is that for direct comparison with experimental results, in the post process of DNS results, the u component of the velocity was interpolated using a spline method into the experimental measurement points, defined in section 4.2.

The computational domain has a larger size and higher spatial resolution in the three coordinates. The interpolation was done only for comparison with experiments, for other analysis DNS domain and resolution was used.

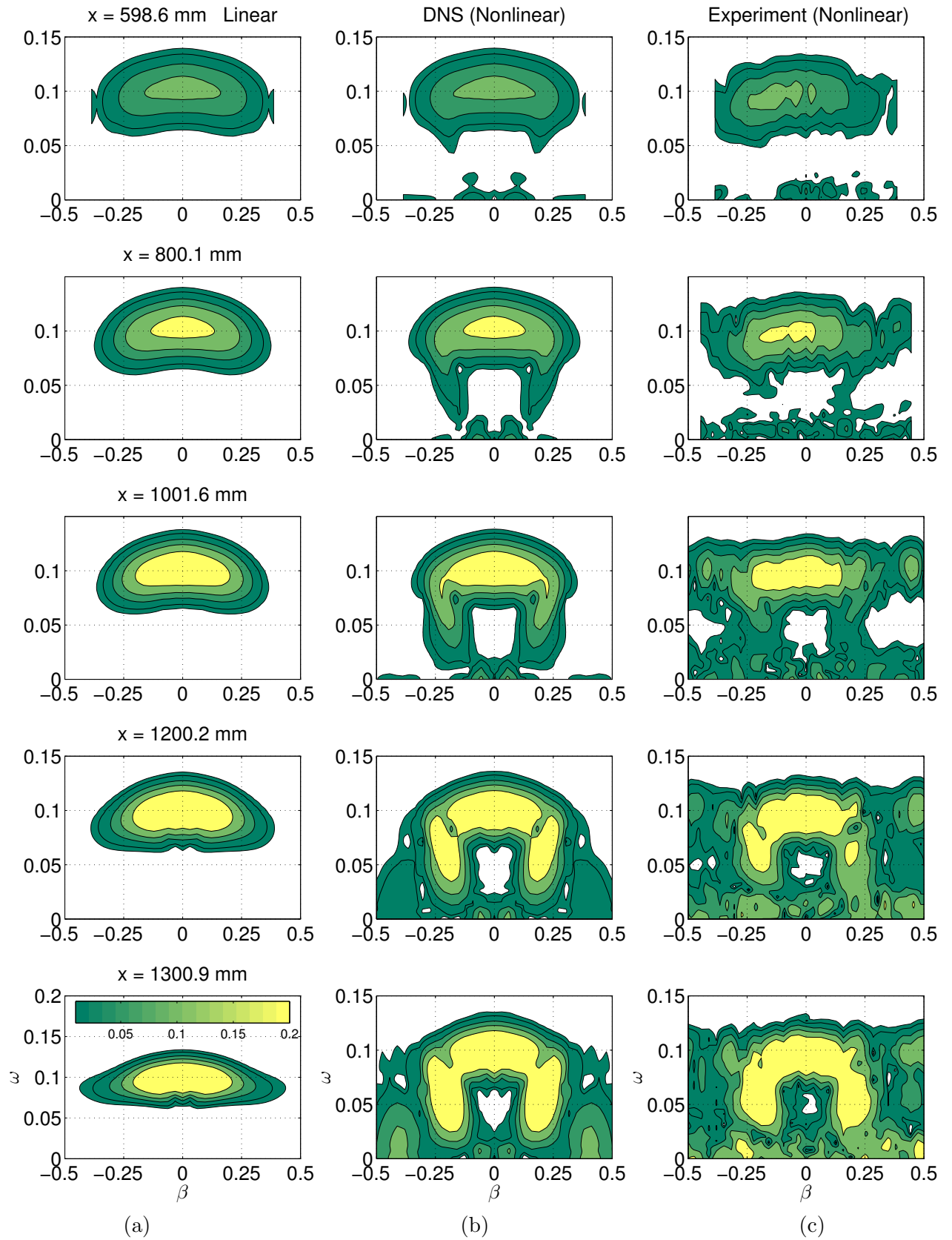


Figure 4.11: Comparison of spectral evolution at several measurement points for (a) linear DNS (b) non-linear DNS and (c) experimental wave packet.

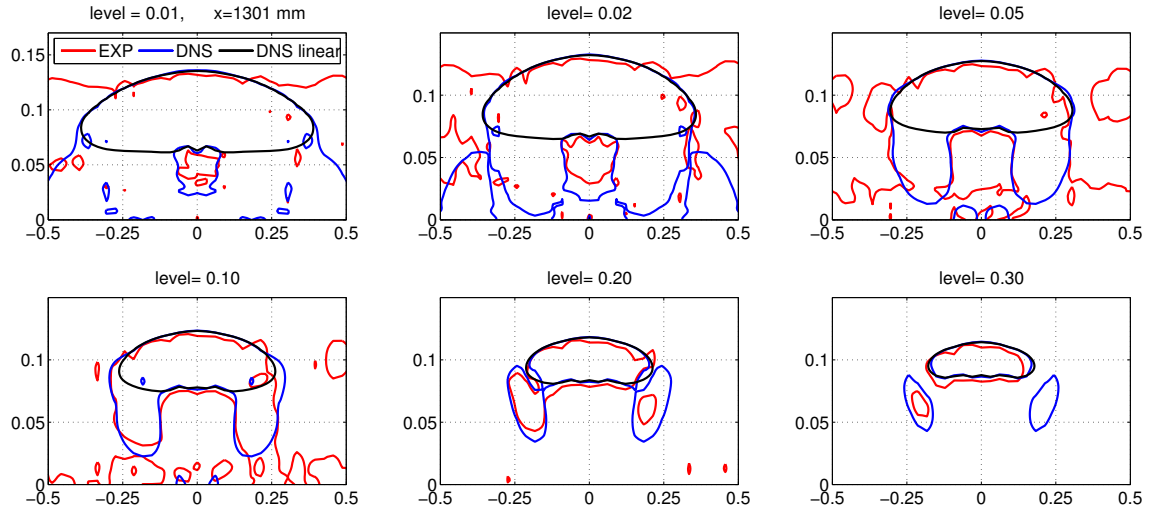


Figure 4.12: Comparison of contour levels of linear, DNS and experimental spectrum in the nonlinear position, $x^* = 1200mm$.

Moreover, interpolation of numerical results into the experimental physical domain (figure 4.13), suggests that the experimental domain might have been a little small in the spanwise direction.

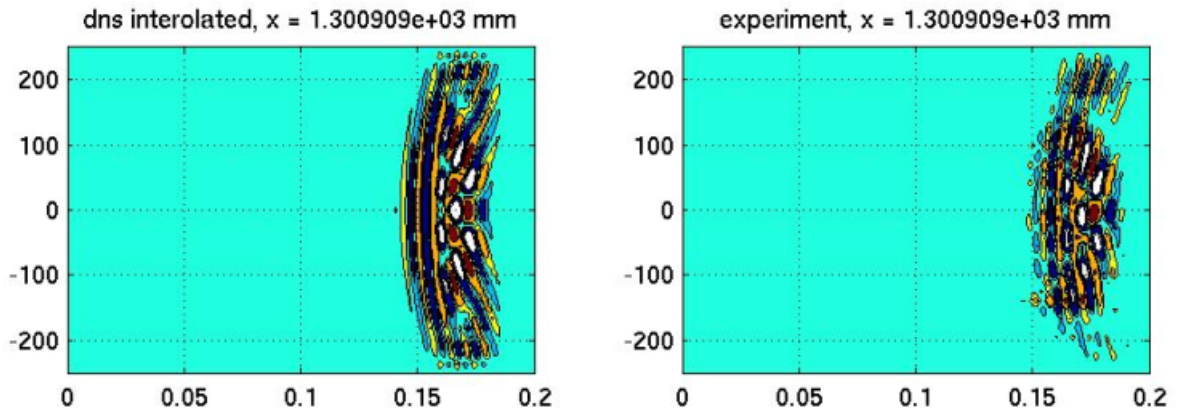


Figure 4.13: Comparison in the experimental domain at $x^* = 1300mm$.

4.4 Nonlinear modal analysis of DNS results

In the nonlinear case it is possible to distinguish four important types of modes, here called linear, subharmonic, nonlinear fundamental and low frequency modes, as illustrated in figure 4.14. The subsequent analysis investigates the subharmonic and nonlinear fundamental band separately.

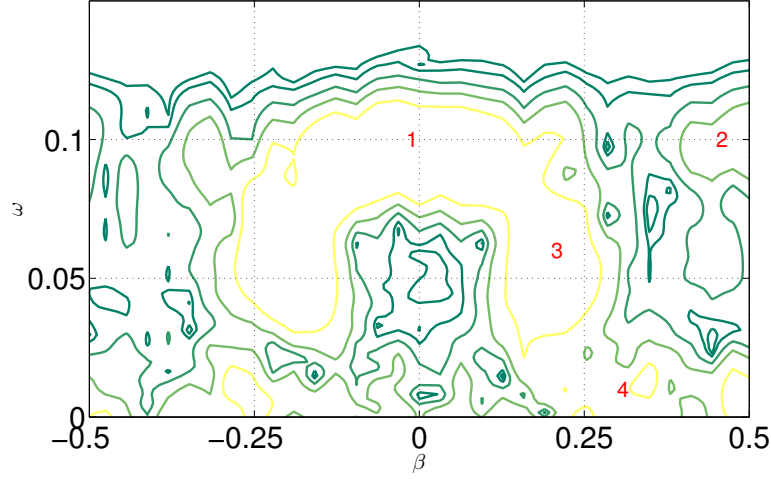


Figure 4.14: (1) linear (2) fundamental (3) subharmonic and (4) low frequency bands.

4.4.1 Subharmonic bands

In figure 4.15, the frames on the left column display amplitude evolution of isolated modes in the packet. The subharmonic modes displayed are indicated by the circles in the contour plots of the wave packet spectrum at position $x^* = 1200mm$. A mode maintain a constant dimensional frequency along the evolution, while results of hydrodynamic instability in the boundary layer are normally plotted in non-dimensional variables based on local boundary layer parameters, which, hence, change along the evolution of a mode. To emphasize that the evolution shown holds for modes, the modes are identified by their spanwise wave number index k and frequency index n , which, for the signal processing used, remain the same along the evolution. The selected subharmonic modes are shown in two groups, one displayed in the top frames the other in the bottom frames. In the frames showing the amplitude curves, the thick continuous blue line represents the fundamental 2D mode with twice the frequency of the subharmonic band. This would be the linearly unstable mode driving a possible subharmonic resonance that is investigated. The red dashed lines correspond to the nonlinear evolution of the subharmonic modes. The dashed green lines correspond to the linear evolution of the same subharmonic modes, obtained from the above discussed linear simulation that was performed for reference. Clearly, the subharmonic modes display a nonlinear behavior that renders them substantially more unstable with respect to the linear evolution. Several modes that are linearly stable display nonlinear instability.

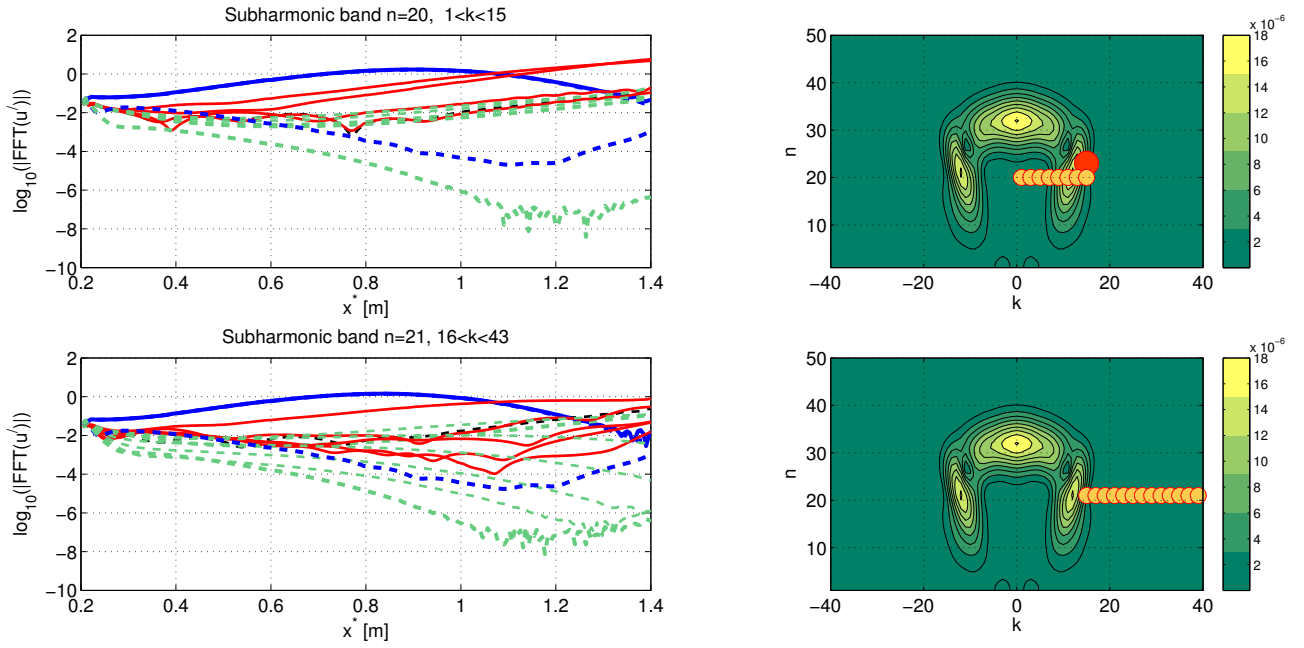


Figure 4.15: Amplification curves for subharmonic bands of linear (green lines), nonlinear (red lines) and fundamental (blue lines) modes.

As discussed in the literature review, the subharmonic instability in a wave packet is an issue not entirely settled, with several aspects deserving more definite conclusions. What follows is an attempt to fill this gap. Nonlinear behavior becomes evident with phase locking (figure 4.16), when this occurs both modes, fundamental and subharmonic reach same phase speed. However in this case, this is not shown clear because from beginning both modes have same phase speed.

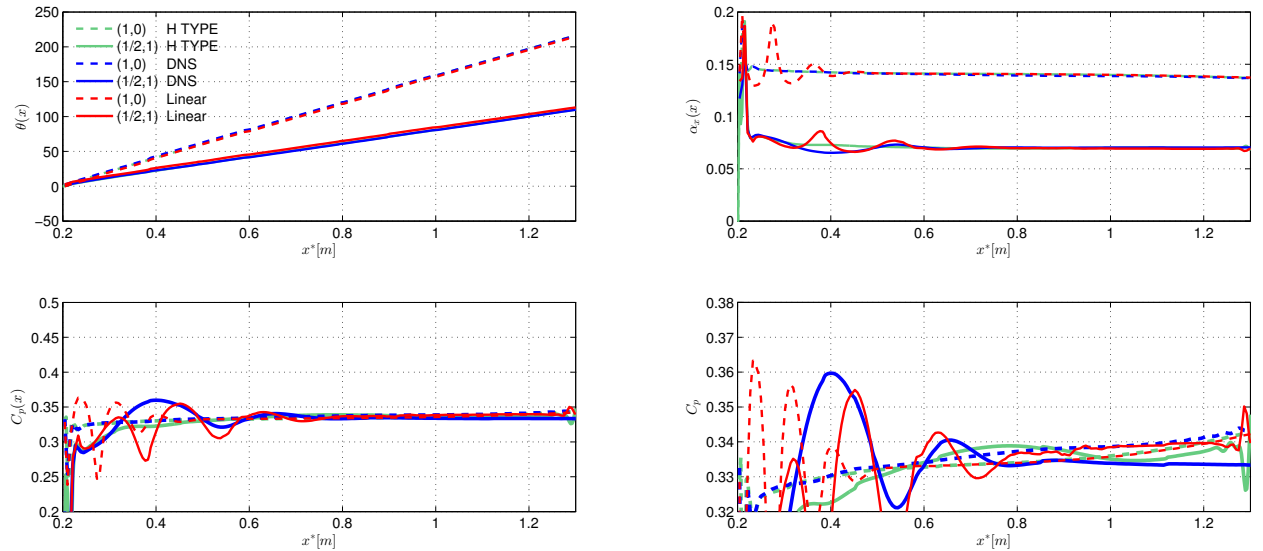


Figure 4.16: (a) Phase, (b) streamwise wave number, (c) phase velocity for subharmonic resonance, (d) zoom of (c), for the mode $\omega/2 = 0.059260$, $\beta = -0.2218$, chosen from experimental spectrum at $x^* = 1300mm$.

One important aspect in subharmonic instability is that there is an amplitude threshold for the primary driving wave for which instability sets in. In boundary layers, as the primary waves grow, the subharmonic growth rates increase. If the primary wave is not too large, it crosses the second branch, reaching its maximum amplitude and then decaying, while the subharmonic wave keeps growing. The subharmonic wave reaches its maximum amplitude where the primary wave reaches the threshold amplitude again, but in its decaying arm. Hence the maximum amplitude of the subharmonic wave occurs downstream from the maximum amplitude of the primary driving wave.

Figure 4.17 helps to illustrate this concept in the wave packet. The top frame indicates the subharmonic mode tracked. For a packet in the boundary layer, the linearly unstable frequency band changes with the packet evolution. Its frequency reduces as the Reynolds number based on global parameters increases (see figure 4.7). A similar pattern may be observed for the subharmonic waves, although not so clearly.

For the analysis in figure 4.17, the subharmonic mode chosen was a subharmonic band peak at position $x = 1200mm$, which is a neighbor mode of the modes examined in figure 4.16. This streamwise position was chosen for clarity. Figure 4.17, bottom frame, shows the evolution of the subharmonic mode in the nonlinear packet (red dashed line). It also shows the primary driving wave obtained from the nonlinear simulation (continuous red line) and the same wave obtained from a linear simulation (continuous blue line). The dashed blue line is the linear evolution of the subharmonic wave, which is shown with two lines shifted in the vertical direction. The first aspect to discuss in the figure is that the primary wave is virtually unaffected by the nonlinearity. The picture indicates further that the nonlinear subharmonic wave departs from its linear behavior at a position about $x = 0.25m$. The picture also shows that at some position downstream the nonlinear subharmonic wave settles back to its linear behavior. The amplitude of the primary wave at which the subharmonic departs from linear behavior and returns to it are also indicated in the figure, and they are virtually identical. Overall the results convey the idea of a nonlinear process of a subharmonic wave which is governed by the amplitude of the primary wave and has a well defined threshold amplitude. Moreover the primary wave remains unaffected by the nonlinear activity. The observations are consistent with a subharmonic instability driven by a small amplitude primary wave. It is interesting to mention in passing that the subharmonic wave does not reach its maximum amplitude at the decaying threshold point, owing to the fact that at that x location the nominally subharmonic waves have already become linearly unstable. The results is shown for a selected mode, but it is representative of a large portion of the modes belonging to the subharmonic band.

Yet, further evidence of subharmonic instability can be offered, figure 4.18 The figure shows the amplitude evolution of the modes indicated in the two-dimensional spectral contour plot. The amplitude evolution are given for experimental (red lines) and nonlinear numerical (blue lines) results, and agree very well with one another. Results are also given for the corresponding linear evolution (black line). Once more, the primary wave is unaffected by nonlinearity while the subharmonic wave becomes nonlinear very early in its evolution. The green lines represent a control case, meaning, a two dimensional wave with the frequency of the other primary waves shown in the plots and a pair of subharmonic waves with the same frequency and spanwise wave numbers of the other subharmonic waves displayed in the plot. The amplitude of the primary wave in the controlled case was chosen to match the nonlinear subharmonic wave growth rate in the packet. Indeed the matching is fairly good, and indicates that the phenomenon observed in the packet corresponds to subharmonic resonance of a primary wave at some amplitude. The amplitude of such primary wave is not that of the 2D fundamental wave composing the packet.

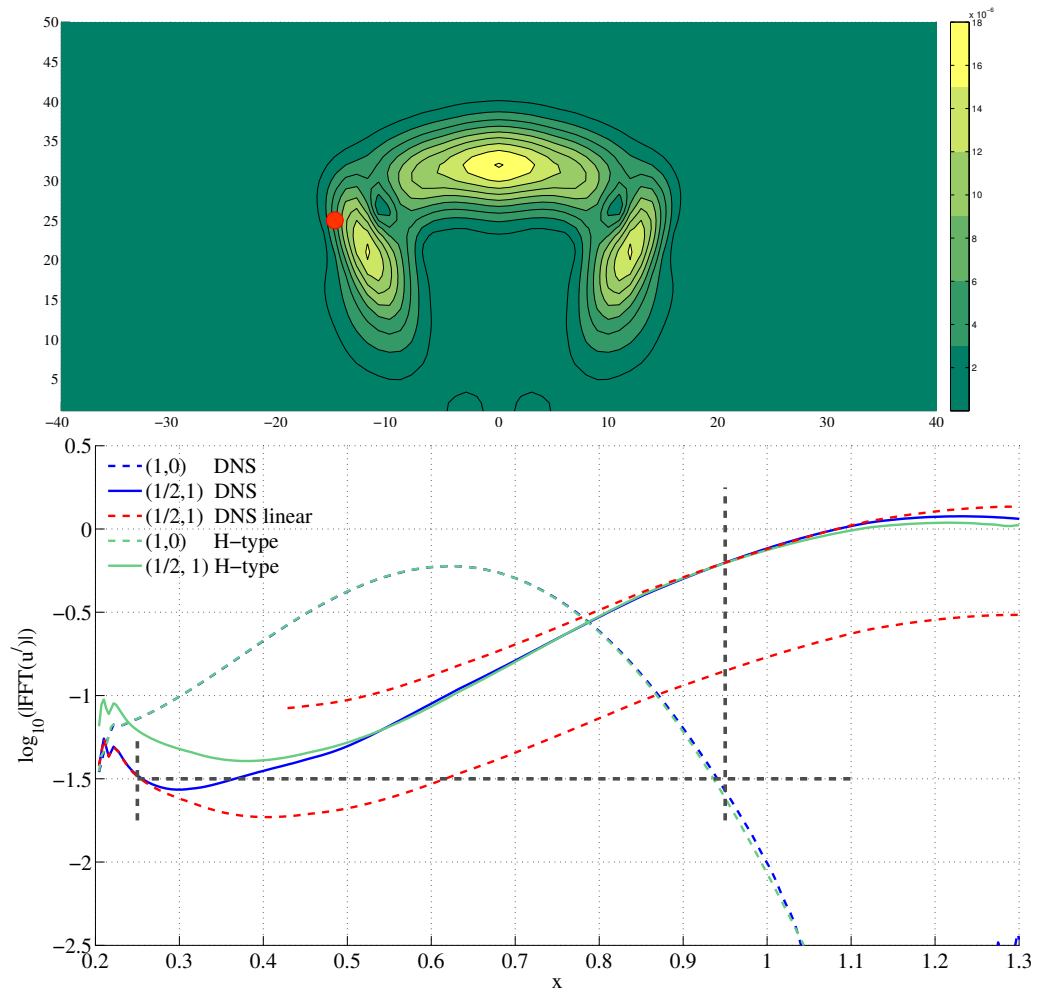


Figure 4.17: (a) Selected mode in the subharmonic band. (b) Effect of threshold amplitude of the driving mode (1,0) (indicated by the gray dashed lines) on the subharmonic resonance. Nonlinear growth rate for the mode (1/2, 1) calculated by H-type controlled transition, matches with the growth rate for the selected mode in the packet.

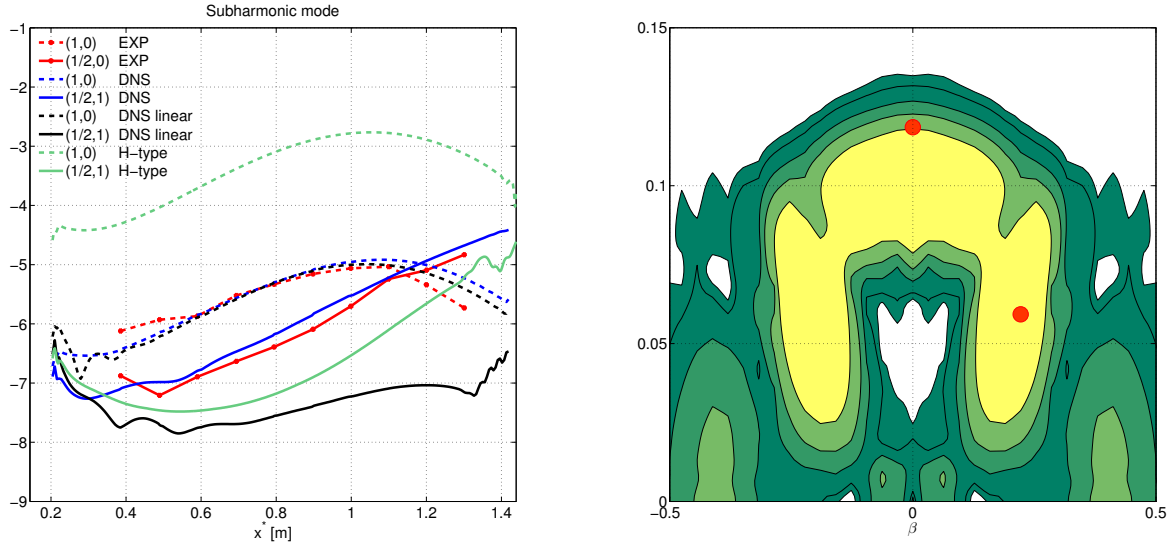


Figure 4.18: Growth rate of selected modes in subharmonic band (a) and fundamental band (b).

Figure 4.19 shows the envelope of the primary wave used in the controlled transition case studied in figure 4.18. It also shows the envelope of the wave packet along the centerline at a region where the primary wave in the control case reaches a maximum. The bottom figure shows results for the nonlinear packet. The top figure shows results for a linear packet scaled to the amplitude of the nonlinear packet at some position where the nonlinear packet displays linear behavior. Since, as shown previously, the primary waves are virtually unaffected by nonlinearity, the linear results shown are a representation of the linear part contained in the nonlinear packet. The results show that the amplitude of the primary wave in the controlled transition case is about 80% of the maximum amplitude in the packet. In other words it can be said that the effective amplitude of the packet in what concerns the subharmonic secondary instability is a little smaller than the maximum amplitude in the packet. The concept of effective amplitude was presented by [16] in the context of streamwise-modulated-only waves, and also used by [55] in the context of spanwise-modulate-only waves. In both cases the effective amplitude was the maximum amplitude in the packet. For modulation in both directions, the amplitude is a little lower.

[79] investigated the phase-locking of subharmonic waves and its respective primary wave in the Mach=6 wave packet. In their results, phase locking was observed only in the nonlinear regime and was used as an indication of subharmonic instability. In figure 4.16 a similar analysis is presented for the current results. Figure (a) shows the phase variation of a number of modes along the x direction. Dashed lines and solid lines correspond respectively to the primary and subharmonic waves already discussed in figure 4.15. Numerical results are shown for linear packet, nonlinear packet and controlled transition, all with perfect agreement. It shows clearly that no significant phase adjustment is caused by nonlinearity. That is expected for subharmonic instability of the Craik type where the waves that resonate already match the phase speed required for resonance. Indeed, this secondary instability is a limiting case of H-type instability as the driving wave amplitude decays.

Conclusions are further supported by the distribution of streamwise wave number of these modes along the streamwise direction, figure 4.15(b). Some irregularities are observed at the earlier and later stages, but the bulk of the distribution is also not affected by nonlinearity. Figures 4.15(c) and 4.15(d) show the actual phase speeds, with figure 4.15(d) showing that, for a large portion of the evolution, the phase speeds of the resonant modes match each other only a little better under resonance. Once more the results are consistent with subharmonic instability of a small amplitude driving wave.

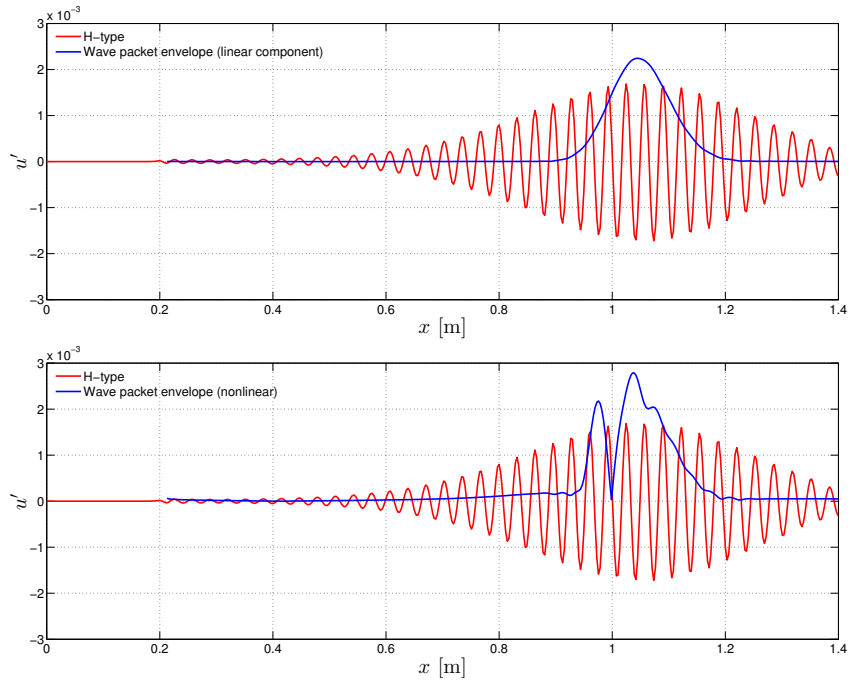


Figure 4.19: Effective amplitude for H-type breakdown.

The asymmetry of the nonlinear effect with respect to packet maximum amplitude

From the amplification curves it is clear than subharmonic modes grow nonlinearly from a position downstream near the disturbance source. However in the time signal velocity their effect is not visible due to subharmonic low levels. When subharmonic component in the packet is aligned with its correspondent fundamental mode (2D), their amplification is optimized, and deformation of the wave packet is observed in downstream, as can be seen in figure 4.20.

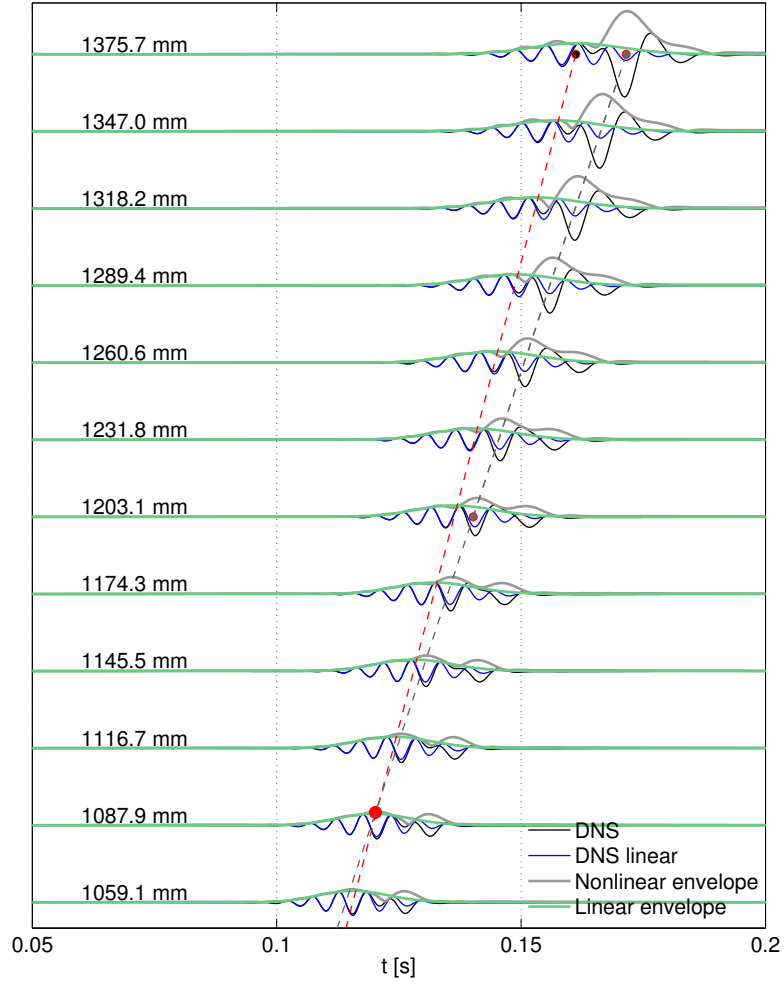


Figure 4.20: Effect of nonlinearity on wave packet format.

4.4.2 Fundamental bands

In the fundamental band it were selected two bands, indicated by yellow circles in figure 4.21. The first band, shown in the top frames, has the same frequency of the dominant 2D mode, that could amplify as K-type breakdown. The second band, shown in the bottom frames, has higher frequencies, maintaining the same spanwise wave numbers of the first band. The modes are identified by their indices (n, k) in the spectrum. These bands are interesting because [13] shows strong nonlinear amplification in these bands, also, [54] report similar amplification for lower amplitudes of the wave packet. Amplification curves reveals that nonlinear growth dominates from in positions around $x^* = 800mm$ and $x = 700mm$ for the first and the second group respectively.

On each group it was selected a mode, to verify if exists fundamental resonance condition. In figures 4.22 and 4.23 can be observed locking between 2D fundamental wave and oblique mode, for both bands. In the second band, locking occurs first than in the first one, because the 2D wave reach threshold amplitude before, because linear amplification is triggered early for higher frequencies (see figure 4.7).

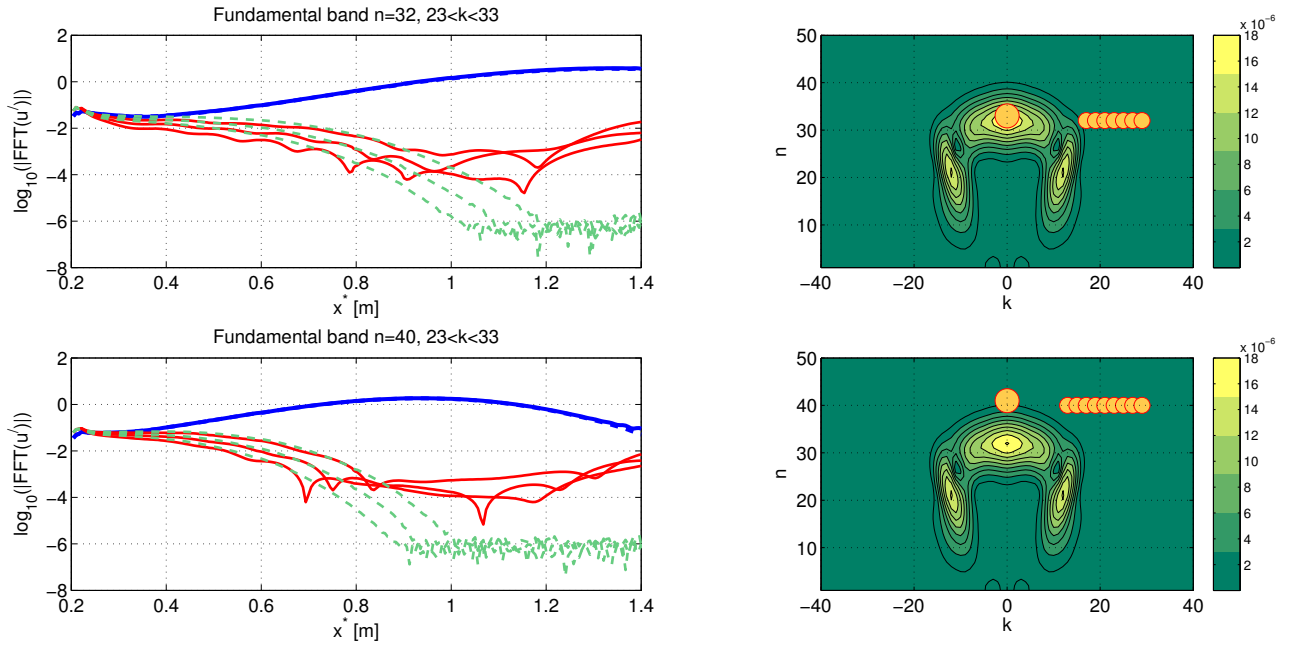


Figure 4.21: Amplification curves for fundamental bands of linear (green lines), nonlinear (red lines) and fundamental (blue lines) modes.

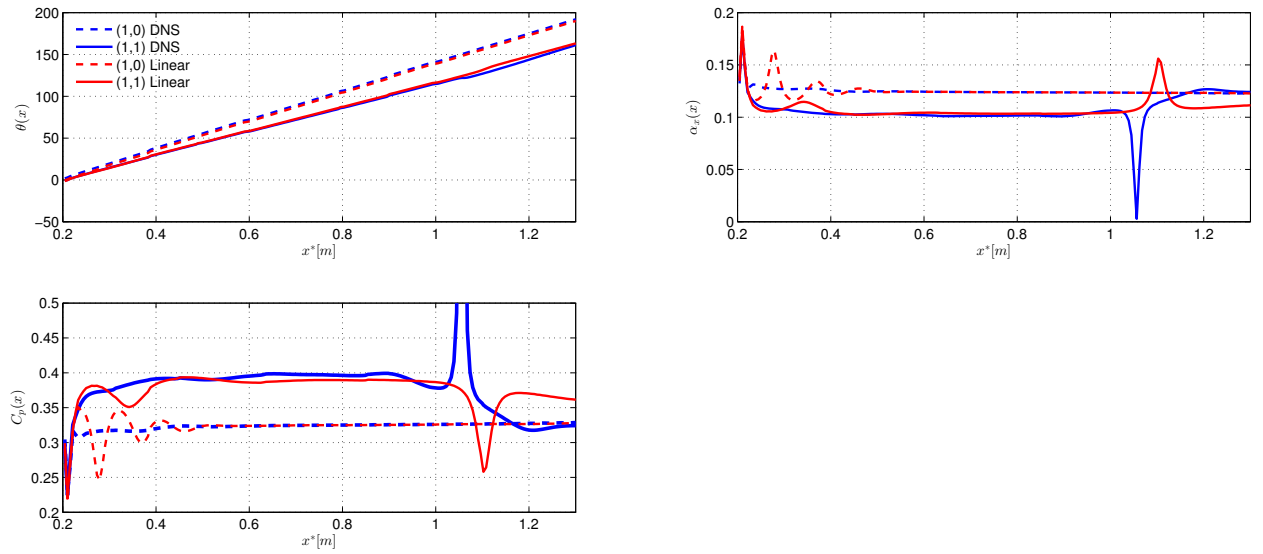


Figure 4.22: Mode of the first band, $n = 32, k = 25$, (a) Phase, (b) streamwise wave number, (c) locking in phase velocity for fundamental resonance.

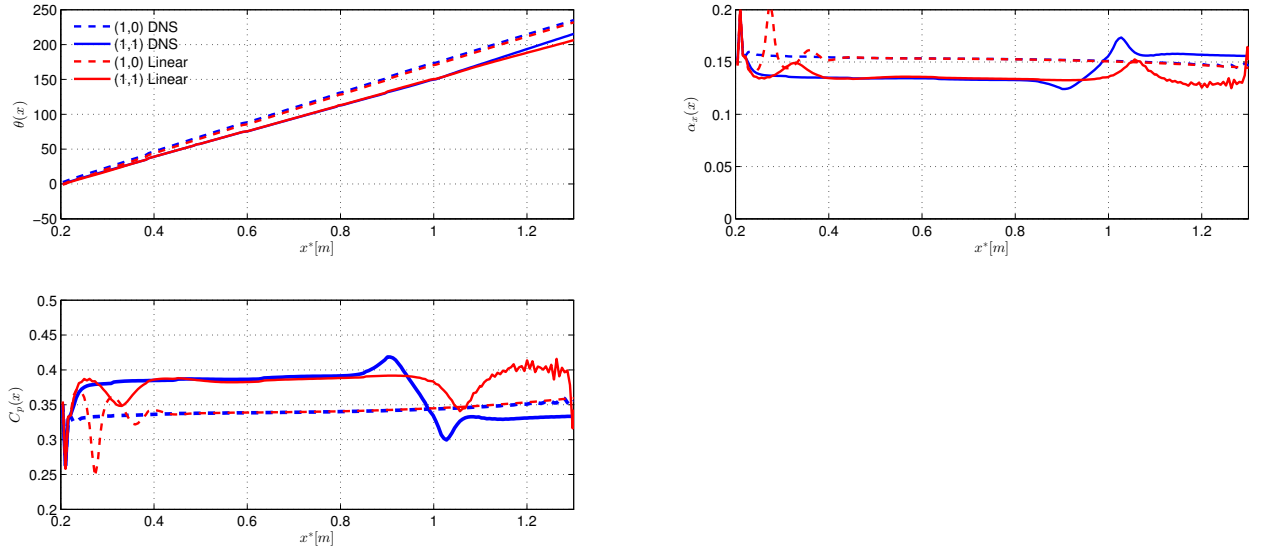


Figure 4.23: Mode of the second band 2 , $n = 40$, $k = 25$, (a) Phase, (b) streamwise wave number, (c) locking in phase velocity for fundamental resonance.

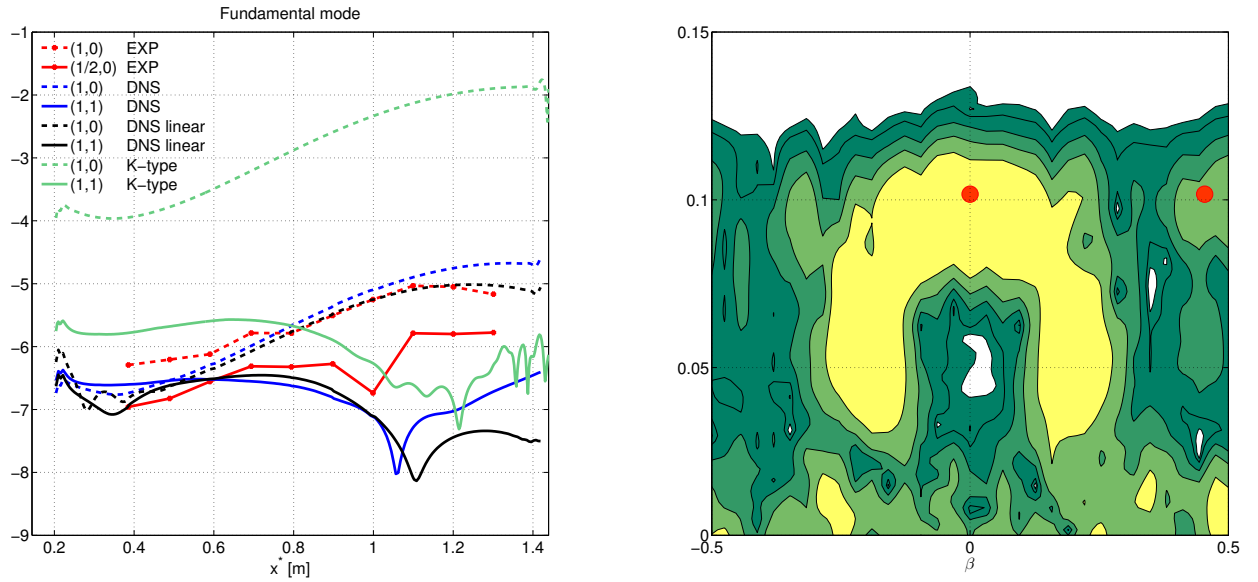


Figure 4.24: Amplification curves of selected modes in the fundamental band.

Effective amplitude for fundamental resonance

To reproduce nonlinear growth rates for modes oblique modes (1,1) by controlled transition of K-type breakdown, the threshold amplitude of the 2D wave must be higher than the wave packet amplitude. In the experiment and simulations this kind of instability rises in the last measurement points with higher growth rates than H-type resonance.

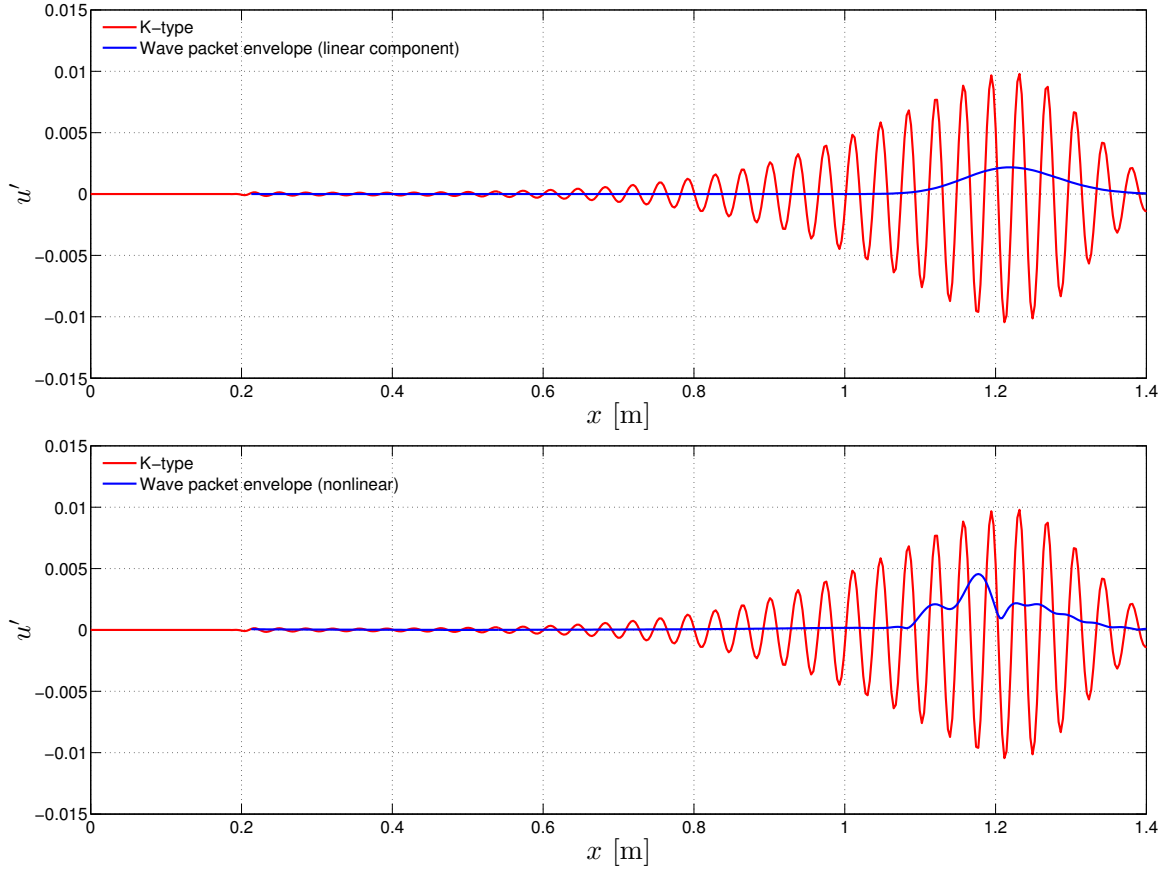


Figure 4.25: Effective amplitude for K-type breakdown.

4.5 Effective experimental conditions

In previous sections was shown that main difference between DNS and experimental results was in the modes associated with K-type breakdown. Nonlinear growth rates for low frequency modes and fundamental ones, calculated from DNS are in accordance with experimental growth rates, however, these modes have lower levels in DNS than observed experimentally. To attempt identify the cause of the levels mismatch in the experiment, some effective experimental imperfections were investigated.

4.5.1 Pressure gradient

The experimental pressure coefficient C_p shown in figure 4.26, was included into pressure distribution at the outflow boundary as $p_{yf} = p_\infty + C_p$. Amplification curves were calculated for a wave packet with the experimental pressure gradient, a subharmonic (figure 4.27(a)) and a fundamental mode (figure 4.27(b)). From the amplitude curves can be concluded that experimental pressure gradient has no effect on fundamentals modes level, because difference in levels of the mode (1,1) between DNS result and experiment remains almost equal as in previous case.

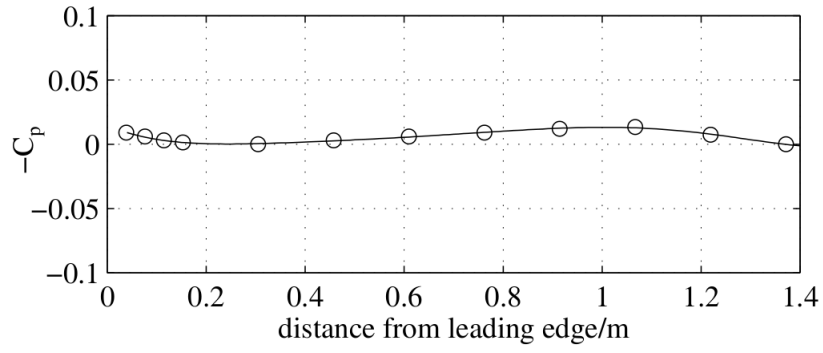


Figure 4.26: Experimental pressure gradient curve. (Reproduced from [54].)

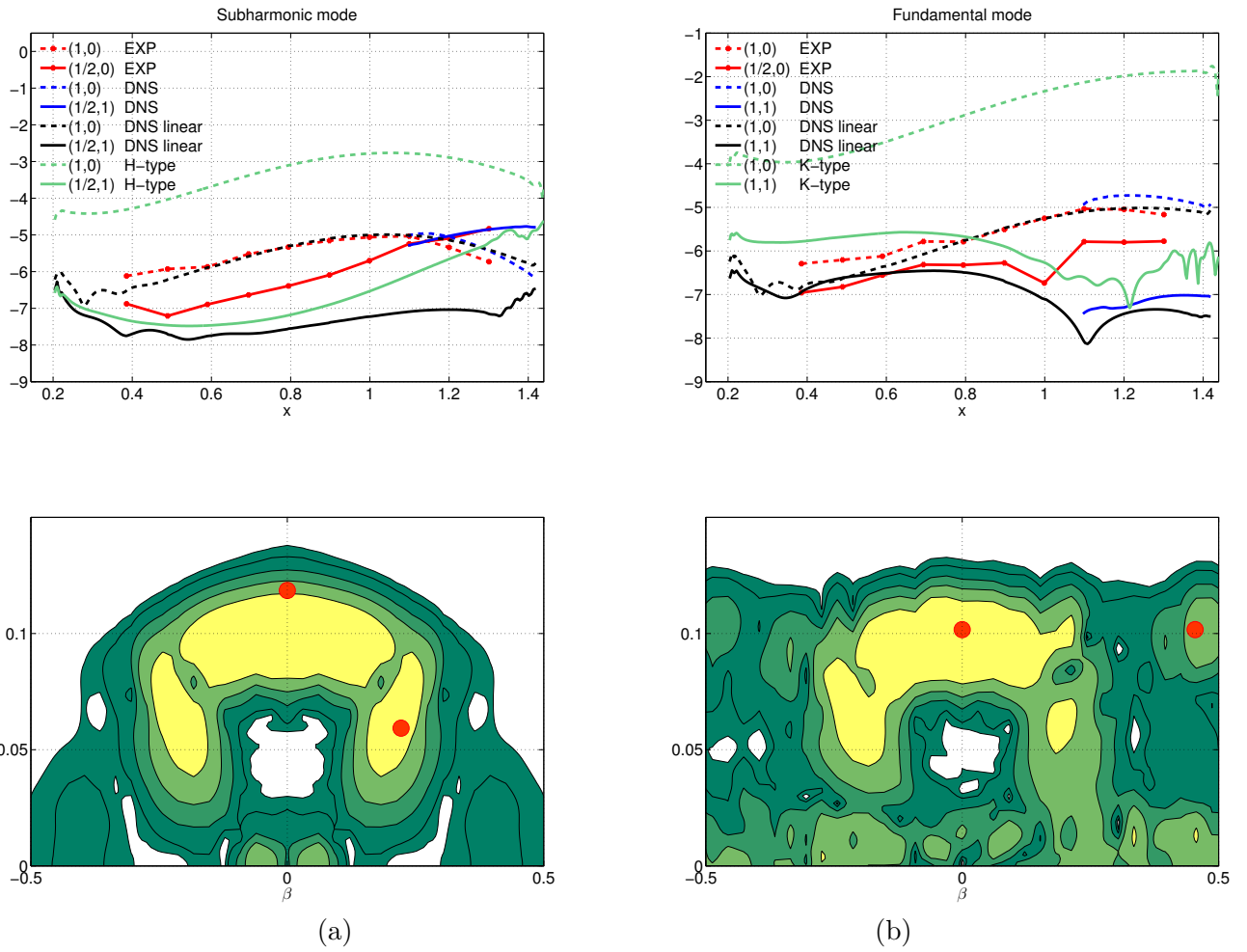


Figure 4.27: Amplification curves and spectrum at $x^* = 1200mm$, for a wave packet with the experimental pressure gradient, (a) subharmonic and (b) fundamental mode.

4.5.2 Amplitude calibration

The experiment displayed some asymmetries in relation to the center of the plate, not present in DNS simulations due to idealization of the problem. Also [11] shows that spectra of the ensemble-averaged is *different* from the ensemble average of the individual spectra. It is not clear DNS result to which can be associated. For the present analysis results are compared directly, but in future works this detail deserve more attention. To evaluate the effect of these factors in the fundamental mode amplification, a modal calibration in Fourier space was done, in a linear region without affect nonlinear evolution. This strategy was used successfully in [51] to compare numerical and experimental data. It is based on weighting each mode, to have the same amplitude of the experimental spectrum in a linear position.

Calibration was done in the linear position at $x^* = 600mm$. Also the experimental pressure gradient was considered. In the spectrum at position $x^* = 1300mm$, from calibrated spectrum (figure 4.28) can be observed that fundamental modes remains underestimated. Moreover the subharmonic bands present a higher deviation from experimental, than obtained for the simulation with plane spectra.

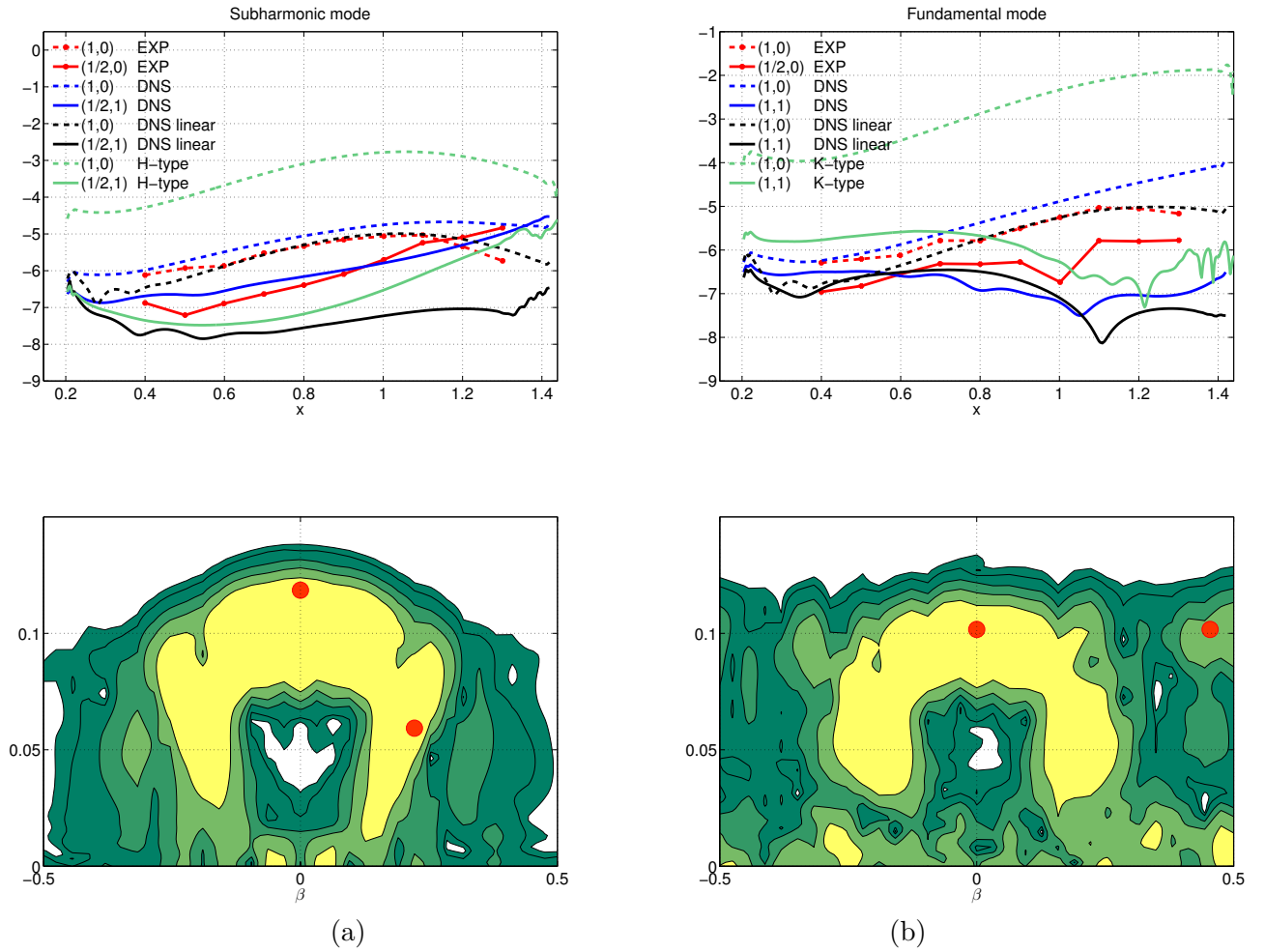


Figure 4.28: Amplification curves and spectrum at $x^* = 1200mm$, for wave packet with experimental pressure gradient and spectrum calibration at position $x = 600mm$. (a) Subharmonic and (b) fundamental mode.

4.5.3 Amplitude effect

Experimental [59] and numerical works [81] relate high levels of fundamental modes with disturbance amplitude. To investigate the amplitude effect, a wave packet generated with an amplitude higher %20 than in previous case was simulated. In figure 4.29 it can be seen that the resulting spectra have levels in fundamental band that are similar to the experimental ones, however, low frequency modes present higher amplification. Also, subharmonic mode is overestimated.

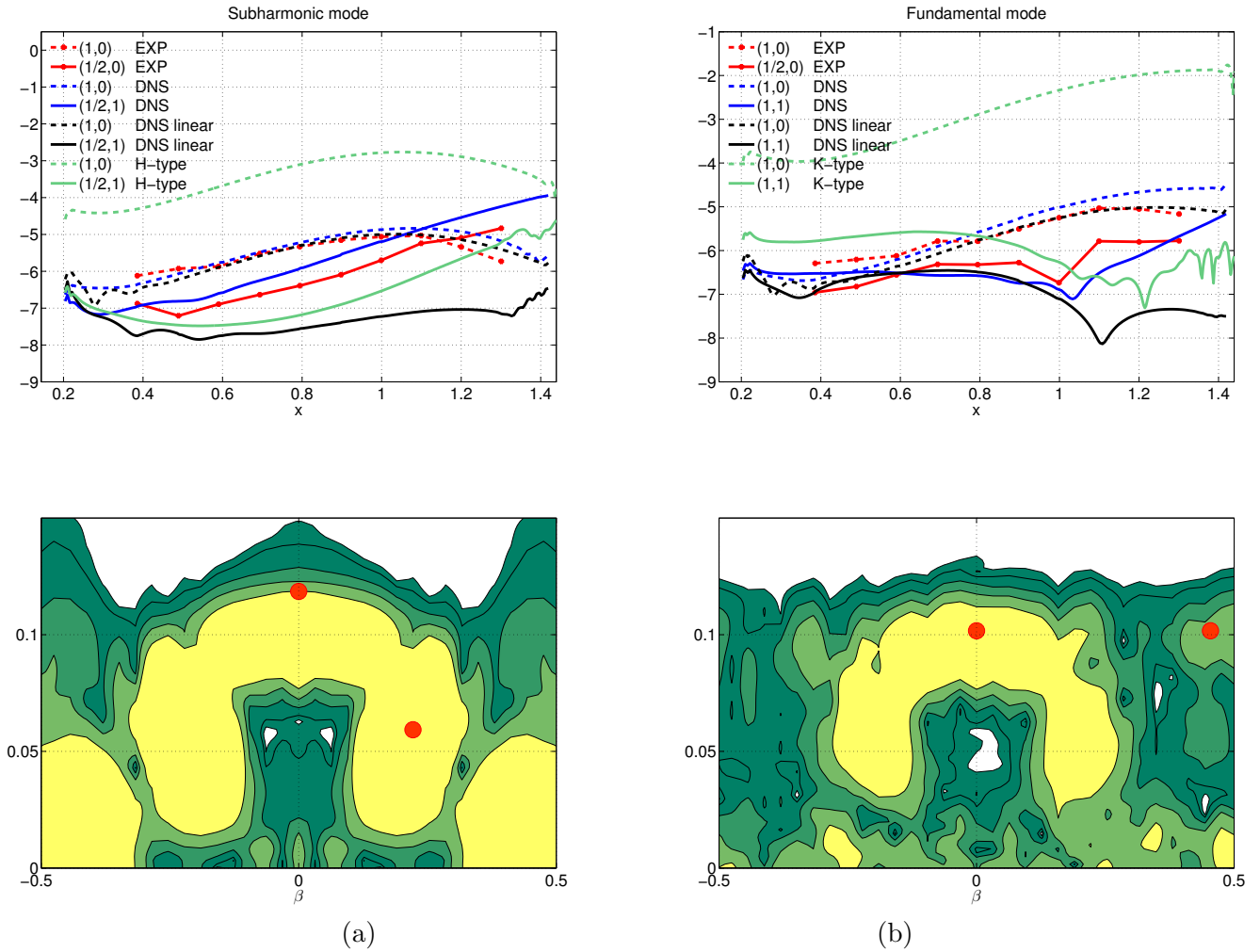


Figure 4.29: Amplification curves and spectrum for a wave packet with disturbance amplitude increased 20%. (a) subharmonic and (b) fundamental mode.

4.6 Seed

To investigate the origin of subharmonic modes they were removed from the perturbation spectrum as can be seen in figure 4.30, as was done by experimentally [54].

In the resulting spectra (figure 4.32), subharmonic modes develop almost equal than in the previous case (see figures 4.18, 4.31), with the complete band at the perturbation. Then, subharmonic modes are generated by nonlinear interaction, however the responsible mechanism is not known. Preliminary observations suggest that it also occurs for modes in the fundamental band, that are amplified nonlinearly, but must be confirmed by complete mode removal from the perturbation spectra of these modes.

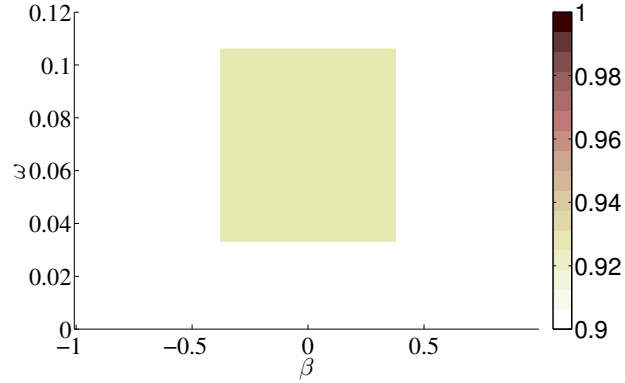


Figure 4.30: Spectrum of the perturbation with subharmonic band removed.

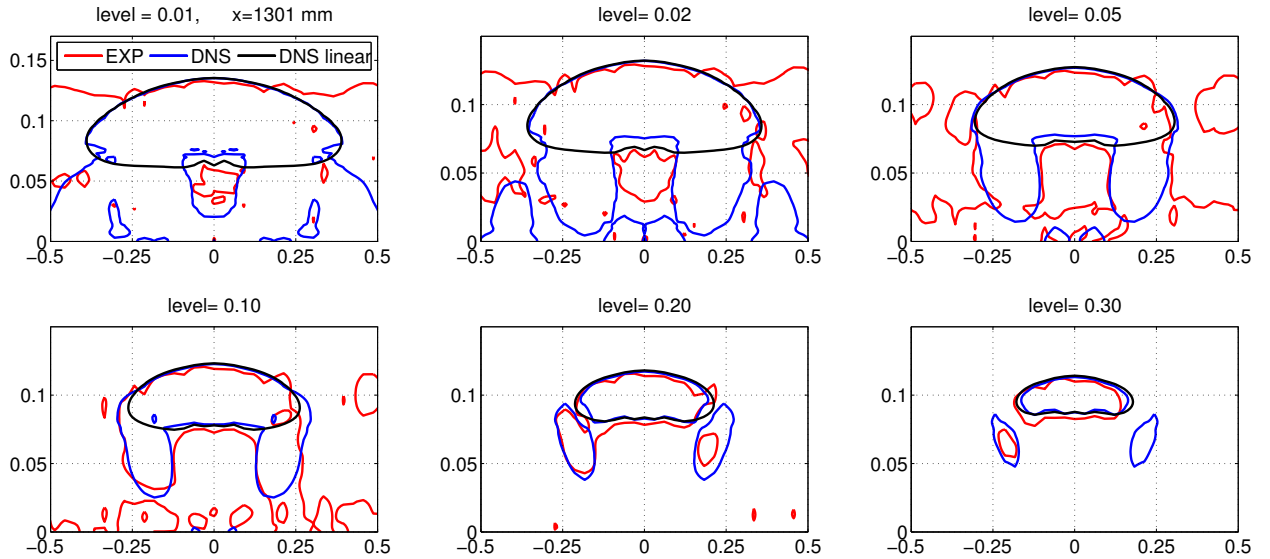


Figure 4.31: Comparison of spectrum levels at $x=1300\text{mm}$, to investigate subharmonic seeding.

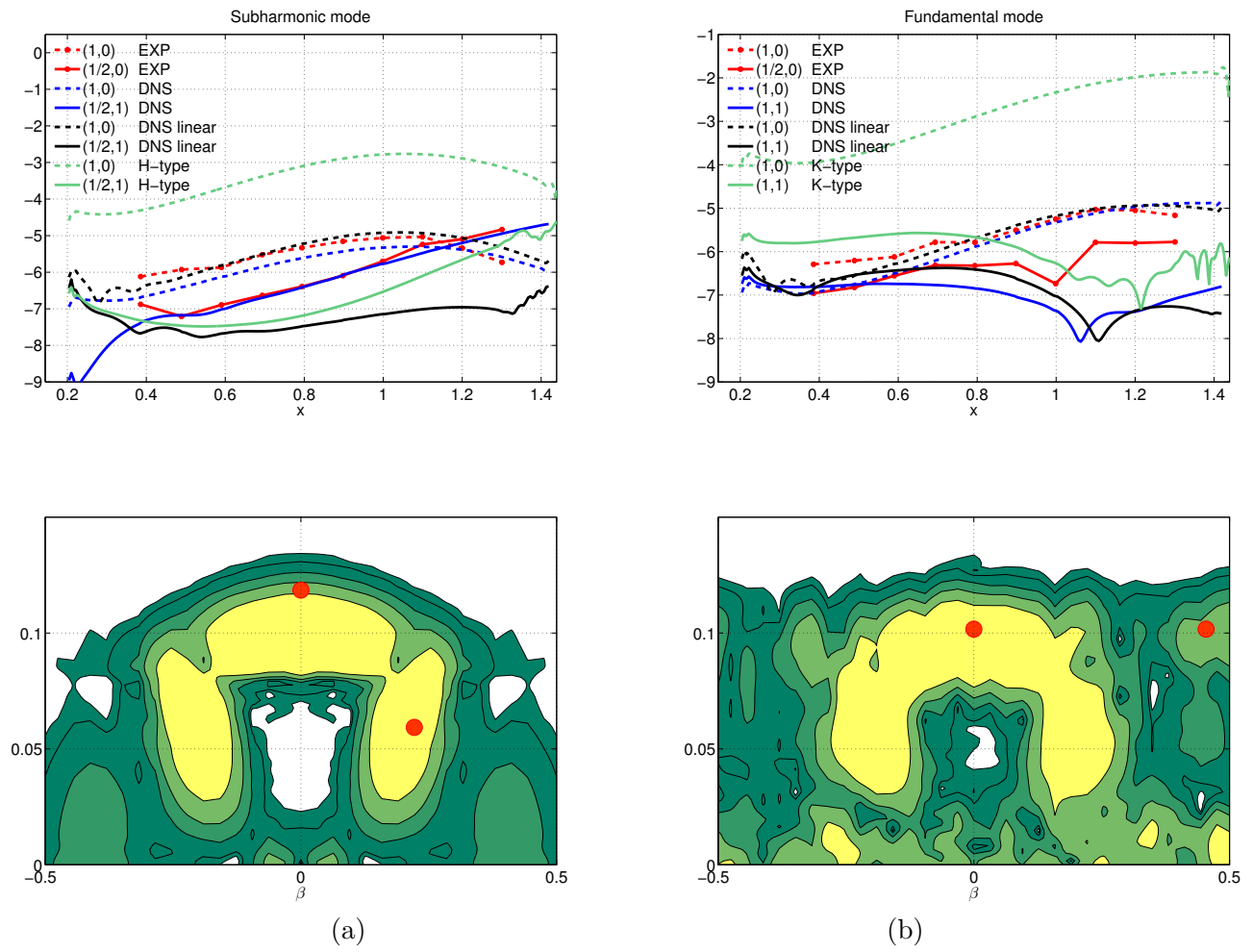


Figure 4.32: Amplification curves and spectrum of the wave packet generated by removing subharmonic band in the perturbation spectra.

Chapter 5

Wave packet in subsonic boundary layer

Some observations at Mach 0.5, considering white noise [58], nonlinear growth [91], transition on an airfoil [44] and secondary instability mechanisms [17] suggest that up to Mach 0.5 there are no remarkable differences on the initial nonlinear stages of transition on compressible boundary layer. Then for $Mach > 0.5$, compressibility effects rises on the transition process.

This section is organized as follows. Initially the numerical set-up is defined. Next, the evolution of linear and nonlinear wave packet is investigated by DNS simulation, considering boundary layer on a flat plate at Mach 0.7 and 0.9. Main differences with wave packet on incompressible boundary layer are established and early nonlinear stage is investigated from the spectral evolution. Finally, to consider a closer scenario to natural transition, results for interaction at Mach 0.9 of two wave packets are presented, in physical and Fourier spaces.

5.1 Numerical set-up

To reduce computational time needed to perform the simulations, it was considered as reference case the experimental parameters of [14], for incompressible boundary layer. This experiment introduces relative high level of disturbances amplitude which induces develop of transition in a smaller region of the boundary layer in streamwise. The disturbance was the same considered for the incompressible case, covering the same bands and controlling the perturbation spectrum as shown in section 4.2. The perturbation was located at the position $x_0 = 200$. From the experimental parameters defined in the table 4.1 the computational domain is:

$$\begin{aligned} 0 &\leq x \leq 1200 \\ 0 &\leq y \leq 20 \approx 3.5 \times \delta_{99}(x = 1200) \\ -\frac{2\pi}{\beta_0} &\leq z < \frac{2\pi}{\beta_0} \end{aligned}$$

It was employed the same grid resolution as in the incompressible boundary layer, the resultant number of grid points in each direction is $nx = 601, ny = 51, nz = 161$. Some tests, not shown here, reveals grid independence for this computational arrangement. The flow parameters for DNS simulation are $Re = 1035$, $Pr = 0.71$, and the considered Mach numbers, $M_\infty = 0.7$ and $M_\infty = 0.9$. In all simulations isothermal wall was considered.

5.2 Wave packet in a boundary layer at Mach 0.7

At Mach 0.7 three wave packets were simulated, a low amplitude packet (linear) to be used as reference case and two nonlinear packets with amplitudes $a_1 = 3.5 * 10^{-5}$ and $a_2 = 2.5 * 10^{-5}$. The perturbation amplitude was chosen to guarantee a linear amplification during a short distance from the perturbation location.

5.2.1 Linear wave packet

The N-factor allows to identify the most amplified mode at a fixed spanwise wave number. Empirically have been established that transition occurs at $N \sim 9$, (see [88]). The N-factor is defined as:

$$N = \ln \left\{ \frac{A(x)}{A_{ref}} \right\} \quad (5.1)$$

As illustration, for Mach 0.7, the resultant N-factor curves are shown in figure 5.1. The most unstable mode has the highest N, it is indicated by the red line. From current DNS simulations for linear wave packets at several Mach numbers, it was found that the most amplified mode 2D decays with Mach number, as can be observed in figure 5.2. These modes were found from N-factor curves. As a consequence, the modes influenced by the nonlinear amplification in downstream may change by Mach number.

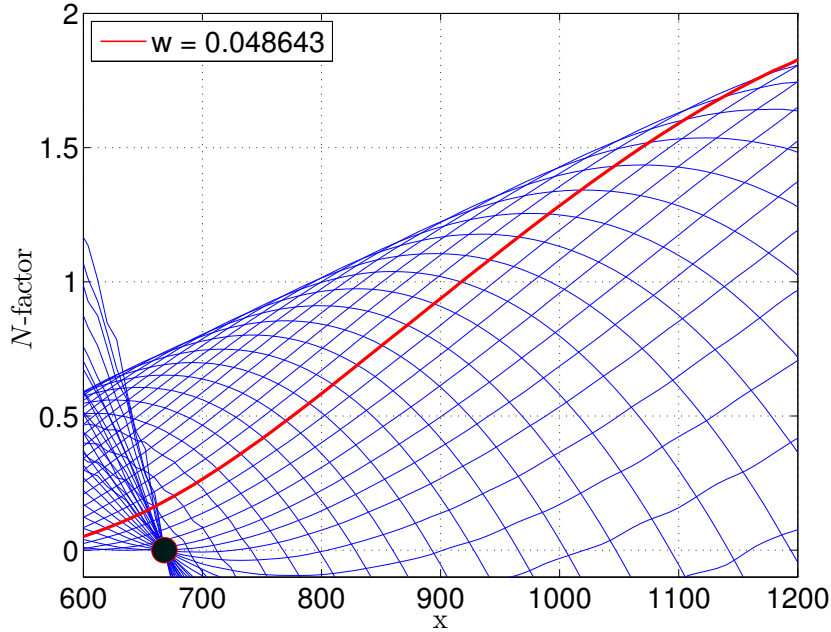


Figure 5.1: N-factor curves for Mach 0.7. Red line indicates the mode 2D most amplified., in this case corresponds to the mode $\omega = 0.048$.

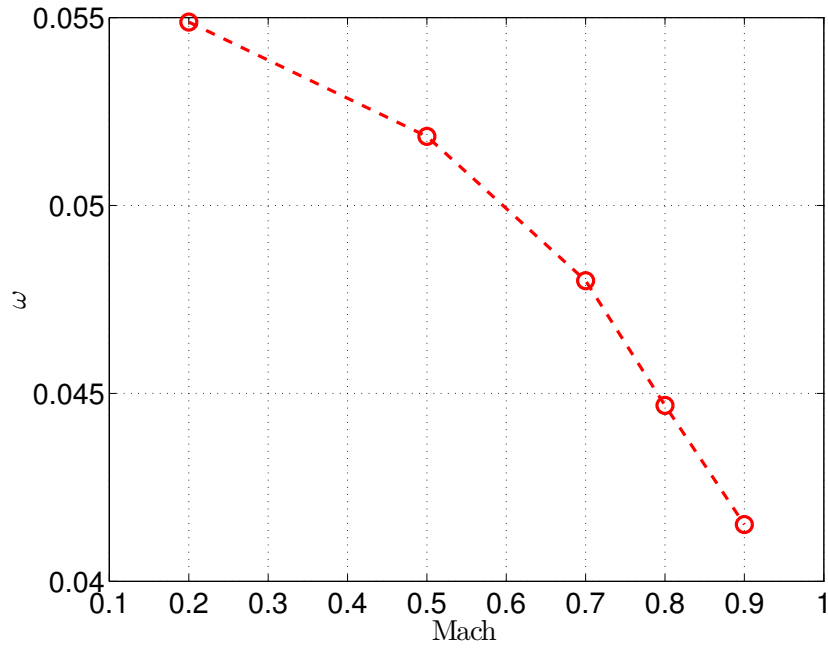


Figure 5.2: Variation of the frequency of most amplified 2D mode with Mach number, calculated from the N-factor curves.

5.2.2 Nonlinear wave packet

For the amplitude a_1 , the linear and nonlinear wave packet are compared at advanced downstream position in figure 5.3. The linear wave packet has regular and smooth distribution of amplitude with no strong modulation in spanwise. The nonlinear packet presents well defined three-dimensional structures, higher amplitudes are concentrated at the center of the packet. In figure 5.4 is shown the spectral evolution for linear and nonlinear wave packet in global nondimensional variables. The linear amplification concentrates energy in the 2D modes in downstream, and as occurs in the incompressible boundary layer, the frequency of the dominant mode decays when local Re_x increases.

In the nonlinear wave packet the spectrum gains energy in downstream positions, mainly in the subharmonic band and low frequency modes, a similar behavior was observed in the incompressible case (figure 4.29). For a more quantitative analysis it was selected the spectrum at the nonlinear position $x = 972$. Figure 5.5 allows to separate clearly the linear from nonlinear bands, by comparison of spectrum levels. From this spectrum it was chosen a mode representative on each band, to compare its amplification curve with the linear wave packet (figure 5.6).

Each mode is identified in the figure by the color and the indexes (n, k) in the legend of the figure. Near the perturbation location, at $x = 200$, the amplification curves are as the linear ones, because the amplitude disturbance was chosen to satisfy this condition. In downstream positions all selected modes grows with higher growth rates than linear ones. For the considered computational domain, low frequency modes and subharmonic band, denoted by the red circle, are the nonlinear dominant modes.

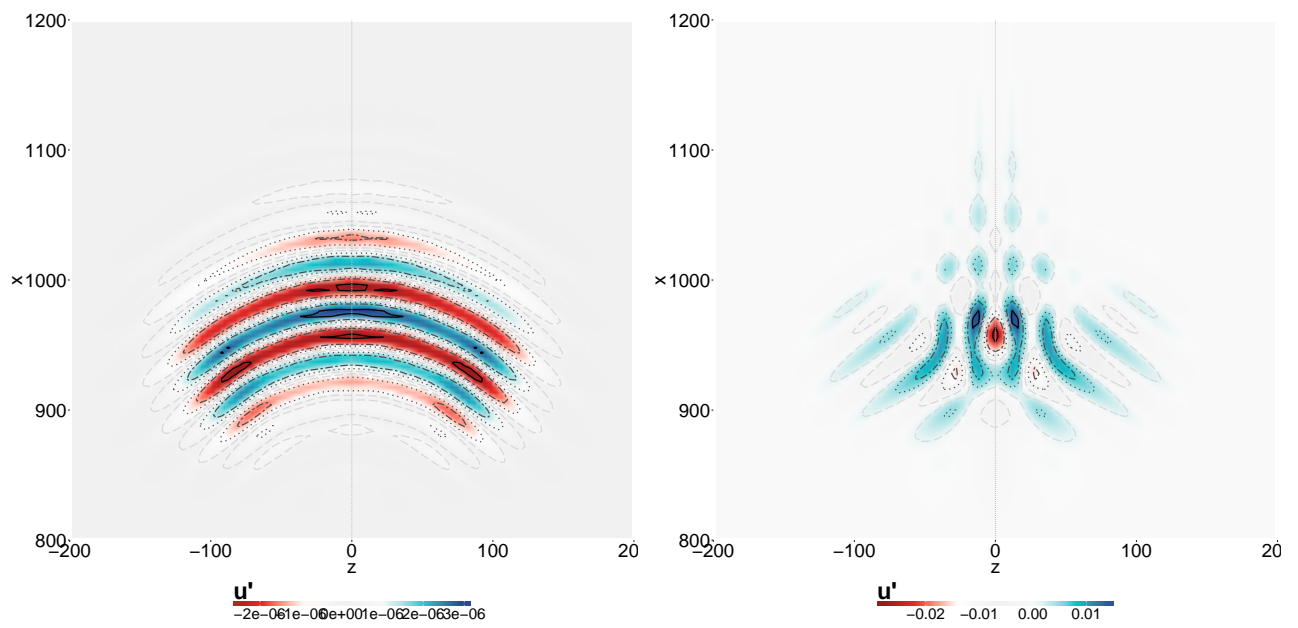


Figure 5.3: Nonlinear wave packet at Mach 0.7, in $y = 0.6\delta^*$. Contour levels at 90% (—) , 50% (-.-), 30% (...) and 10% (- -) of the amplitude peaks in the packet.

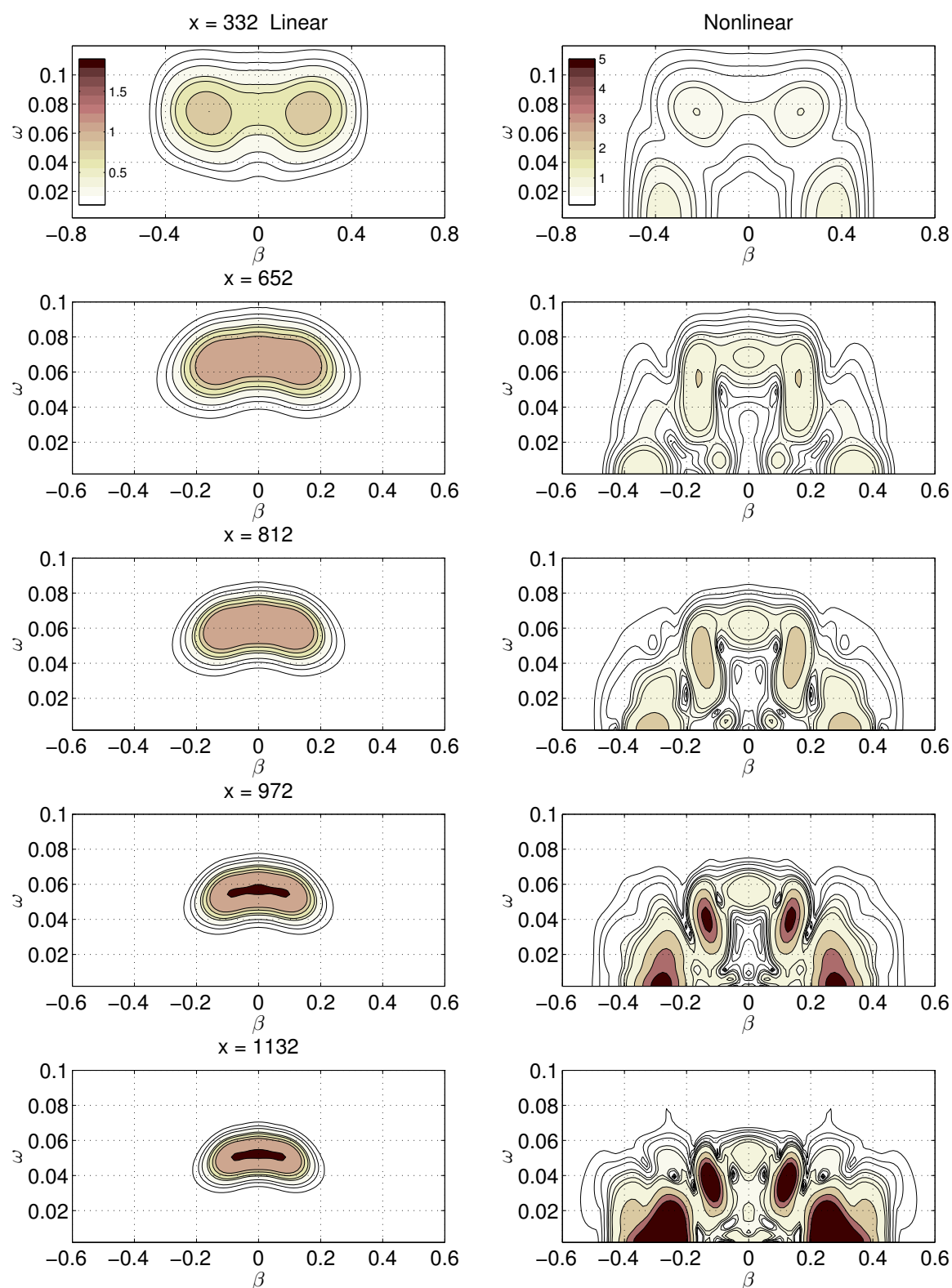


Figure 5.4: Spectral evolution at Mach 0.7, for linear and nonlinear wave packet.

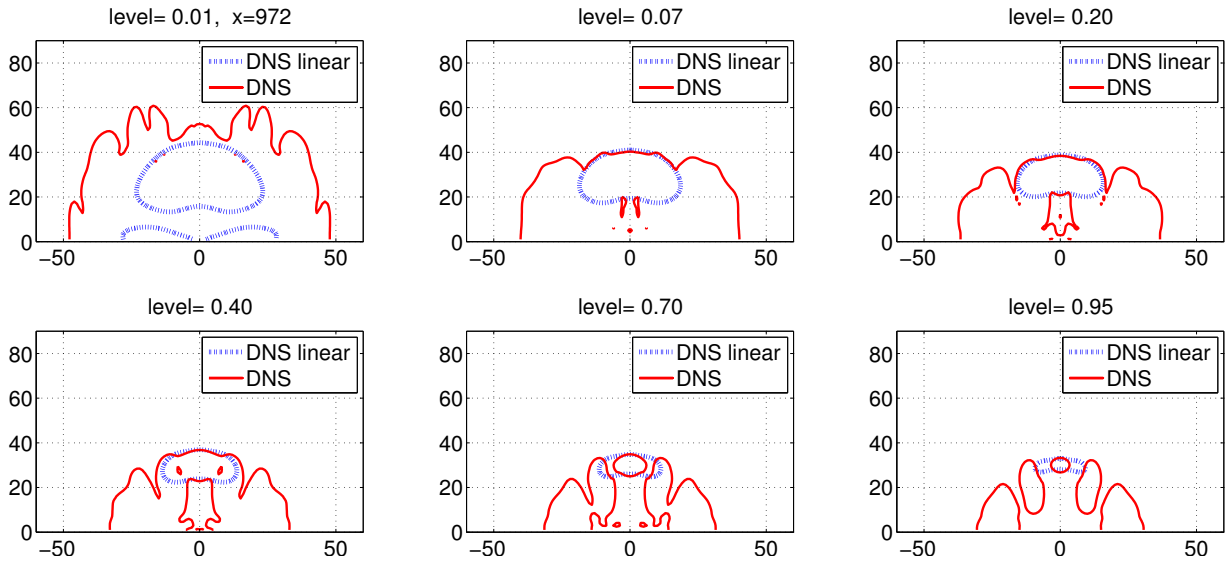


Figure 5.5: Spectrum levels for Mach 0.7 at $x=972$.

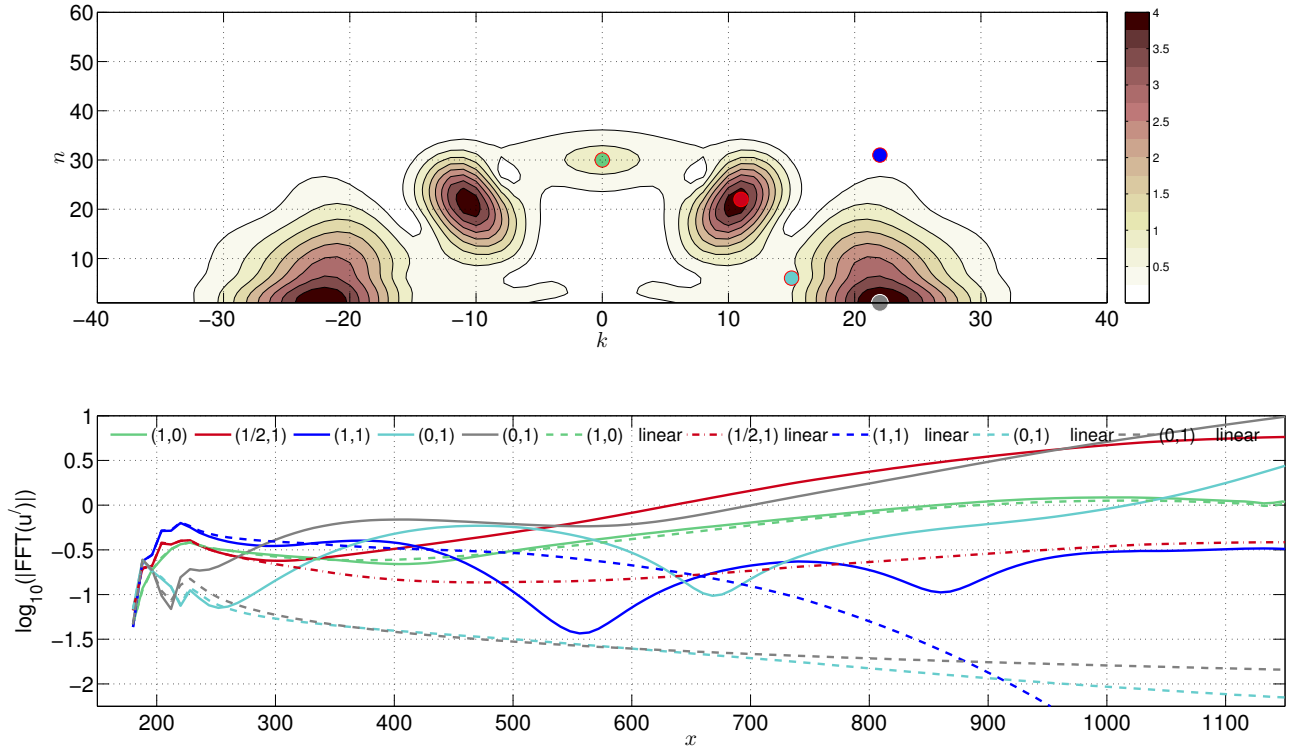


Figure 5.6: Amplification curves for Mach 0.7 for selected modes in the spectrum at the position $x = 972$. All bands shows strong nonlinear amplification.

5.2.3 Amplitude effect

To test effect of disturbance amplitude it was simulated a packet with a lower amplitude than in previous case a_2 . It was not considered an higher amplitude because it would be nonlinear from the source. Now, spectrum evolution (figure 5.7) and amplification curves (figure 5.8) reveal that in contrast to the case with higher amplitude, only two bands have nonlinear amplification. The subharmonic and low frequency modes, that remain growing in the considered domain.

Signals of for both nonlinear wave packets at the centerline are shown in figure 5.9. The packet with higher amplitude have strong amplification and deformation in relation to the linear. Amplitude has an important role in the nonlinear mechanisms that are triggered in the transition region.

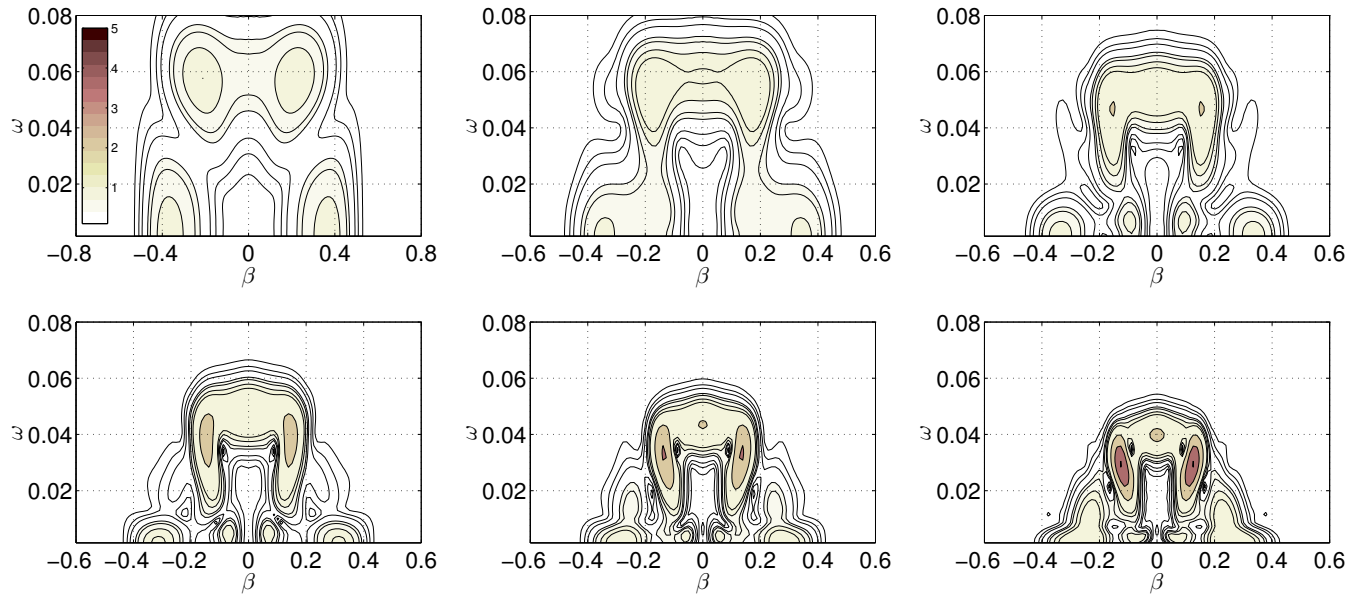


Figure 5.7: Spectral evolution for Mach 0.7, for nonlinear wave packet with disturbance amplitude $a_2 = 2.5 * 10^{-5}$.

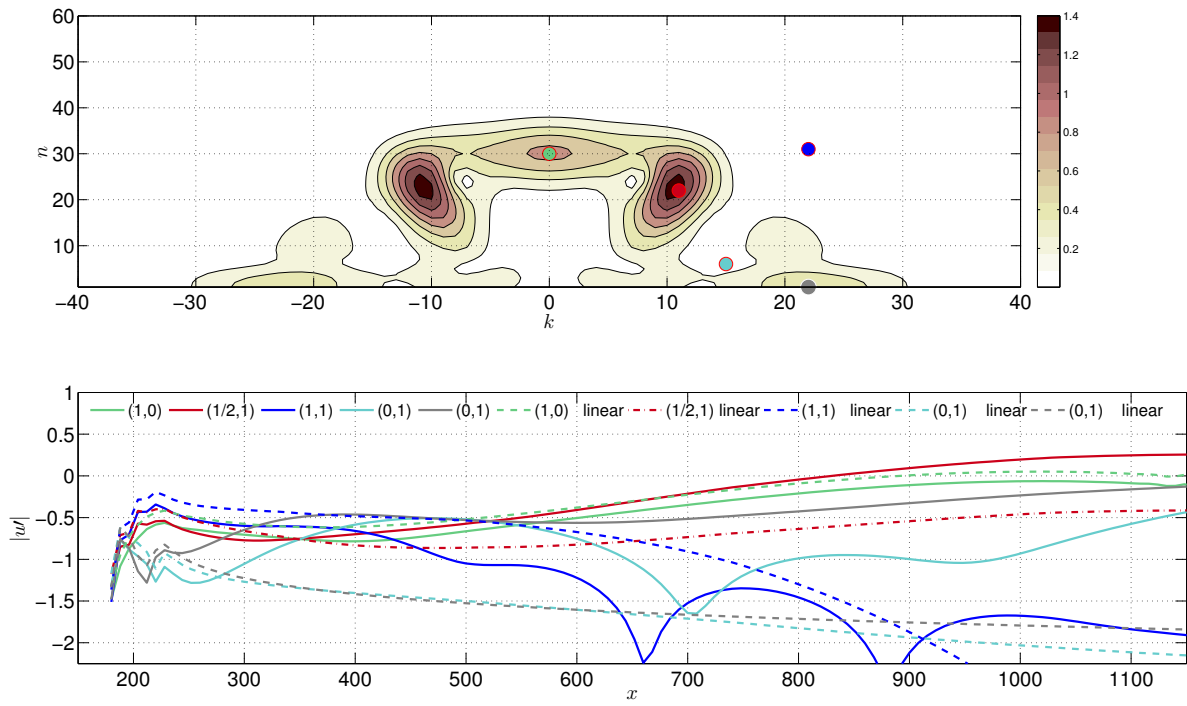


Figure 5.8: Amplification curves for disturbance $a_2 = 2.5 \times 10^{-5}$.

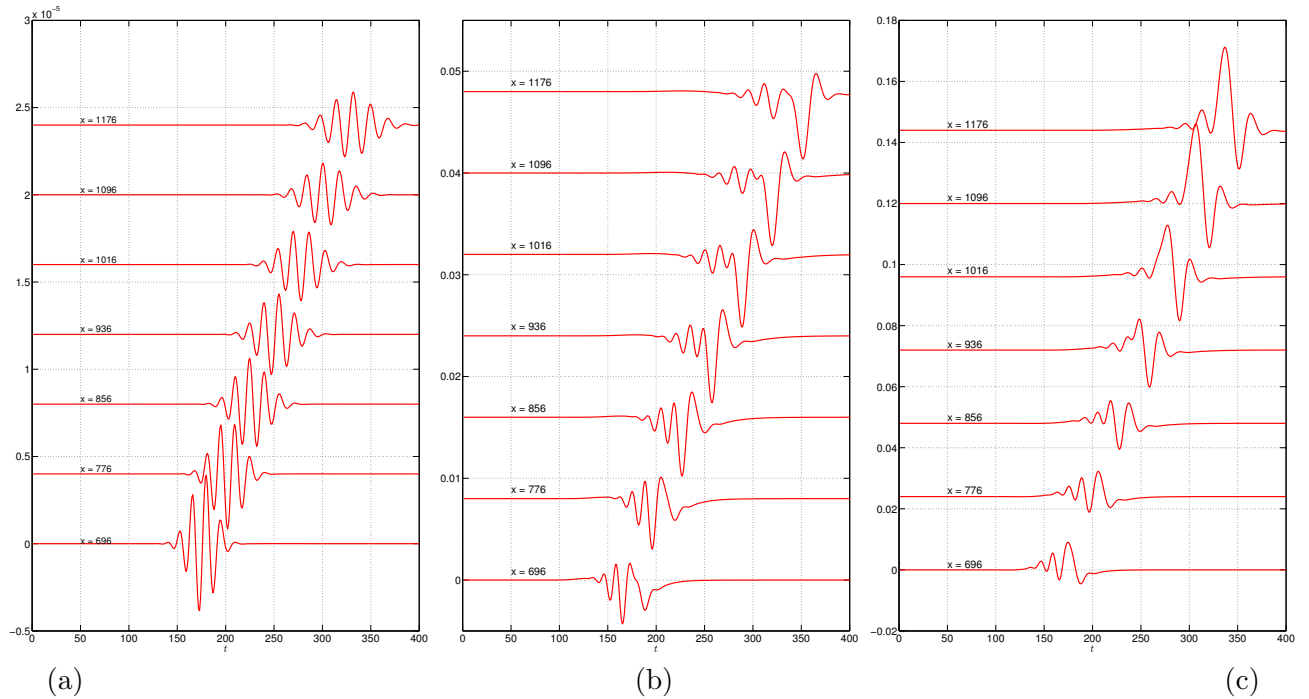


Figure 5.9: u component of velocity at the centerline. Amplitude effect on the nonlinear wave packet evolution at Mach 0.7, (a) linear wave packet, (b) $a_2 = 2.5 \times 10^{-5}$ and (c) $a_1 = 3.5 \times 10^{-5}$

5.2.4 Phase locking

To verify if subharmonic band has a similar behavior as observed in the incompressible boundary layer, explained in section 4.4.1, it were selected two modes from the spectrum at the position $x = 972$, as shown in figure 5.10. The amplification curves for the selected mode in figure 5.10(a) reveals a strong deviation from linear growth rate at the position $x \sim 280$, that remains decaying. The oblique mode $(1/2, 1)$ is amplified nonlinearly up to position $x \sim 800$, here it recovers the linear growth rate. Changes in the growth rates for the oblique mode are driven by the threshold amplitude of the 2D wave, as indicated by dashed lines. The mode shown in figure 5.10(b) also presents nonlinear amplification, but not recovers the linear growth rate when the correspondent fundamental wave reach the threshold amplitude, even it remains growing. This fact suggest the presence of detuned amplification mechanism.

In the fundamental band the same condition was investigated by a pair of modes (figure 5.11) to verify the presence of K-type mechanism. Threshold amplitudes of the driving 2D wave shows that amplification not corresponds with this mode. Amplification could be subharmonic or detuned type.

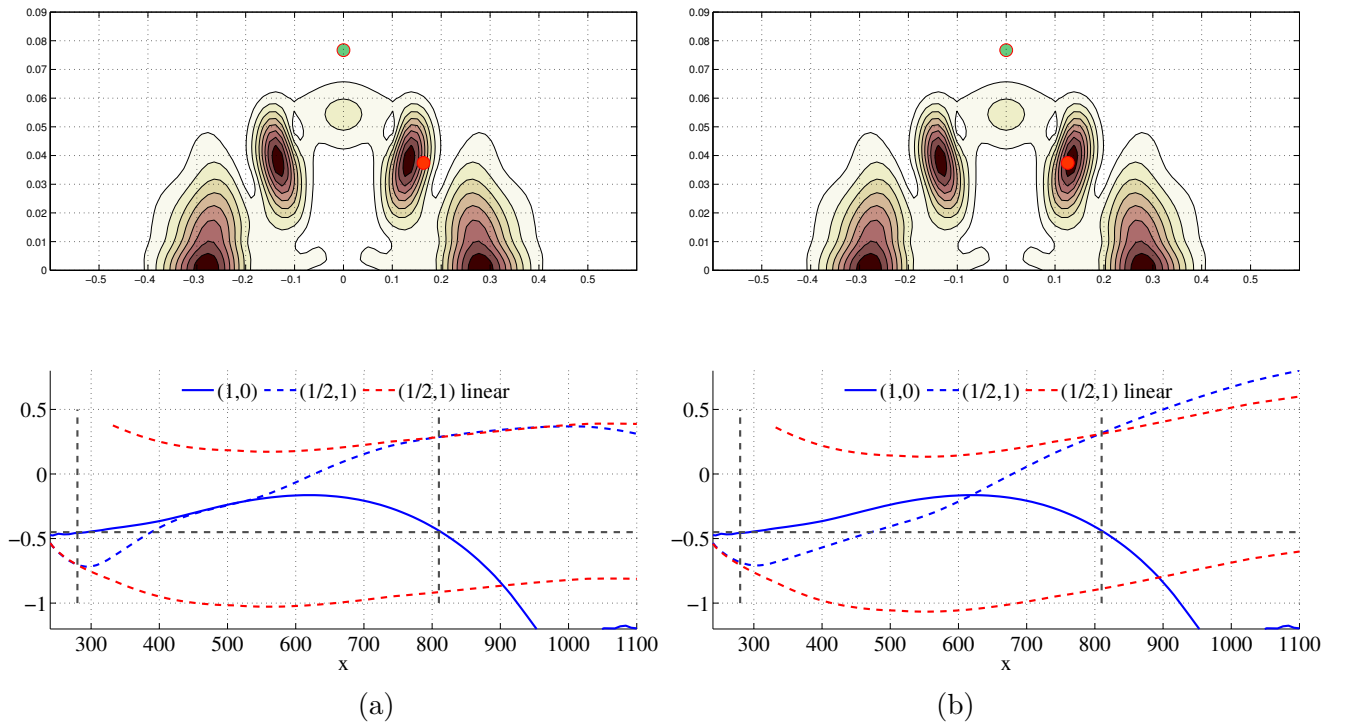


Figure 5.10: Spectrum at the position $x = 972$, for the wave packet generated with amplitude $a_1 = 3.5 \times 10^{-5}$. (a) Mode amplified by subharmonic resonance (b) non identified resonance, could be a detuned resonance.

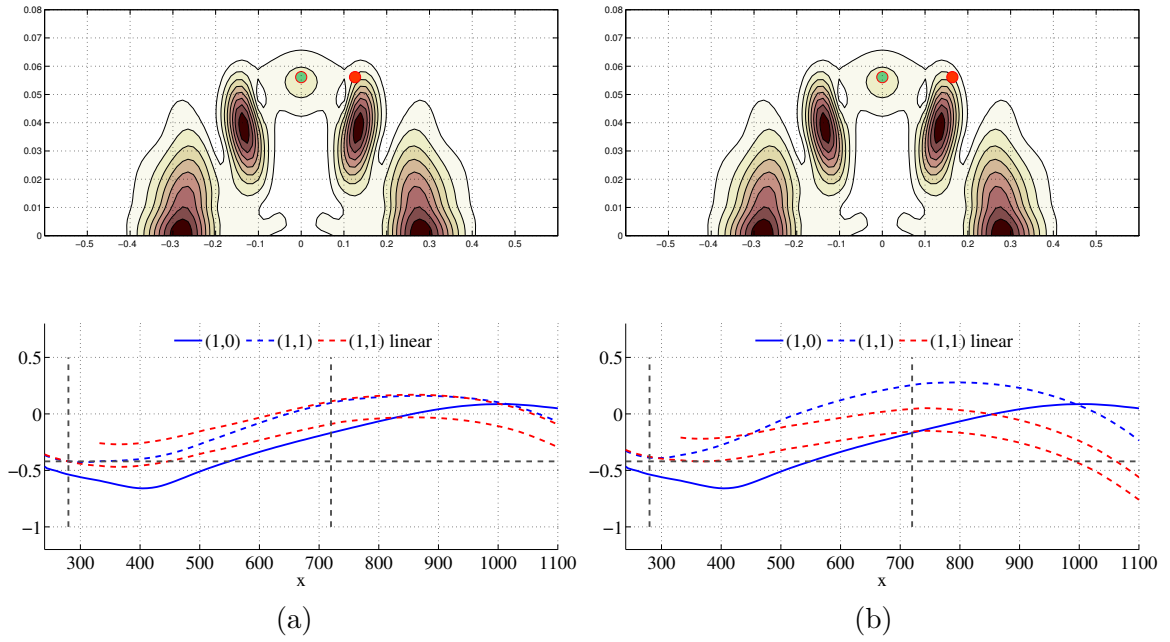


Figure 5.11: (a) Fundamental resonance (b) Non identified resonance. In subharmonic band, only some modes are amplified with subharmonic bands, also is observed nonlinear amplification. $a_2 = 3.5 * 10^{-5}$.

5.3 Wave packet in a boundary layer at Mach 0.9

As in the previous case, a linear and nonlinear wave packet were simulated, with isothermal wall, $T_{wall} = 1$, at Mach 0.9. This Mach number is interesting because is typical on passenger aircraft at cruise.

5.3.1 Linear wave packet

From DNS simulations, it was found that at Mach 0.9, the linear growth rates are around 10 times lower than growth rates for incompressible boundary layer, then it is expected that the boundary layer is more stable, and present a longer transition region. Comparison at the centerline (figure 5.12) for linear wave packet at Mach 0.2 and Mach 0.9 shows that while on the incompressible boundary layer the wave packet amplifies, in the compressible case the packet decays.

In the physical space (figure 5.13), the wave packet have low modulation in spanwise, but more intense than in the incompressible case as can be observed in figure 5.16. In the linear evolution (figure 5.13) energy is distributed uniformly in the packet.

The spectral evolution of the linear wave packet in global nondimensional variables (figure 5.14), reveals that in contrast with all the previous cases, the most linear unstable modes are oblique, centered around the mode $\omega = 0.41$ and $\beta = 0.1$, which generates modulation of the wave packet in spanwise direction.

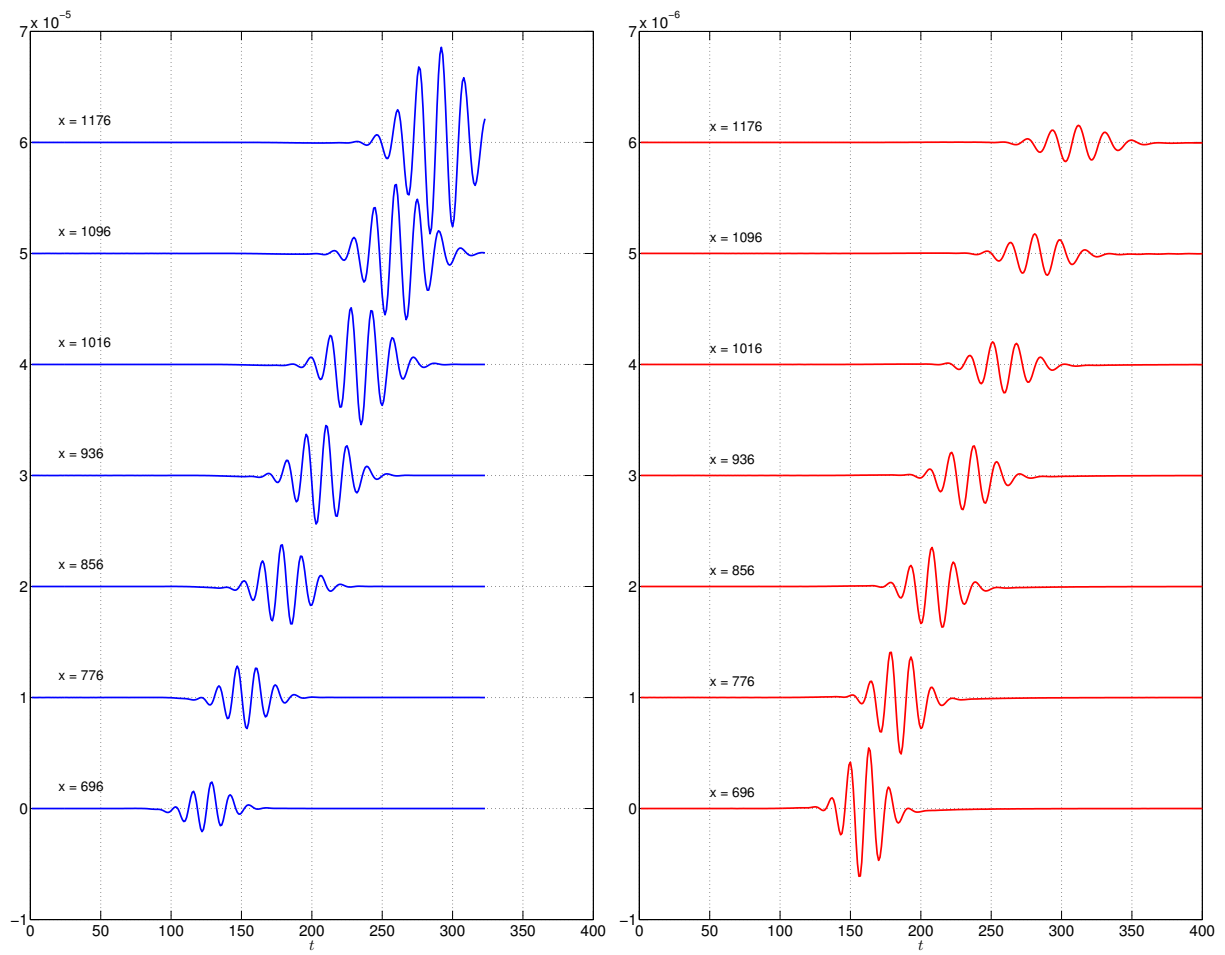


Figure 5.12: Comparison at centerline of linear wave packet for (a) Mach 0.2 and (b) Mach 0.9.

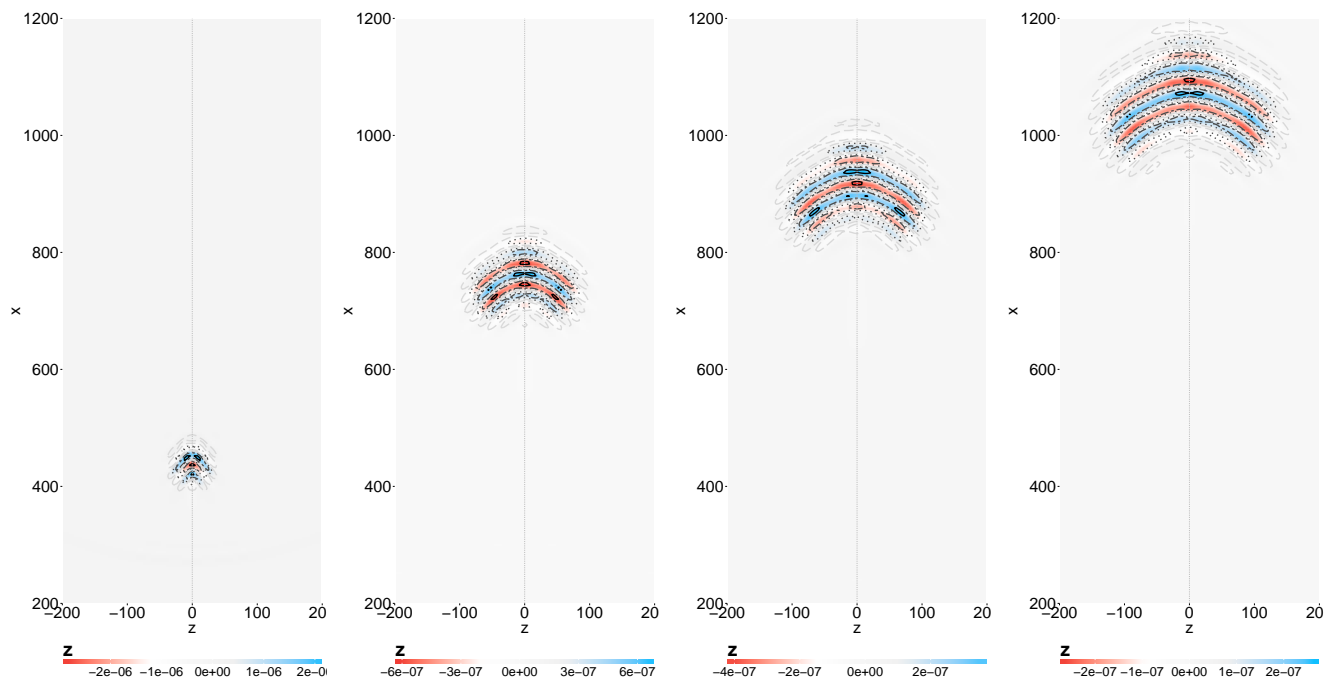


Figure 5.13: Nonlinear wavepacket at Mach 0.9, in $y = 0.6\delta^*$. Contour levels at 90% (—) , 50% (-.-), 30% (...) and 10% (- -) of the amplitude peaks in the packet.

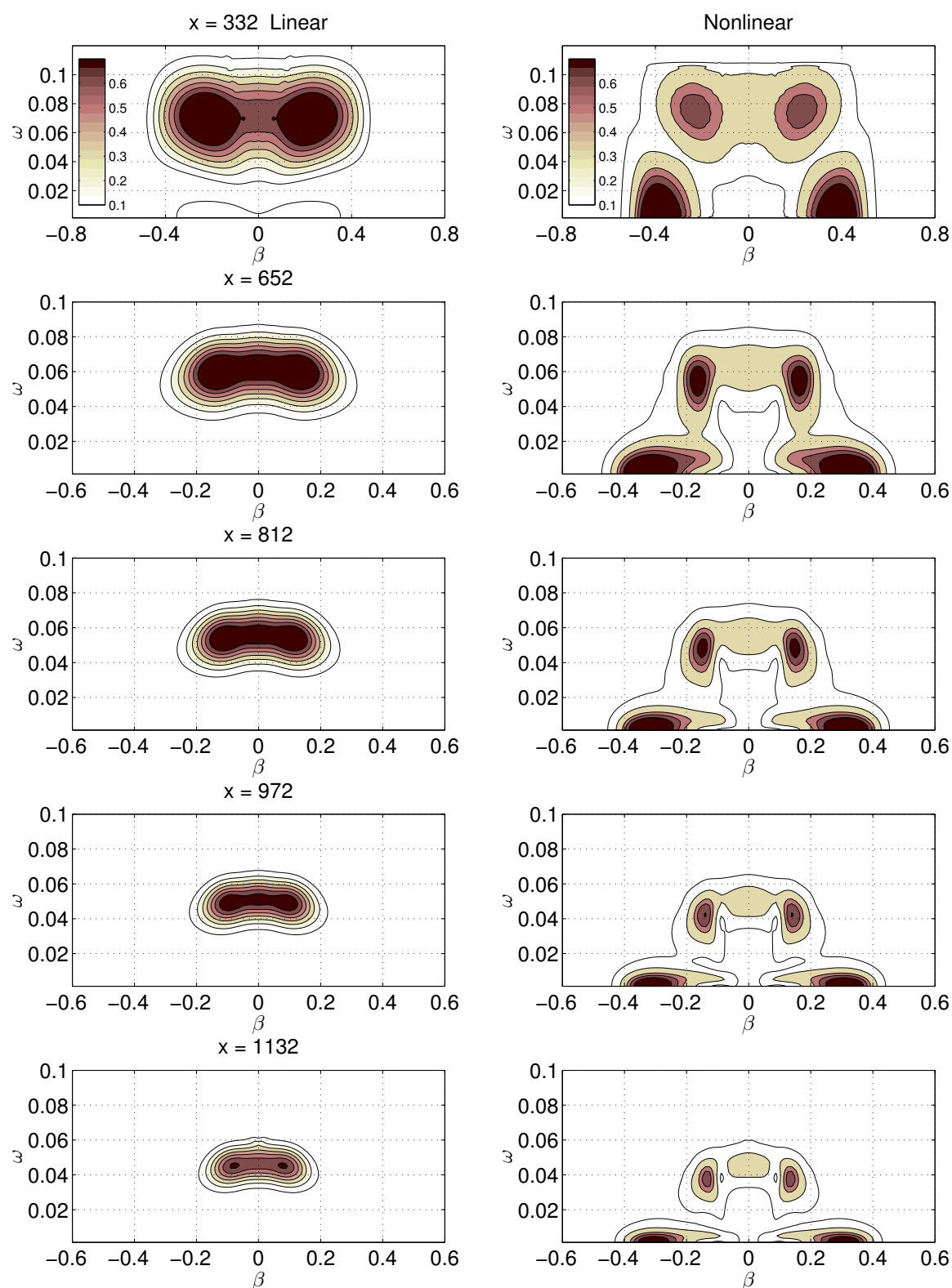


Figure 5.14: Comparison of linear and nonlinear spectrum evolution at Mach 0.9

5.3.2 Nonlinear wave packet

Evolution in the physical space (figure 5.15) shows three-dimensional structures, with strong streaks located at the center of the packet and secondary oblique waves, as was observed in the nonlinear case for Mach 0.7. In figure 5.16 are compared linear and nonlinear wave packets, and can be identified a group of oblique waves with a propagation angle $\psi \sim 45^\circ$.

In the spectral evolution (figure 5.14) only two bands presents nonlinear amplification, subharmonic and low frequency modes. From the spectrum at the position $x = 1132$ it were selected representative modes to be tracked in downstream. From figure 5.17 the linear and nonlinear bands can be separated easily. A more precise quantitative analysis can be done from the amplification curves shown in figure 5.18. Amplitude of nonlinear wave packet was chosen to be linear in a region next to the perturbation region. There are two bands of modes that amplifies nonlinearly, low frequency modes, responsible for strong streaks and subharmonic band. Low frequency modes, are strong near the perturbation source, but eventually decays, with the linear growth rate, as can be observed in the figure. Only subharmonic modes amplifies nonlinearly and in a self-sustained manner. From the spectral evolution it seems that global behavior is to decay. To investigate this respect, the domain of the simulation was extended in spanwise and streamwise, up to $x = 2500$. Resultant spectral evolution is shown in figure 5.19, and the previous behavior remains, also from the position $Re/x \sim 1100$ the subharmonic modes begin to dominate the transition process, as can be seen in the amplification curves for the extended domain, (see figure 5.20).

Finally the phase locking condition is shown in figure 5.21, for the selected mode Craik condition is satisfied, the nonlinear locking is unclear.

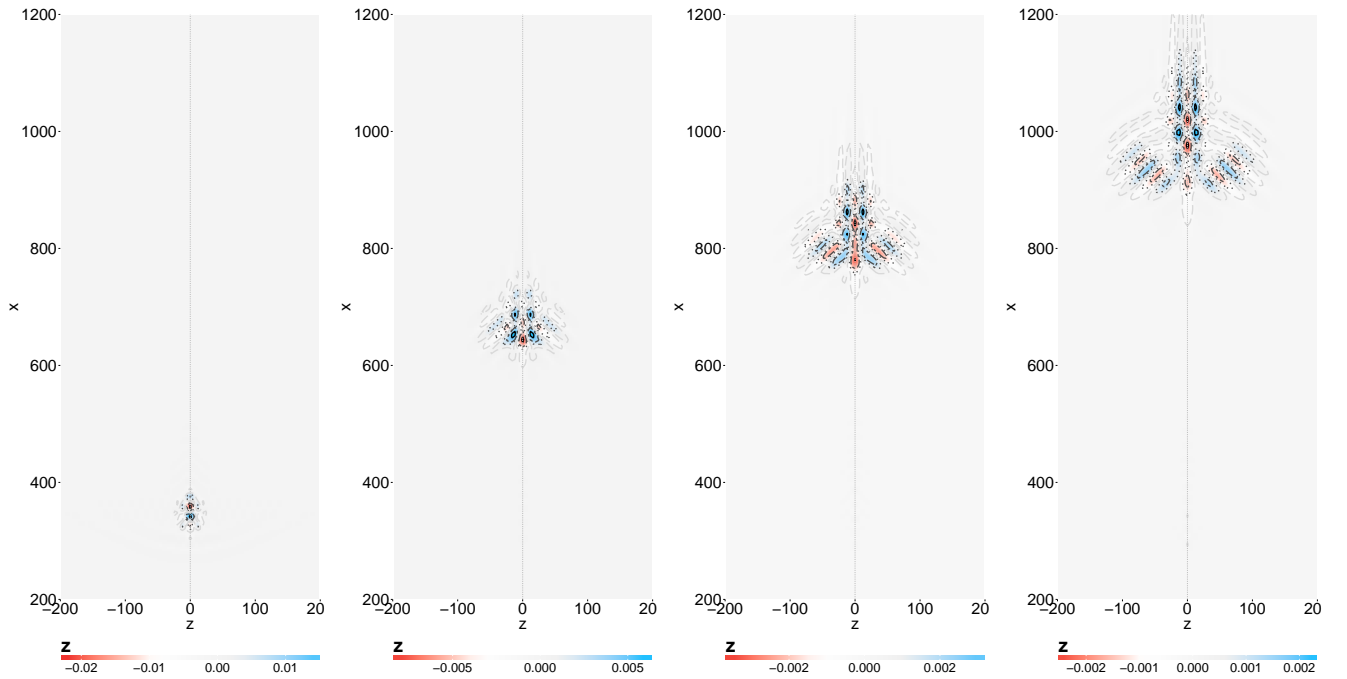


Figure 5.15: Nonlinear wavepacket at Mach 0.9, in $y = 0.6\delta^*$. Contour levels at 90% (—) , 50% (---), 30% (...) and 10% (-.-) of the amplitude peaks in the packet.

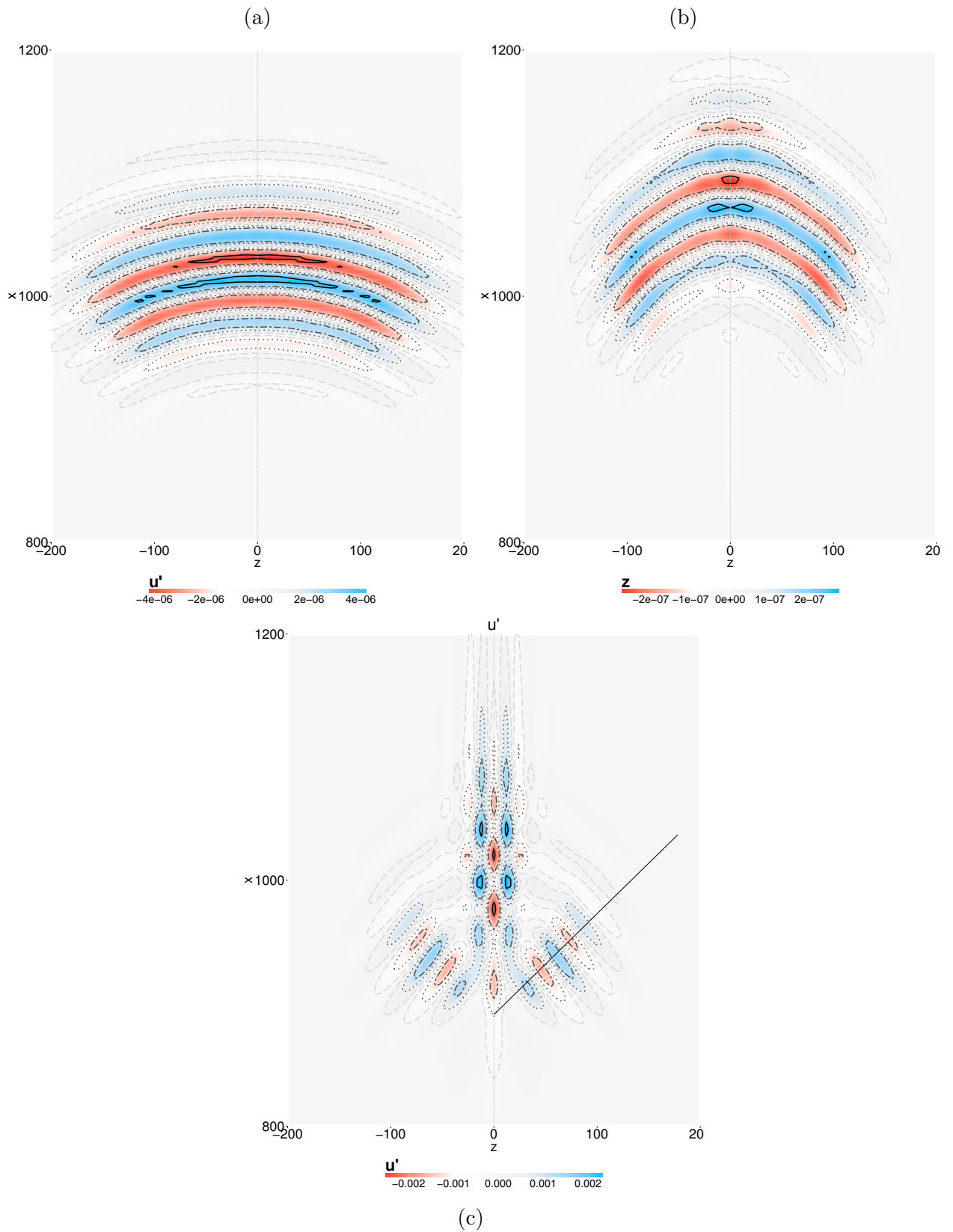


Figure 5.16: Linear wave packet on incompressible boundary layer (a) and at Mach 0.9 (b). (c) Nonlinear wavepacket at Mach 0.9, in $y = 0.6\delta^*$. Contour levels at 90% (—) , 50% (-.-), 30% (...) and 10% (- -) of the amplitude peaks in the packet.

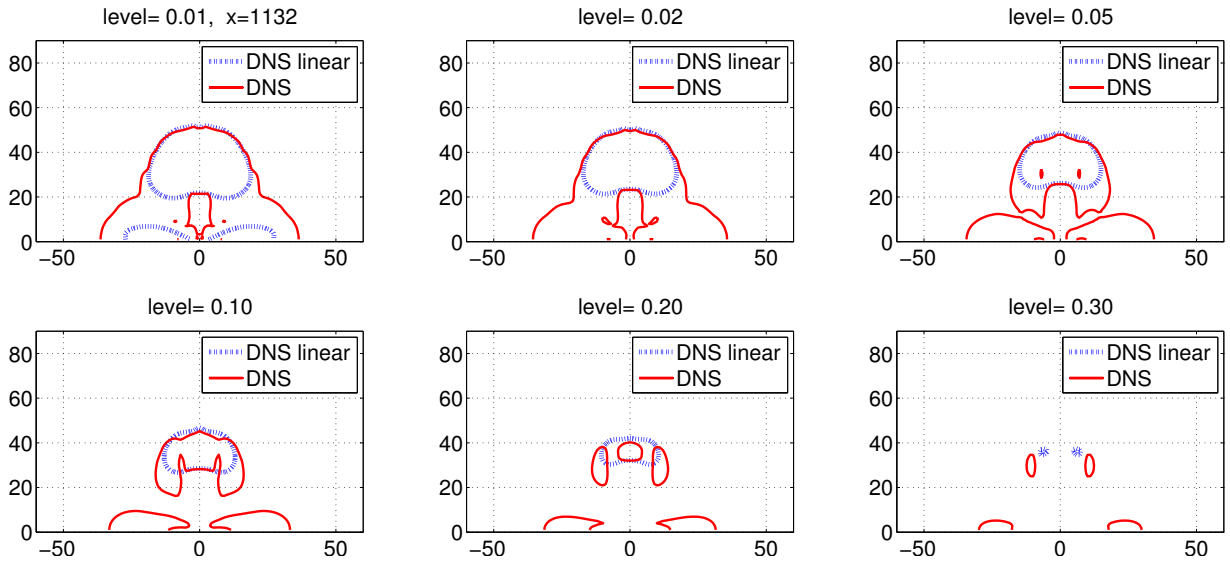


Figure 5.17: Comparison of spectrum levels at Mach 0.9 in $x=1132$.

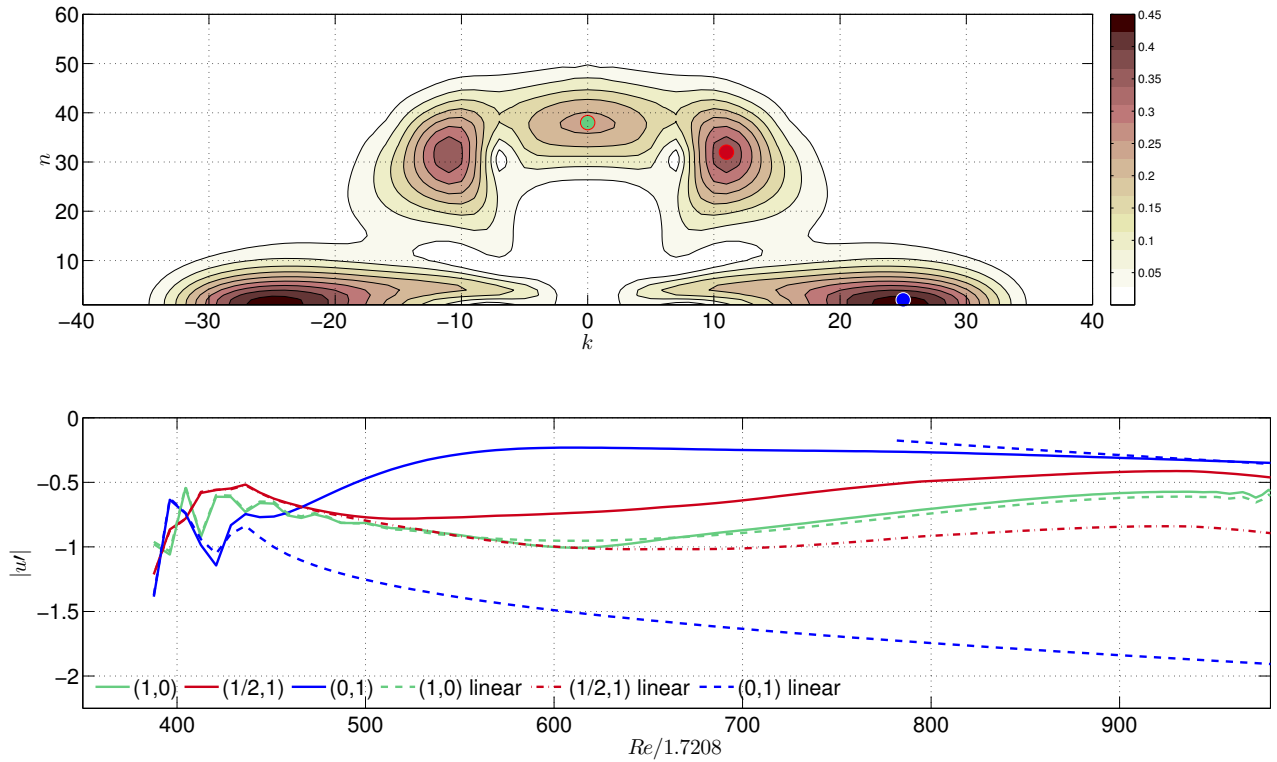


Figure 5.18: Amplification curves at $x=1132$. Streaks are dominant from the beginning, but eventually decay with the linear growth rate. Subharmonic mode remain amplifying nonlinearly.

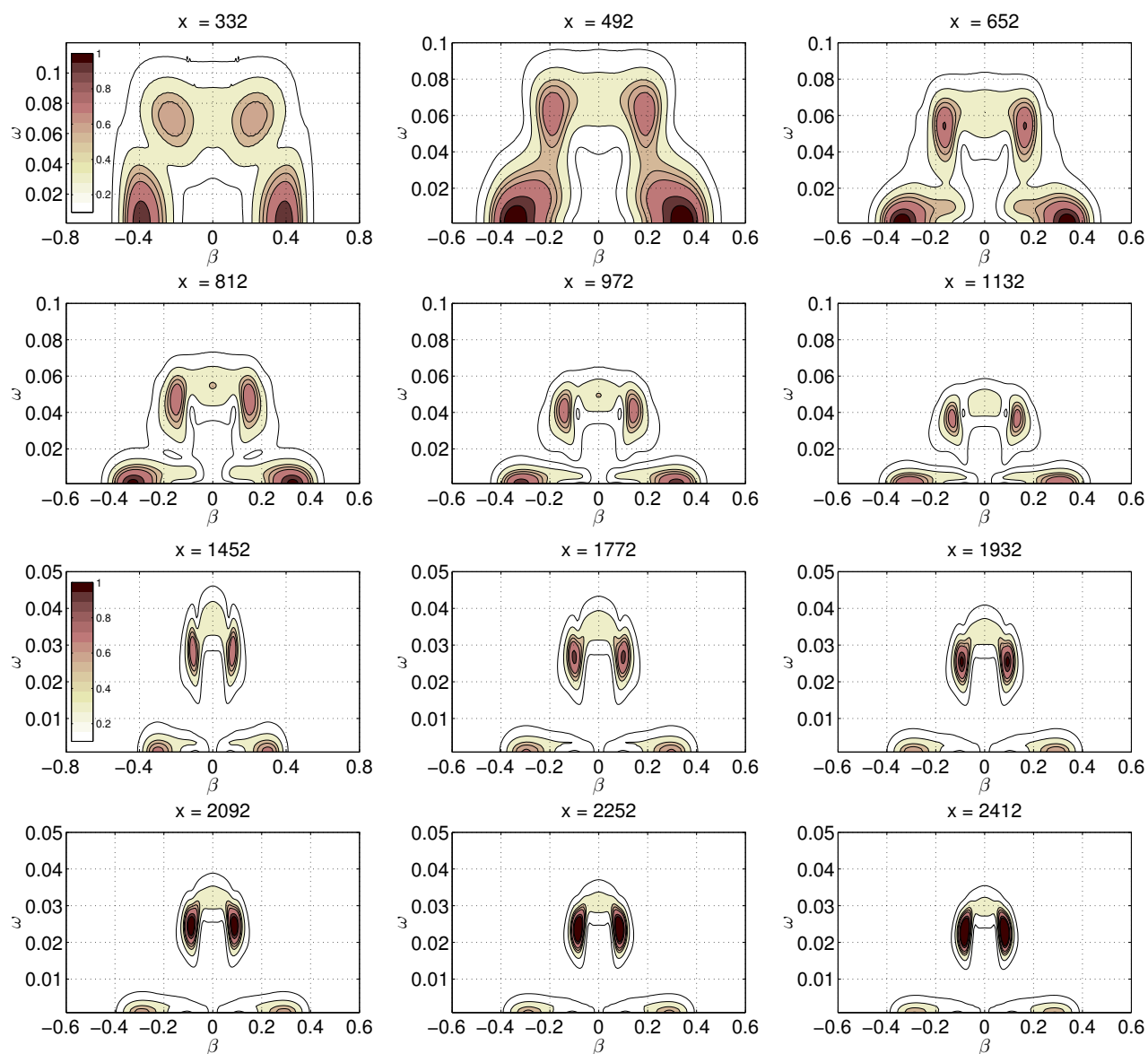


Figure 5.19: Spectrum evolution of nonlinear wave packet at Mach 0.9 in extended in streamwise, $x=2500$.

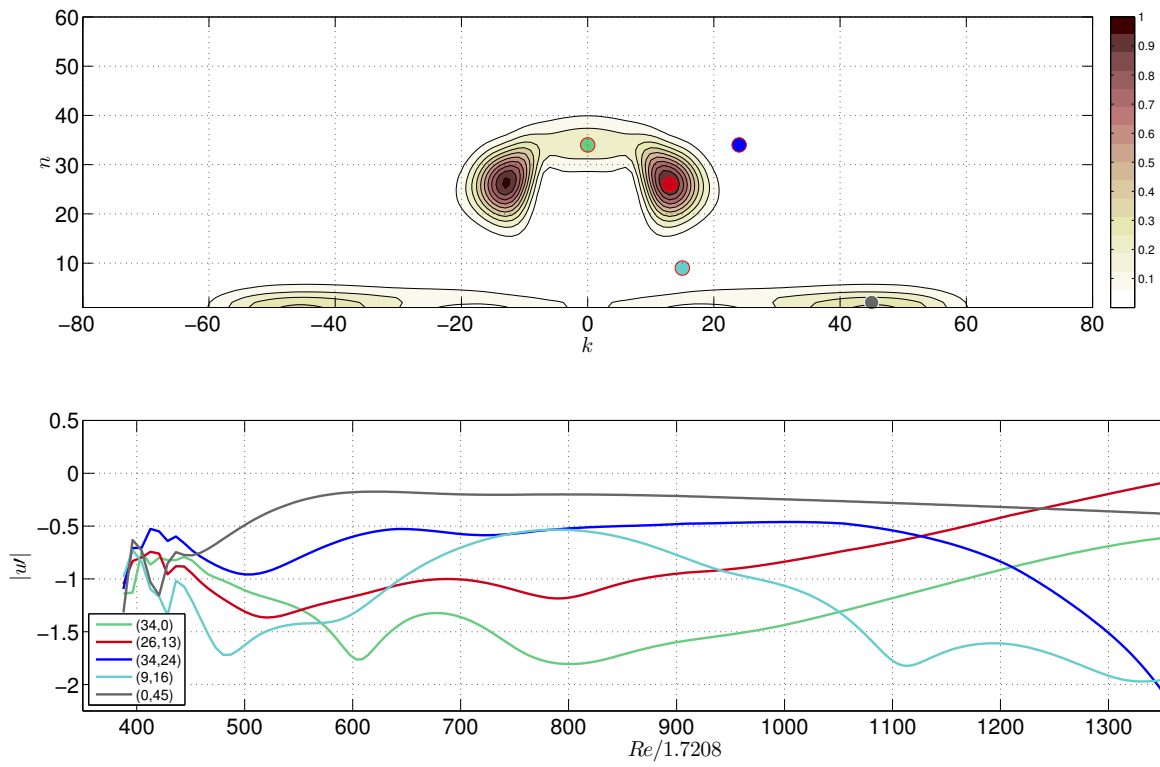


Figure 5.20: Amplification curve at $x=2412$. Streaks are dominant but are decaying.

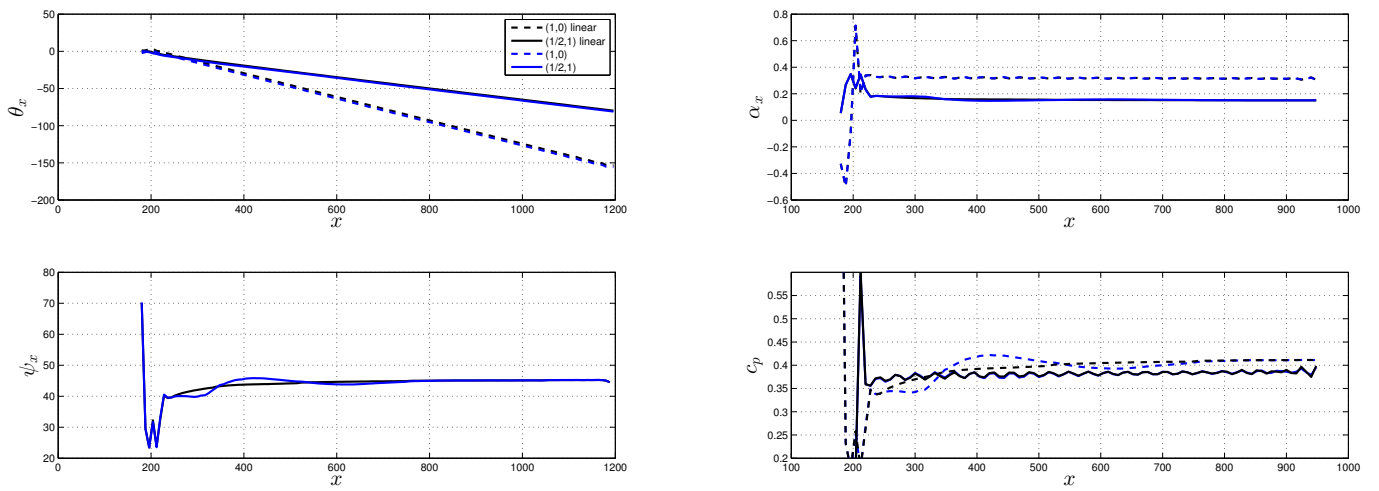


Figure 5.21: Phase locking for subharmonic mode.

5.4 Interaction between wavepackets in a boundary layer at Mach 0.9

In compressible boundary layer the nonlinear stage of the wave packet, occupies a larger region than in the incompressible boundary layer, then, the wave packet spreads along the domain, which is favorable for wave packet interaction. An isolated packet may represent a rare scenario in natural transition, spanwise interaction of packets could be more realistic model. Interaction between wave packets may be a relevant scenario in compressible boundary layers, could be a destabilizing factor. At the knowledge of the authors there are no works considering wave packet interaction.

For the wave packet interaction, two cases were considered, a pair of wave packets with two different separations, to represent 50% of overlap in linear region and 50% in the nonlinear region. The considered distances between center packets were $d = 30$ and $d = 60$ respectively. The computational domain and flow parameters were maintained. For each case a low amplitude wave packet were simulated, to be used as reference case.

5.4.1 Pair of wave packets separated by $d = 30$

In physical space, evolution for the linear pair of wave packets is shown in figure 5.22, and in the figure 5.23) for the nonlinear pair. At the initial positions the two packets can be identified easily, in downstream, they are joined in a unique structure, with a stronger modulation in spanwise than the isolated packet. The nonlinear pair of wave packets develops strong streaks, with higher amplitude than in isolated wave packet.

The spectral evolution for linear and nonlinear cases (figure 5.24) shows amplification for bands centered around specific modes. In nonlinear case, strong steady streaks are amplified.

In particular, the mode ($\omega = 0.045, \beta = 0.16$), could be generating the harmonic $(0, 0.32)$, that corresponds to the amplification of the mode, $(0, 2\beta)$, as occurs in the oblique transition.

From comparison of spectrum levels at the nonlinear position $x = 1132$, linear and nonlinear bands can be identified (figure 5.25) easily. The amplification curves were calculated for selected modes (figure 5.26) in several bands. Steady streaks display sustained growth in downstream. In general, it is observed a destabilizing effect by the pair of wave packet interaction, because modes in the others bands have nonlinear amplification, in contrast to observations on the isolated wave packet.

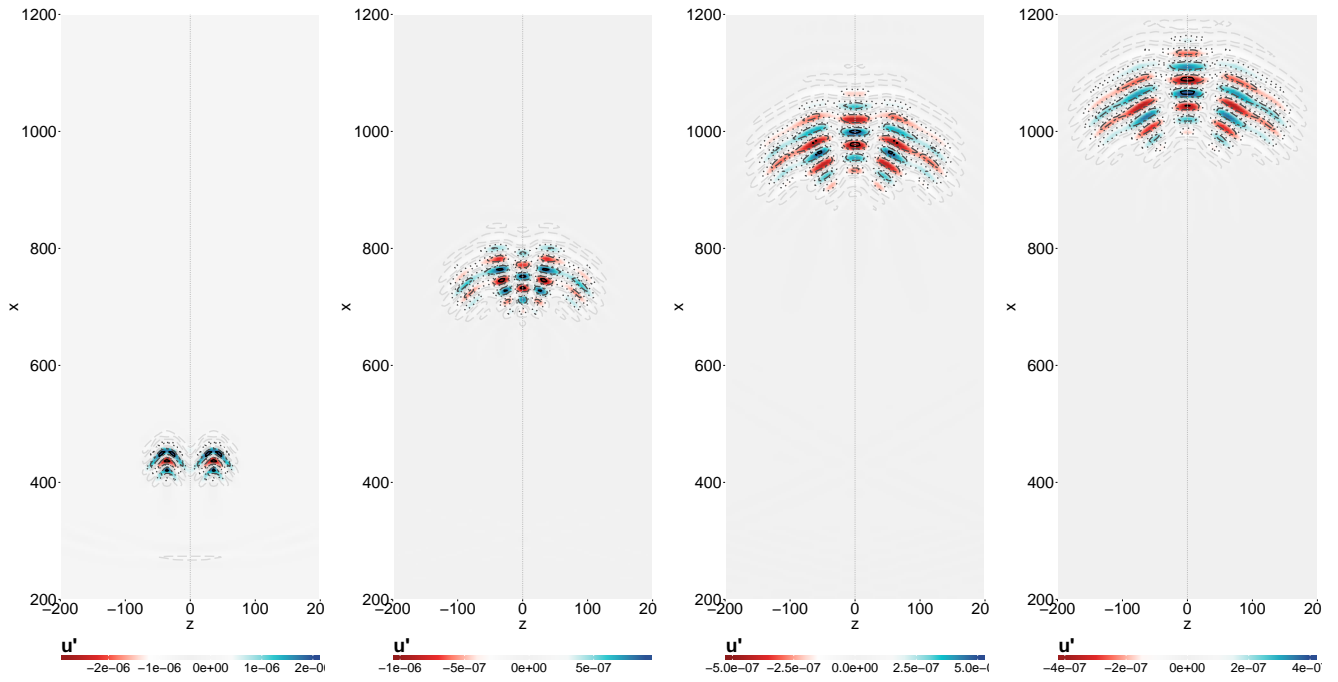


Figure 5.22: Linear evolution of a pair of wave packets separated by $d = 30$.

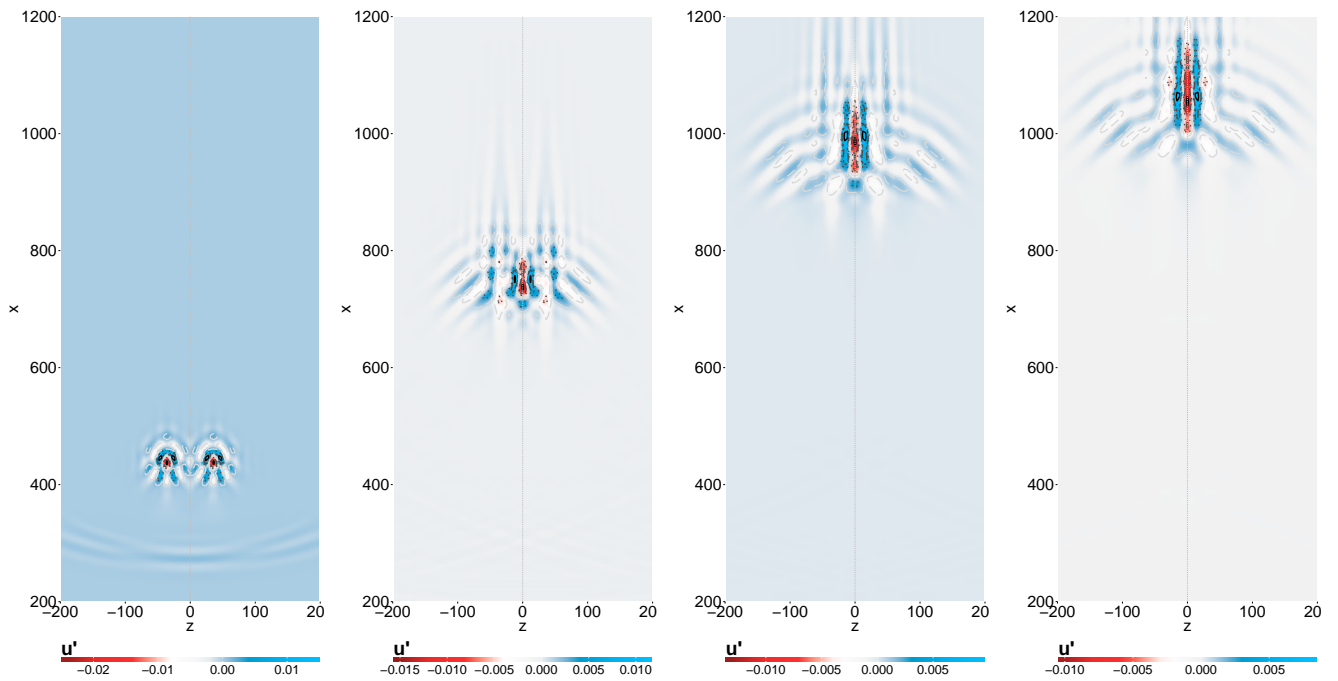


Figure 5.23: Nonlinear evolution of a pair of wave packets separated by $d = 30$.

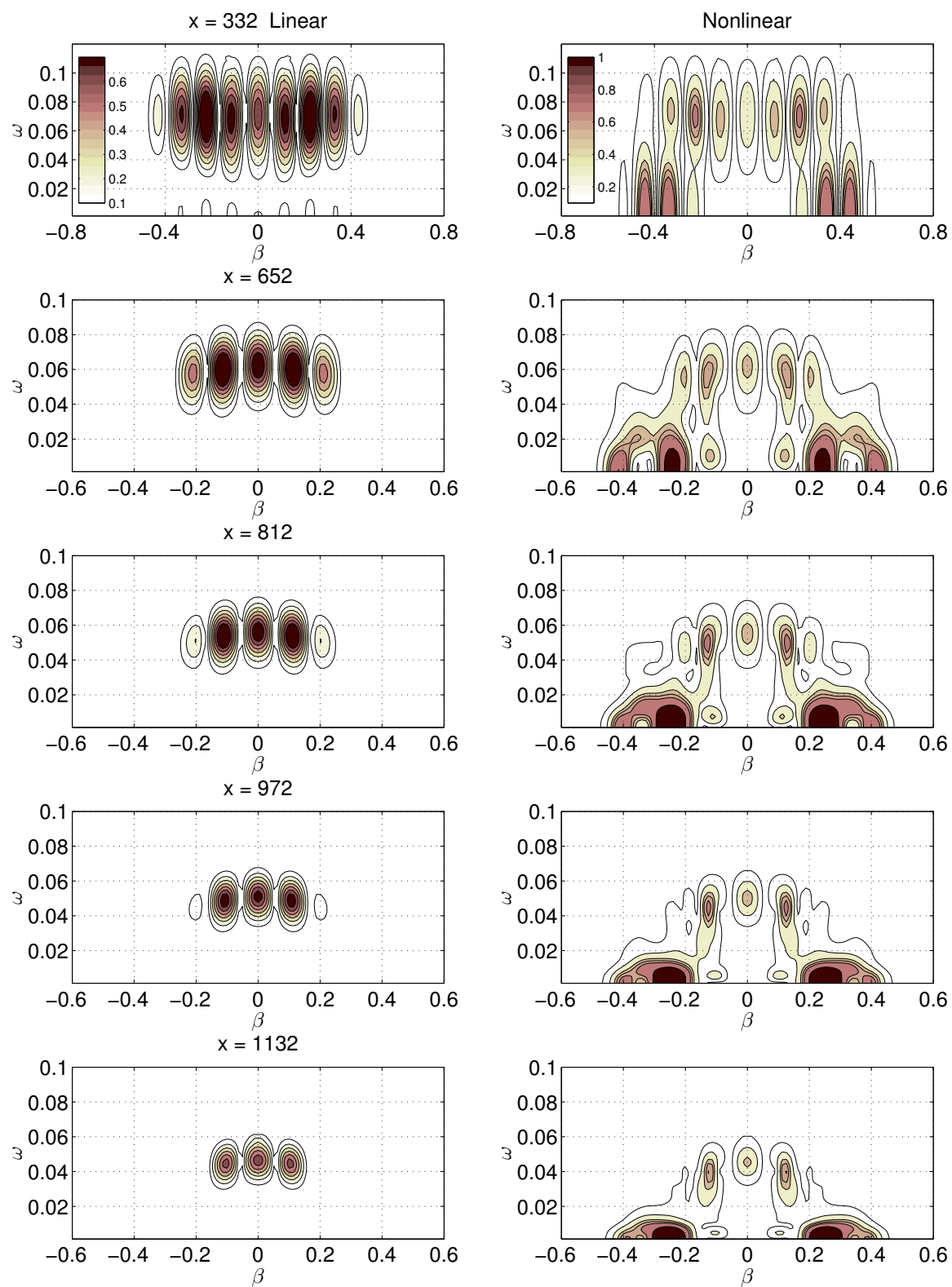


Figure 5.24: Comparison of spectral evolution for two packets separated 30.

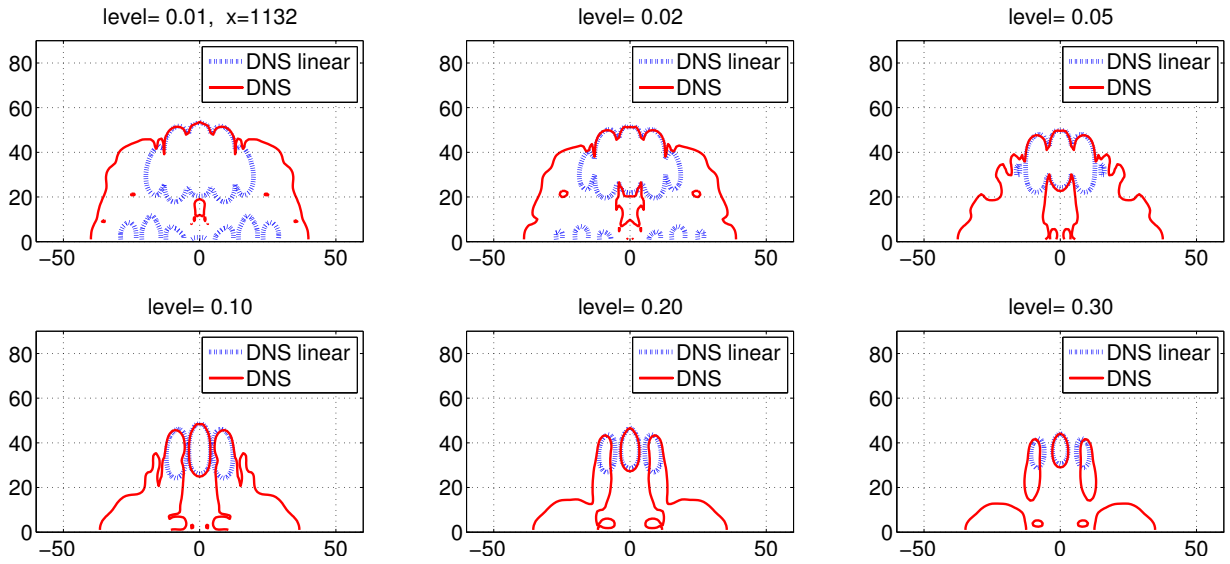


Figure 5.25: Comparison of spectrum contour levels at position $x = 1132$.

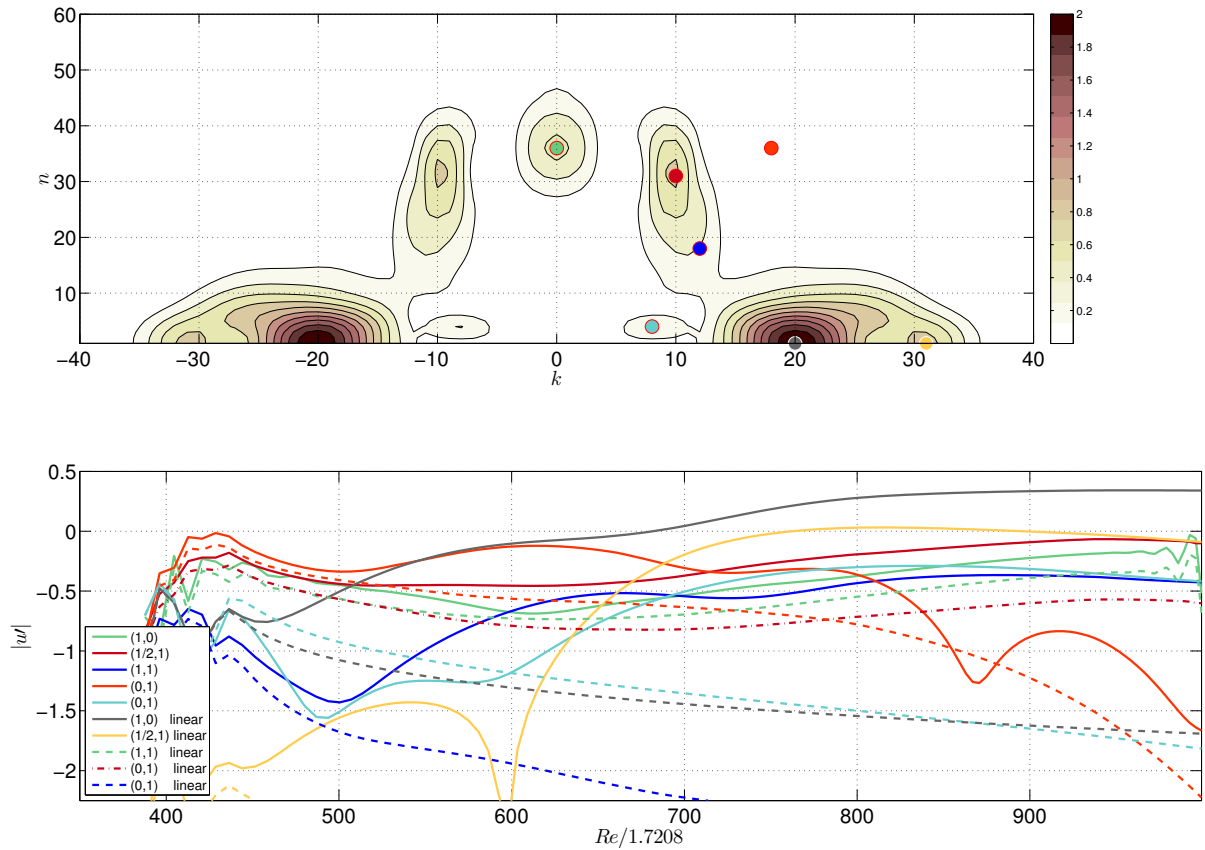


Figure 5.26: Amplification curves for a pair of wave packets separated 30 units.

5.4.2 Pair of wave packets separated by $d = 60$

In physical space, the evolution for the linear and nonlinear pair of wave packets are shown in figures 5.27, 5.28 respectively. At the initial positions the two packets can be identified easily, in downstream, they can be identified separately yet. The nonlinear evolution in the last frame in figure 5.28, resembles two isolated packets with a small interaction region at the center of the domain. The steady streaks have similar amplitudes than the isolated packet, but the overlap region, presents stronger amplitude, but weaker than in the separation $d = 30$. For better comparison in the physical space, the three cases considered, isolated packet and the two pair interaction, are shown in figure 5.29.

The spectral evolution for linear and nonlinear cases (figure 5.30) shows amplification for bands centered around specific modes. In nonlinear case, strong steady streaks are amplified.

The mode $(\omega = 0.045, \beta = 0.06)$, could be generating the harmonic $(0, 0.12)$, that corresponds to amplification of the mode, $(0, 2\beta)$. Also amplification of the mode $(0, 4\beta)$ is observed, as occurs in the oblique transition. There is also a modification on the dominant stationary spanwise mode, in relation to the previous case.

From comparison of spectrum levels at the nonlinear position $x = 1132$, linear and nonlinear bands can be identified (figure 5.31) easily. The amplification curves were calculated for selected modes (figure 5.32) in several bands. Steady streaks display sustained growth in downstream. In general, it is observed a destabilizing effect by the pair of wave packet interaction. However the effect is weaker than observed in closer pair fo packets but stronger than for the isolated packet.

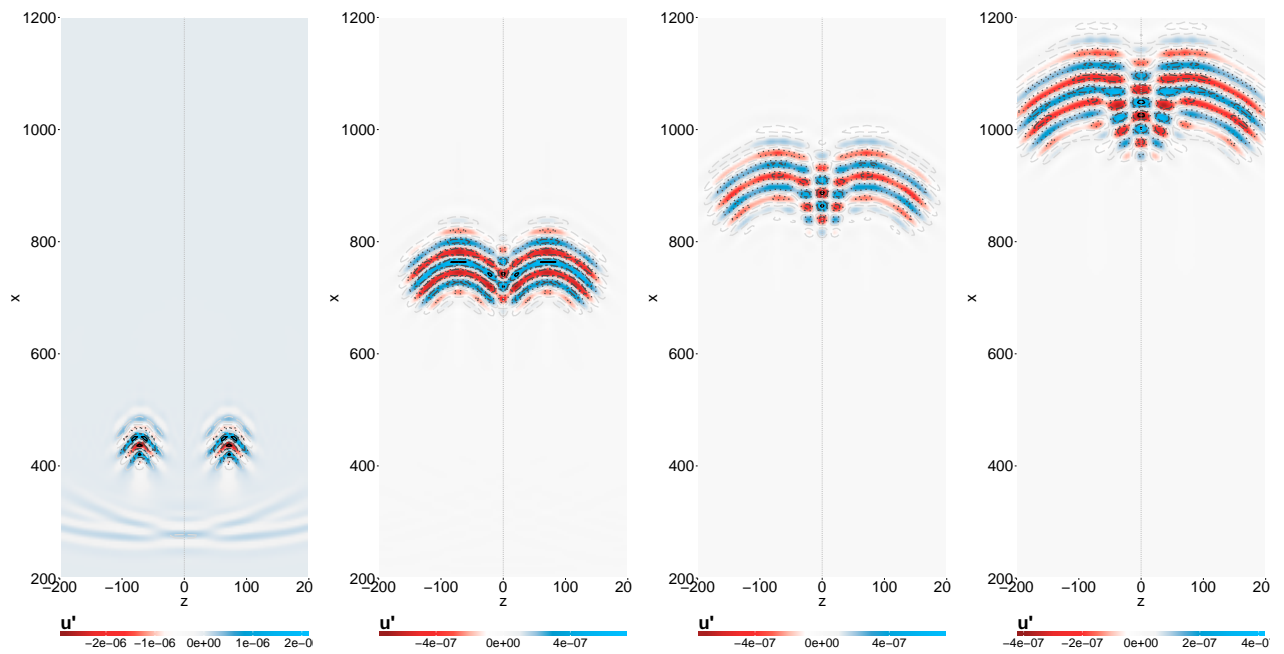


Figure 5.27: Linear evolution of a pair of wave packets separated by $d = 60$.

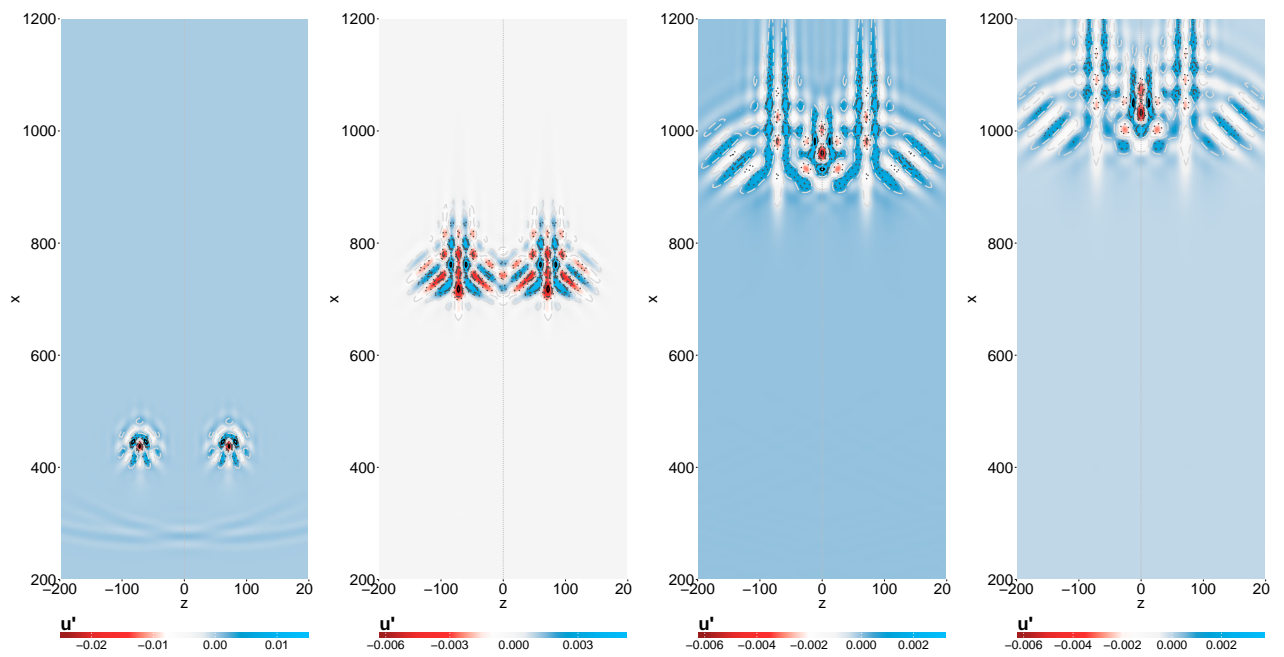


Figure 5.28: Nonlinear evolution of a pair of wave packets separated by $d = 60$.

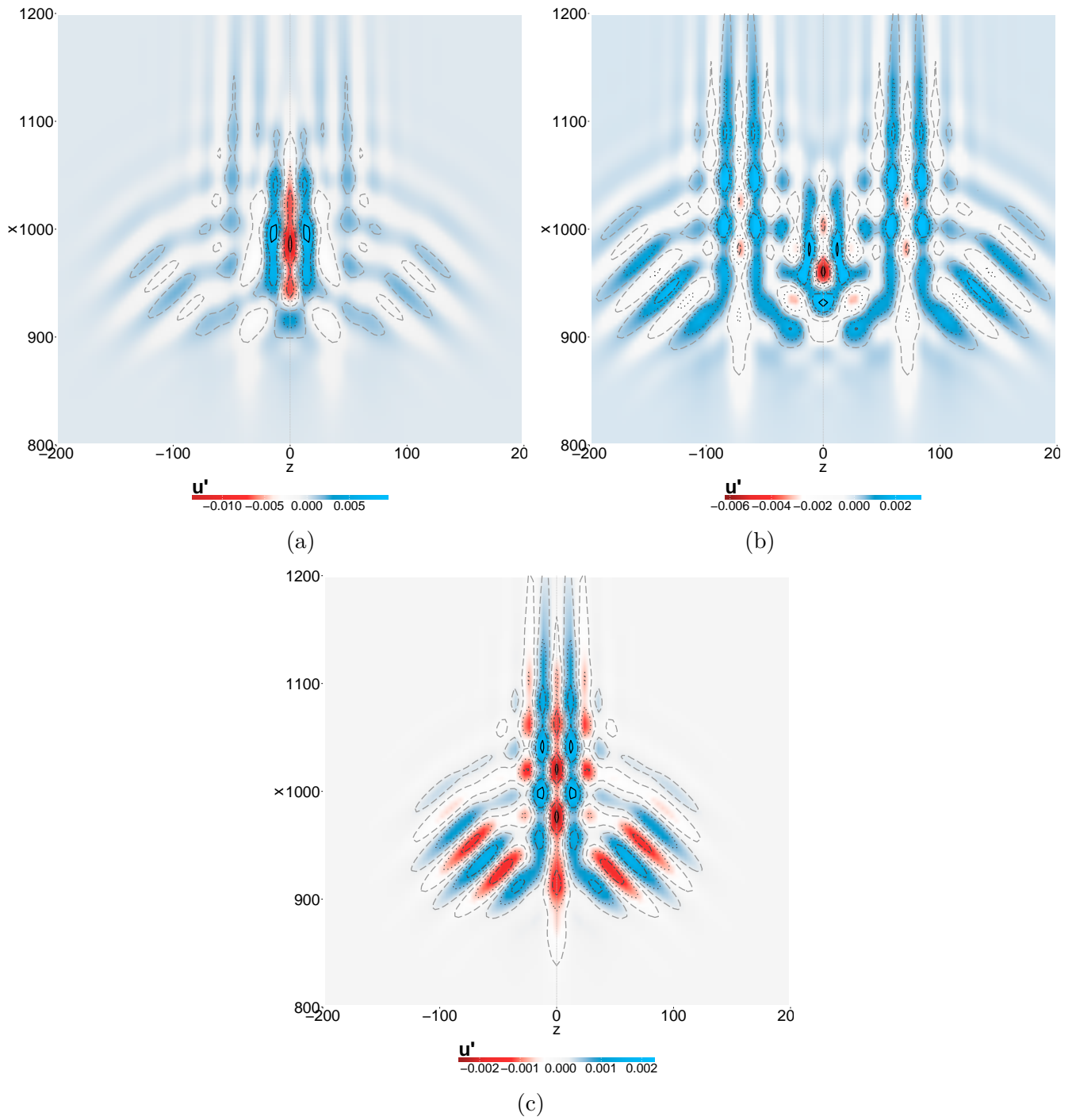


Figure 5.29: Wave packet interaction, with distances between center packet (a) $d = 30$, (b) $d = 60$, (c) isolated packet.

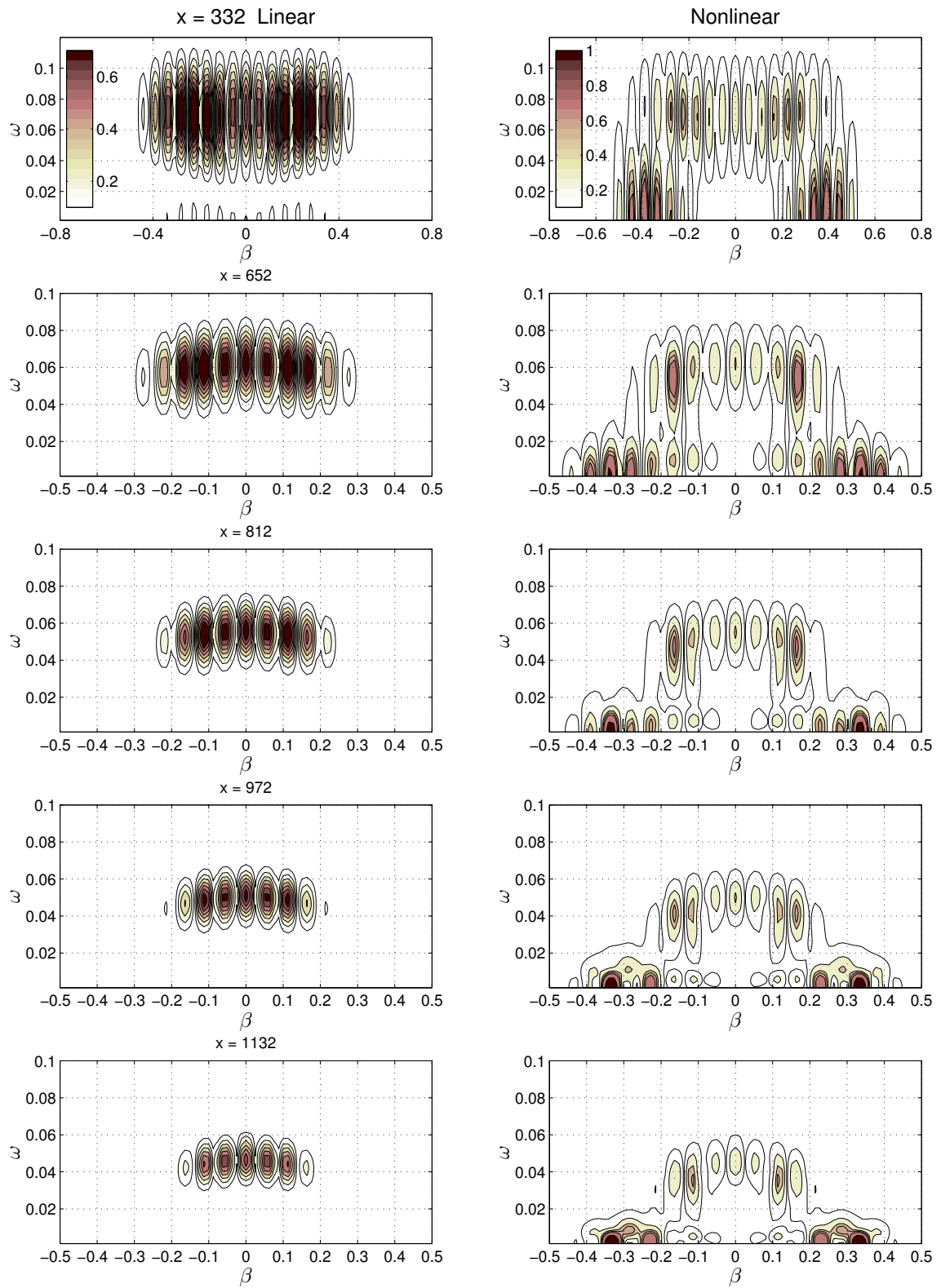


Figure 5.30: Linear and nonlinear spectral evolution for a pair of wave packets separated $d = 60$.

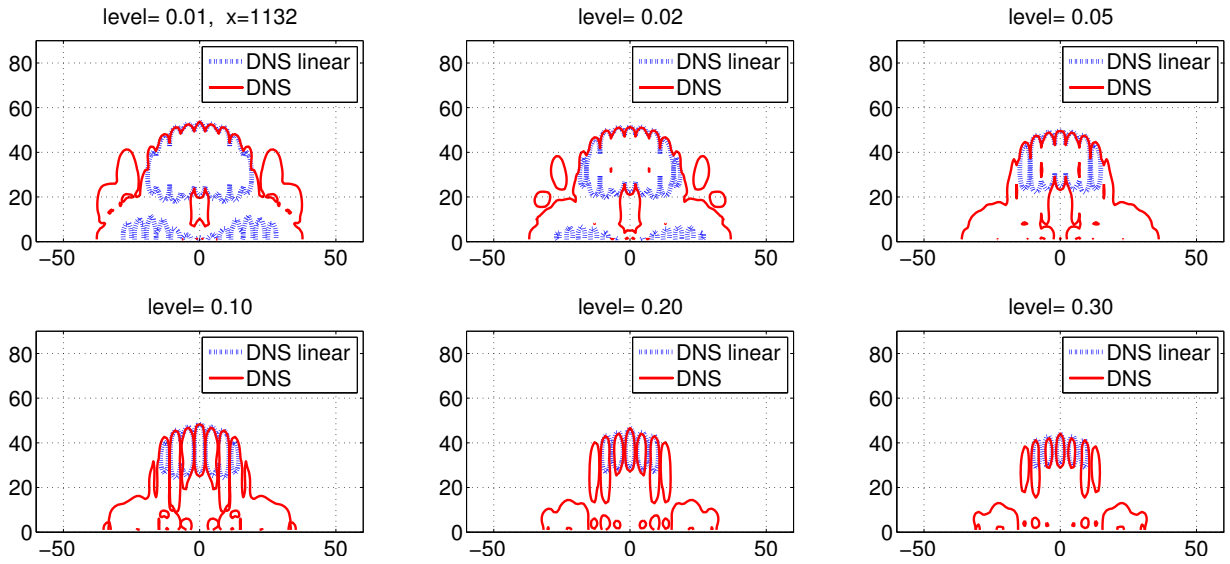


Figure 5.31: Comparison of spectrum levels for a pair of linear and nonlinear wave packets separated $d = 60$ at $x=1132$.

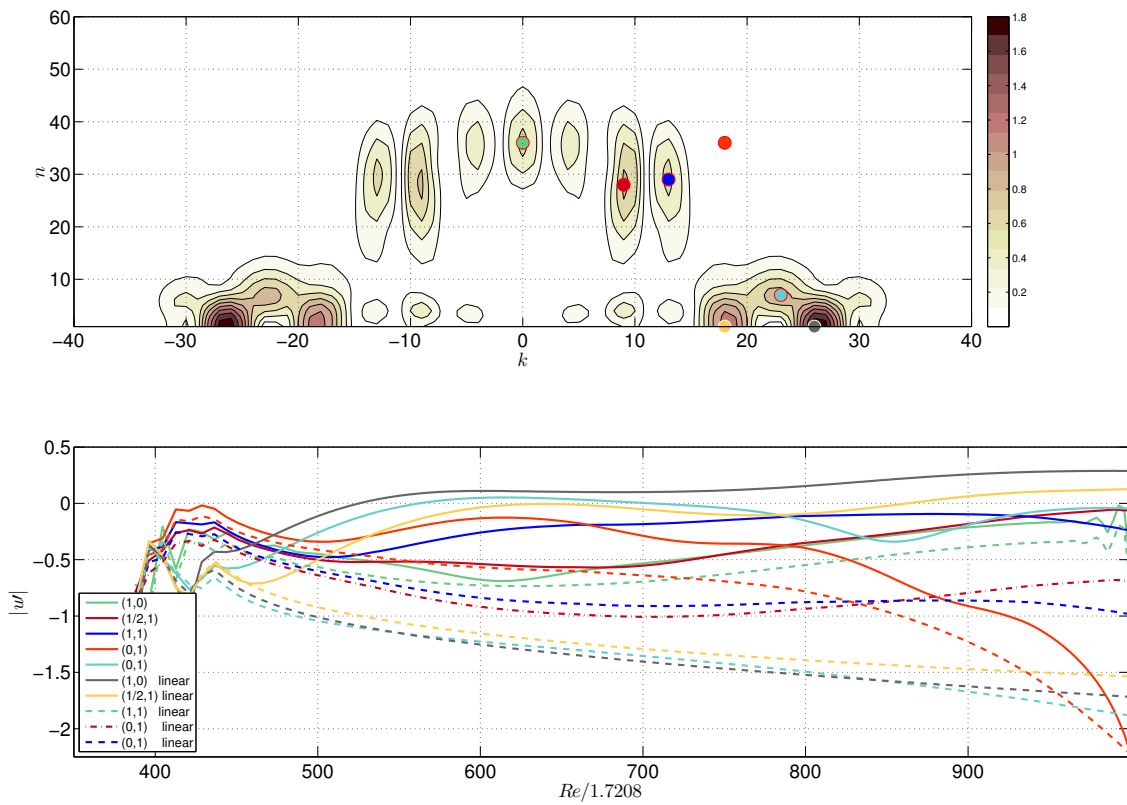


Figure 5.32: Amplification curves for a pair of wave packets separated $d = 60$.

Chapter 6

Transition generated by white noise

In subsonic and supersonic boundary layers, noise has an strong effect in the transition process, by changing spectral sensitivity of the disturbances [72]. A more realistic and hence, complicated scenario for natural transition, is transition generated by white noise. In this chapter are presented results of DNS simulations at Mach 0.2 and Mach 0.9. In both cases, a low amplitude case (linear) to be used as reference and a nonlinear evolution are considered. Also a preliminary analysis is presented. Focus of this chapter is to evidence main differences and influence of compressibility on this kind of problem, to plan future detailed works. [79, 80] investigated link between secondary instability mechanisms, wave packet evolution and natural transition for Mach 6. At subsonic Mach numbers there are no works with this approach.

The objective of these simulations is to identify main characteristics of transition induced by white noise and establish the differences with wave packet evolution. This information could help to plan future detailed analysis.

6.1 Generation of white noise disturbance

It was generated a time periodic random signal, with period $T = 2\pi/\omega_0$. Phase randomization was applied in frequency and spanwise modes, keeping the energy equal for all modes, as can be seen in perturbation spectra (figure 6.1). The perturbation function employed was:

$$v' = A_{3D} \sum_{n=1}^{N_n} \sum_{k=-N_k}^{N_k} [\cos(\alpha_0(x - x_0) \pm (k\beta_0 z + \phi_k)) \cos(n\omega_0 t + \phi_n)] \quad (6.1)$$

where $-\pi \leq \phi_n < \pi$ was generated by using *Fortrans's* rand function. For white noise simulations, the computational domain and parameters used in the Chapter 5 were maintained.

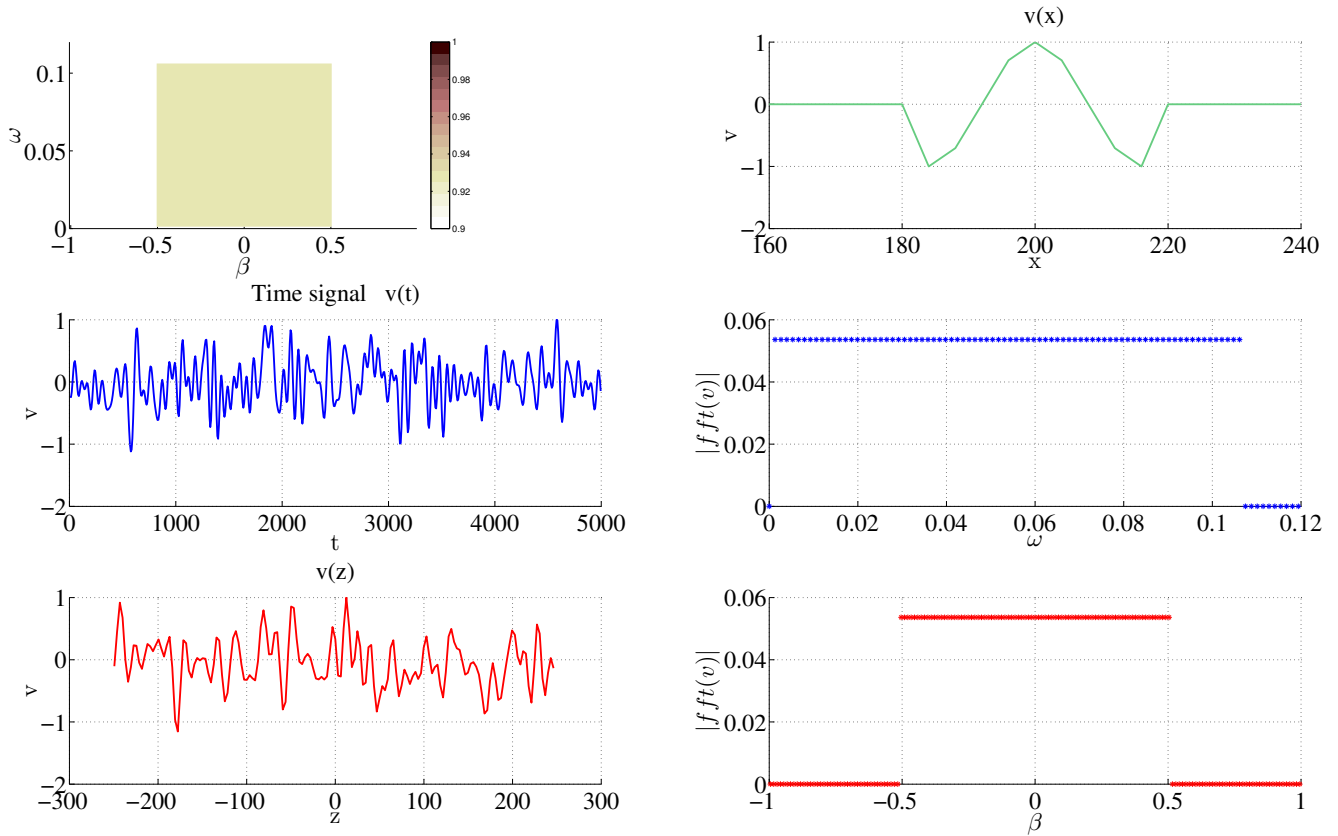


Figure 6.1: Temporal and spatial disturbances used to generate white noise.

6.2 White noise evolution at Mach 0.2

In figure 6.2 are compared linear and white noise evolution in the physical space. Linear case presents smooth distribution of amplitude across entire domain with low amplitude variations $\sim 10^{-5}$. The amplitude of the nonlinear case was chosen to have a linear region after perturbation region, but also to induce nonlinear growth in some downstream position. To observe nonlinear amplification it was needed amplitudes ~ 4 times larger than used for isolated wave packet.

In nonlinear case, lambda vortex structures are observed in a localized region, which have the higher amplitudes. This observation suggest the local presence of fundamental and/or subharmonic mechanisms. This vortex appear and disappear in time. Remembering that time signal at the perturbation source, is a time periodic random signal.

After initial transient go out of the computational domain, Fourier analysis was applied in spanwise and time. The spectrum evolution for linear and nonlinear case, is shown in figure (6.3). The linear evolution is identical to an isolated packet, because linear regime is independent of the phase, and the modes do not interact. In the nonlinear evolution linear band remains strong, but now, low frequency modes are amplified (figure 6.4). The linear and nonlinear bands can be identified in figure 6.5, from the superposition of spectrum levels.

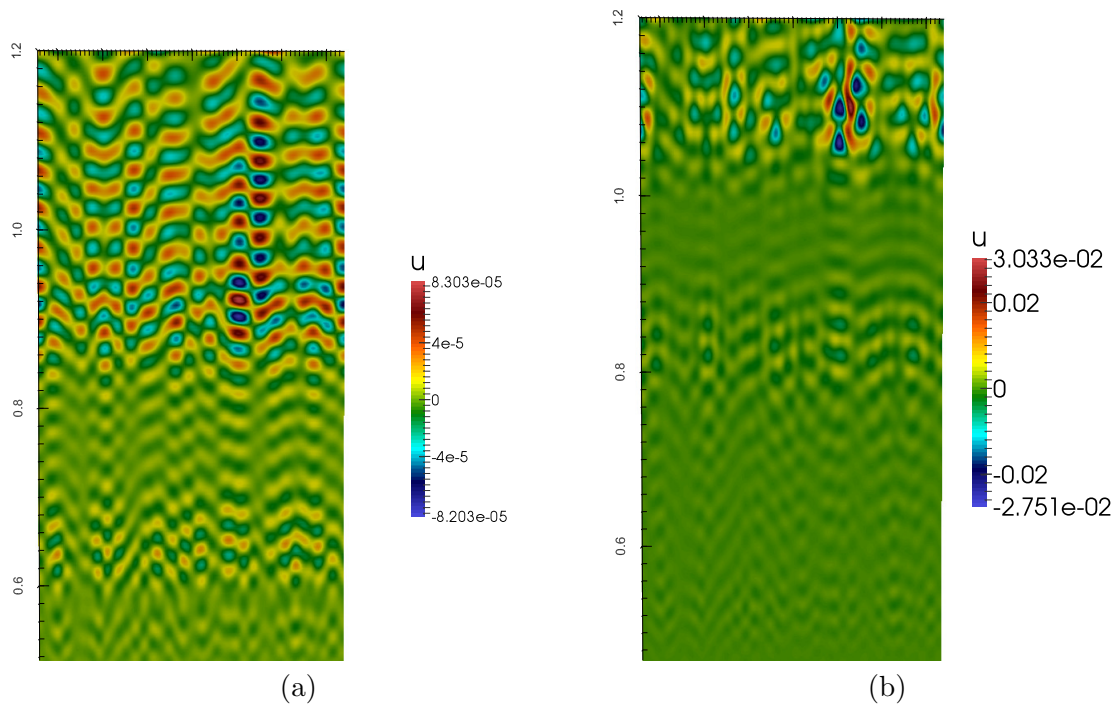


Figure 6.2: (a) Linear and (b) nonlinear evolution at Mach 0.2 for white noise disturbance. Lambda vortex are visible in nonlinear case.

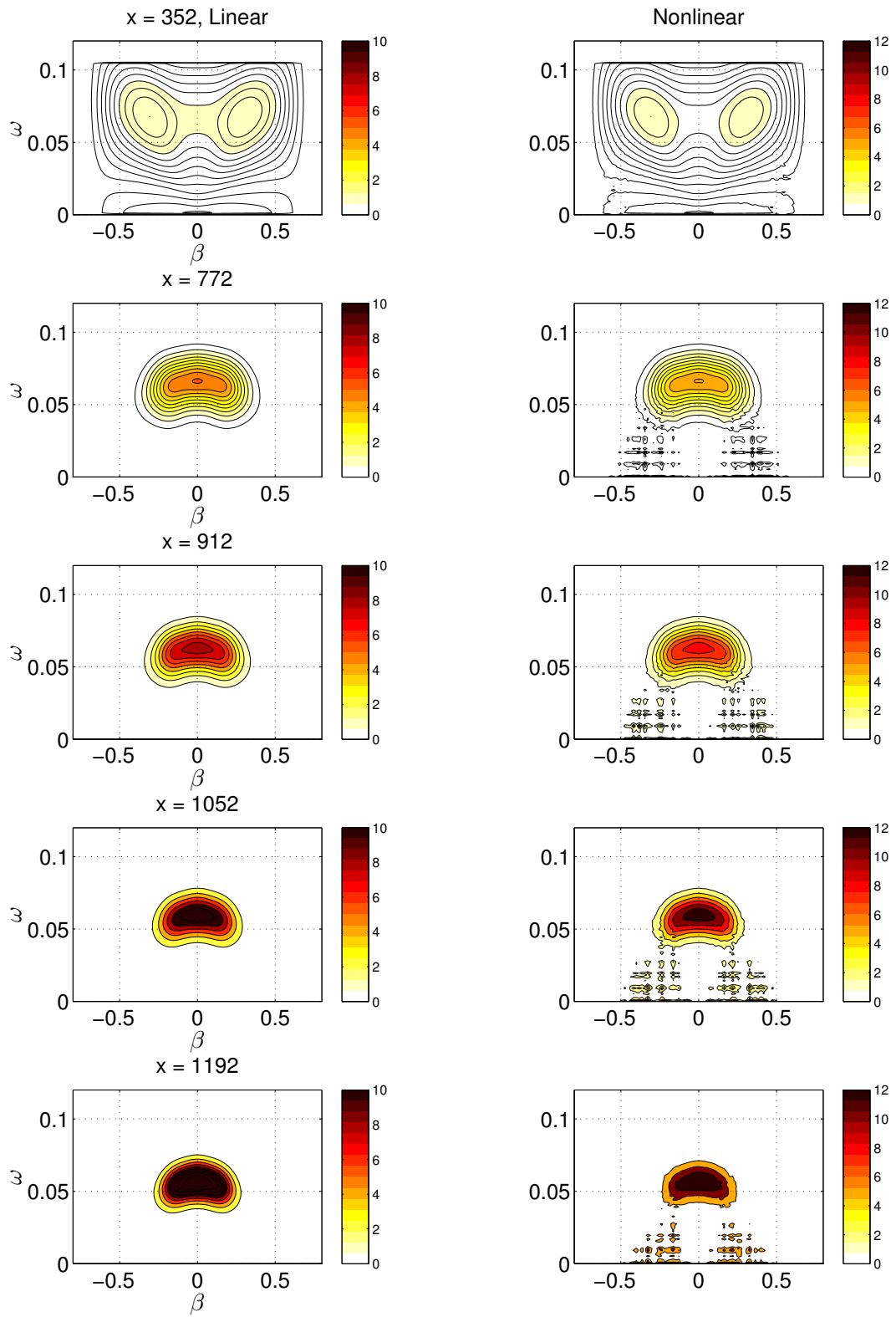


Figure 6.3: Linear and nonlinear evolution of spectral content for white noise perturbation at Mach 0.2.

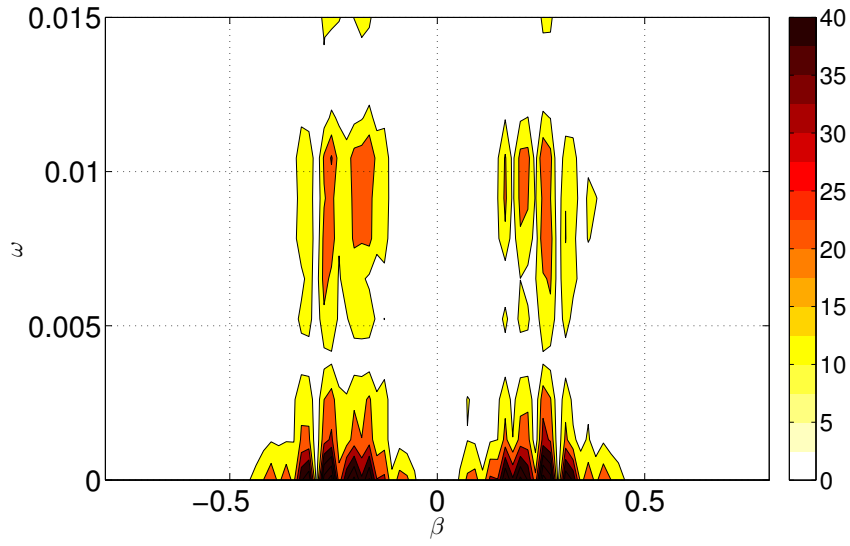


Figure 6.4: Low frequency modes (most amplified) in white noise transition at Mach 0.2.

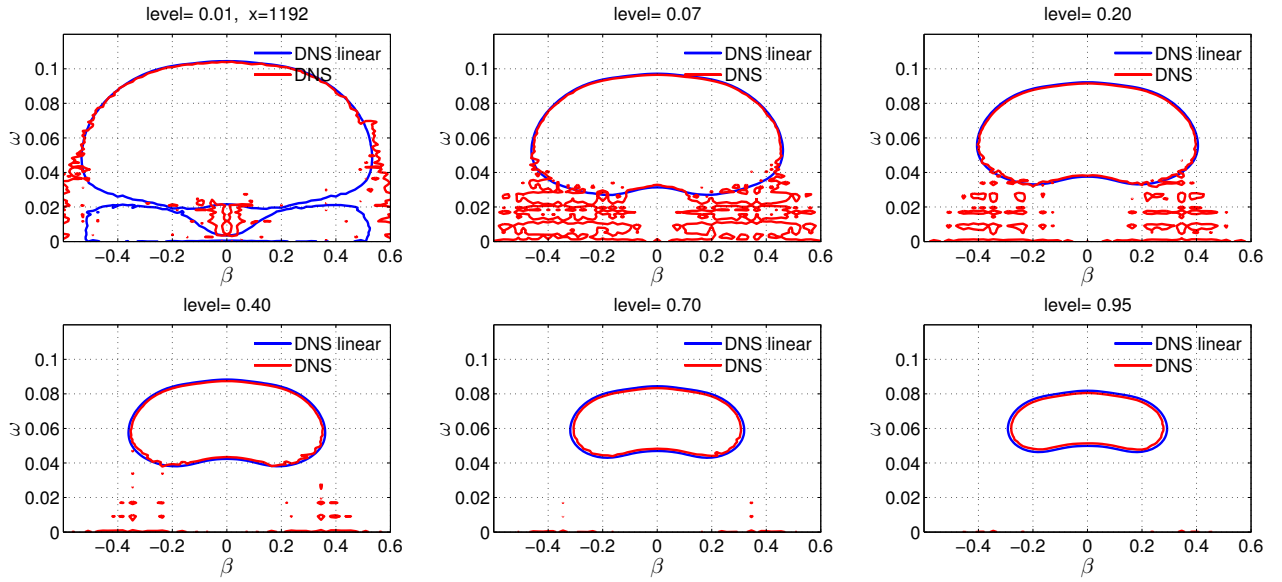


Figure 6.5: Comparison of spectral levels at $x=1192$. Low frequency modes are amplified nonlinearly.

6.3 White noise evolution at Mach 0.9

In figure 6.6 are compared linear and white noise evolution in the physical space. Linear case presents smooth distribution of amplitude across entire domain with low amplitude variations $\sim 10^{-5}$. The amplitude of the nonlinear case was chosen to have a linear region after perturbation region, but also to induce nonlinear growth in some downstream position. To observe nonlinear amplification it was needed amplitudes ~ 4 times larger than used for isolated wave packet.

The nonlinear case result is totally different from incompressible white noise evolution. Now, from a position around $x \sim 0.6$, longitudinal streaks are observed along the entire domain, that could be linked to oblique transition. After initial transient go out of the computational domain, Fourier analysis was applied in spanwise and time. The spectrum evolution for linear and nonlinear case, is shown in figure (6.7). The linear evolution is identical to an isolated packet, because linear regime is independent of the phase, and the modes do not interact. In the nonlinear evolution, the linear band, is now very weak, in contrast to incompressible case. Low frequency modes are amplified strongly (figure 6.8). The linear and nonlinear bands can be identified separately by superposition of the spectrum levels (see figure 6.9). A preliminary localized analysis was performed, by applying a Gaussian windowing in the time domain, as shown in figure 6.10. Low frequency modes are the strongest. Also, in this figure, the format of a wave packet can be observed.

An interesting aspect to note here, is that the wave packet interaction seems to reproduce better aspects of the white noise transition, because in the nonlinear pair packet interaction, streaks modes were amplified. A more realistic model for natural transition could be constructed considering wave packet interaction, justified by the previous observations.

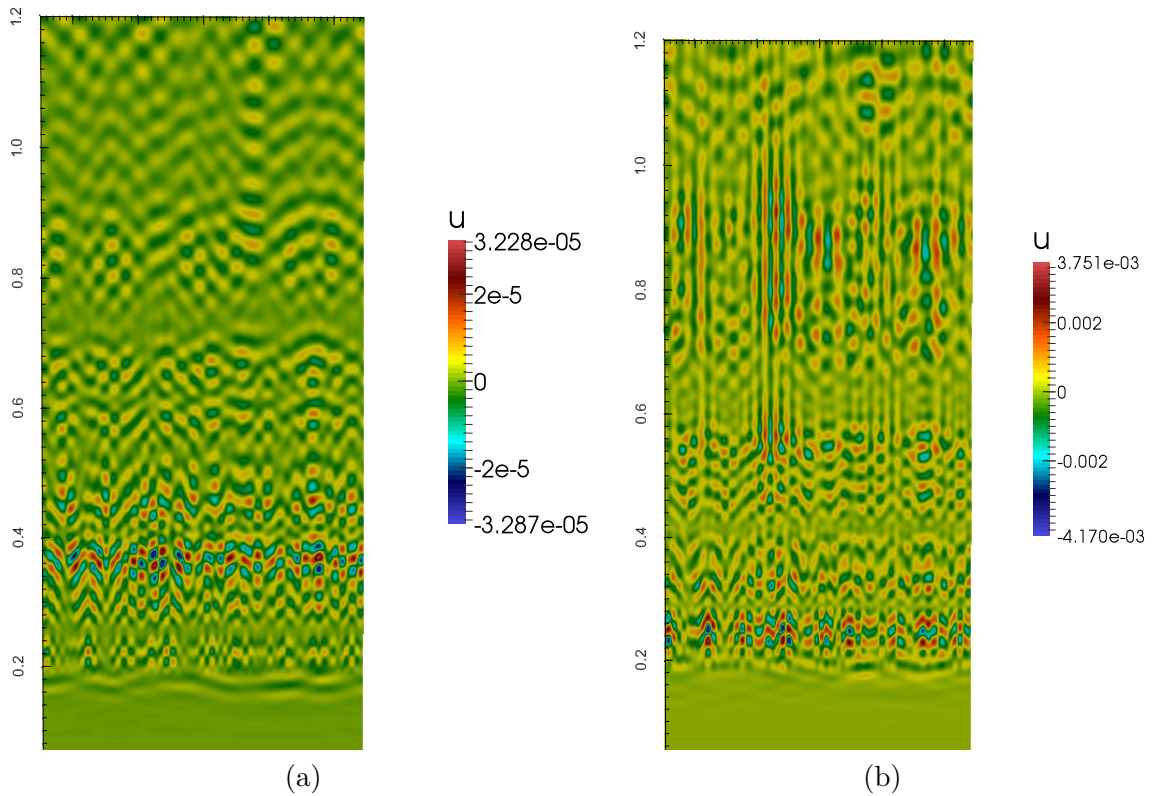


Figure 6.6: (a) Linear and (b) nonlinear evolution of white noise at Mach 0.9.

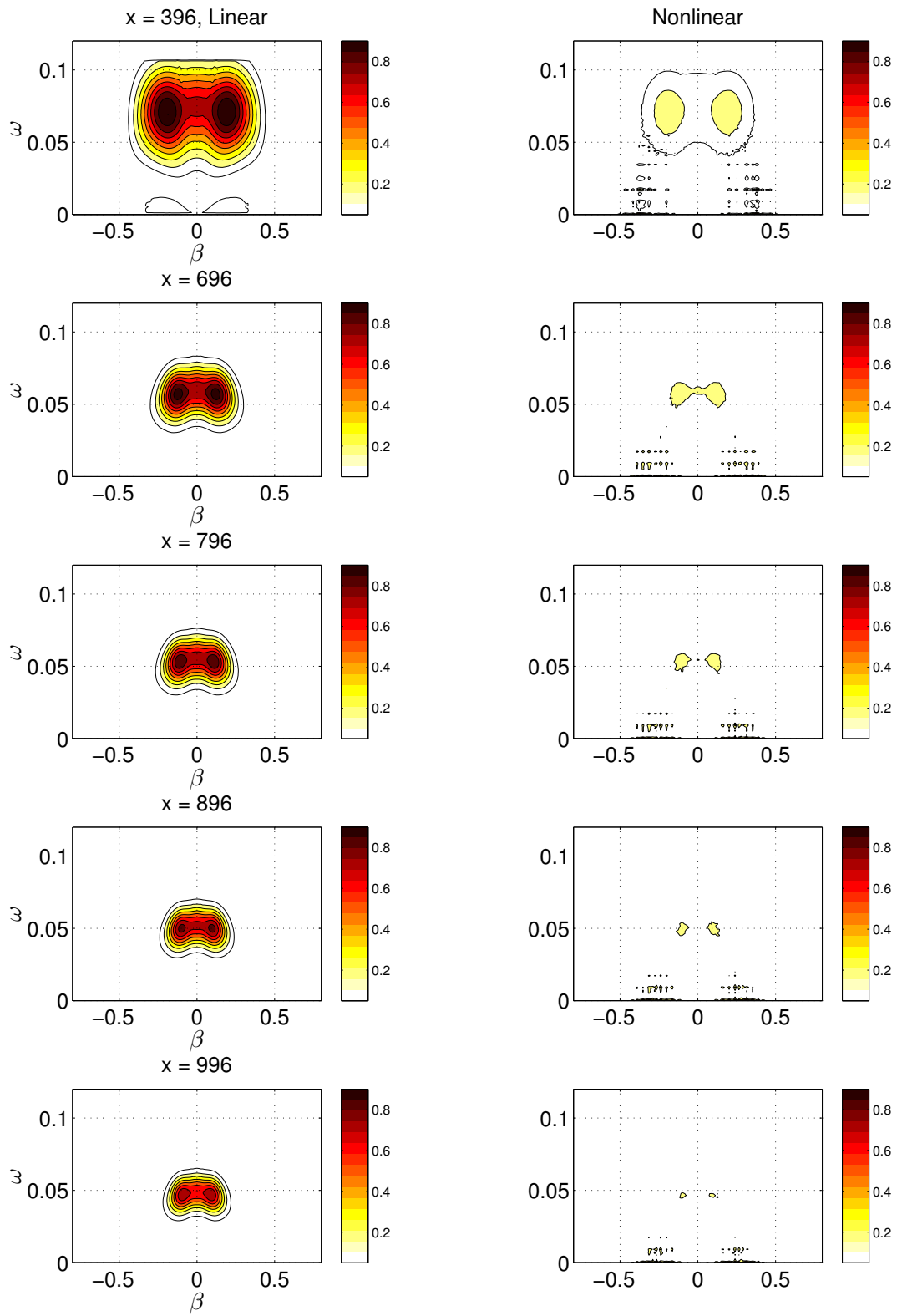


Figure 6.7: Evolution of a white noise perturbation at Mach 0.9.

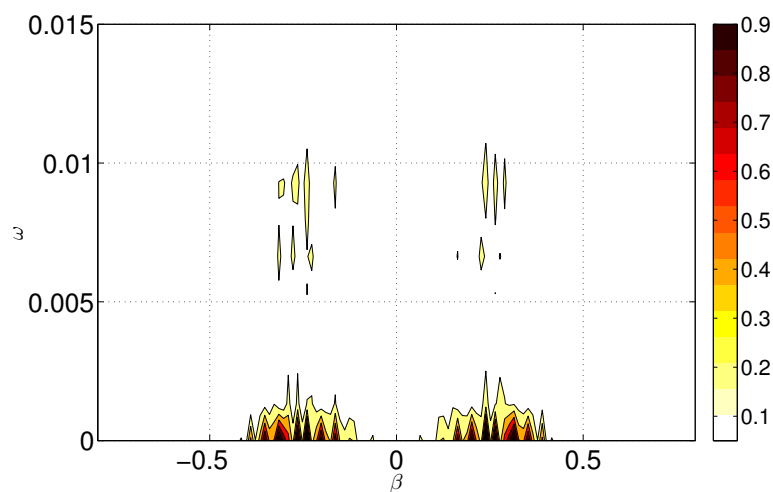


Figure 6.8: Most amplified modes in nonlinear amplification for white noise perturbation at Mach 0.9.

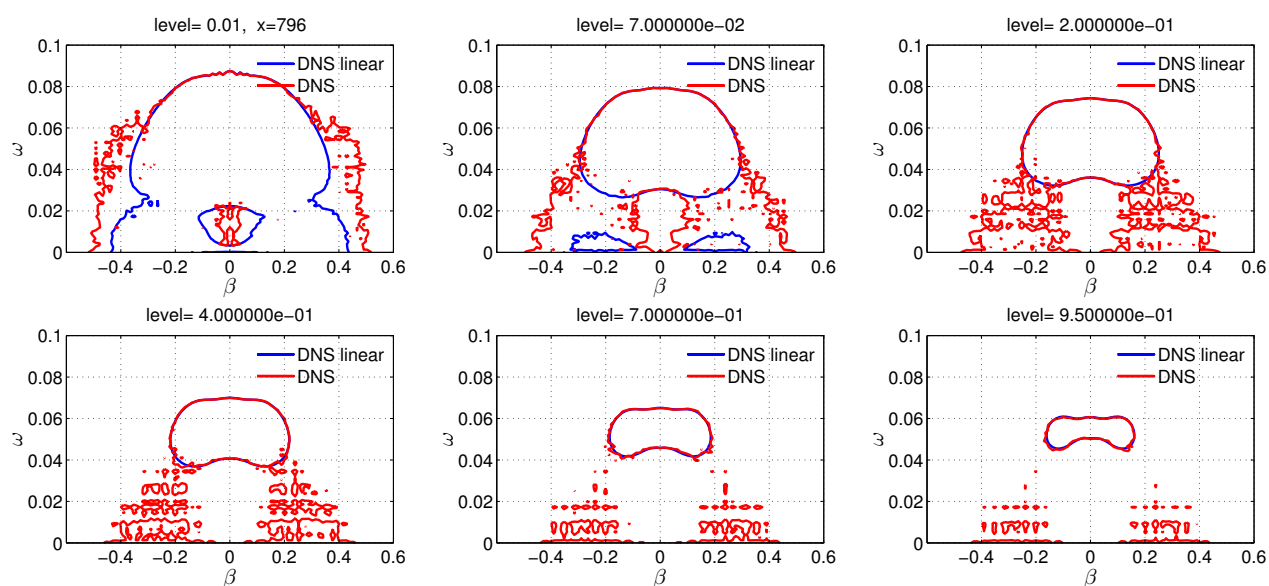


Figure 6.9: Comparison of spectral levels at x=796.

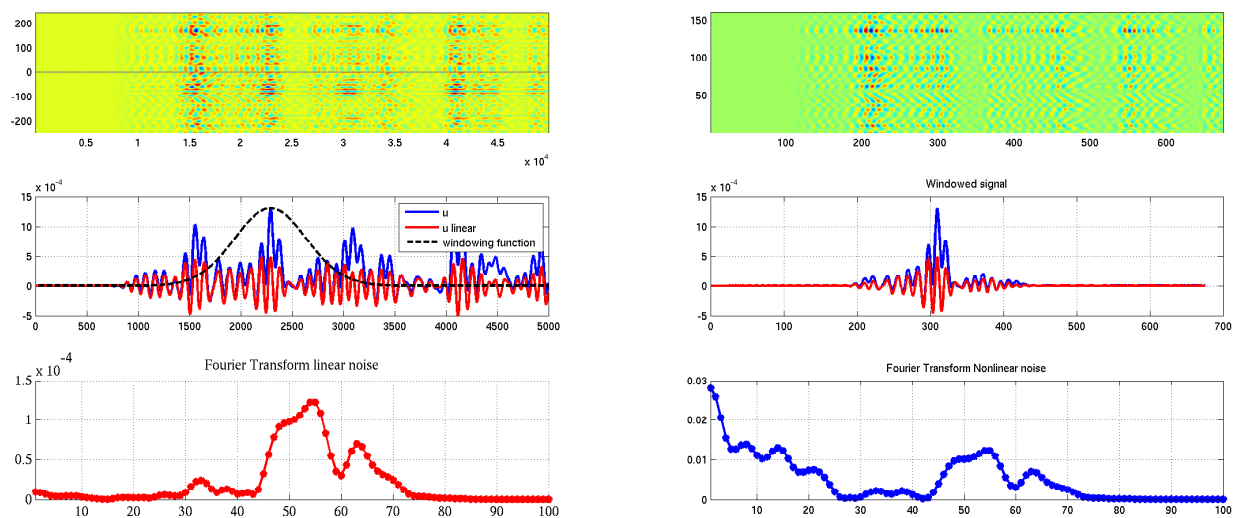


Figure 6.10: Gaussian windowing

Chapter 7

Conclusions and suggested work

7.1 Conclusions

A DNS code was developed, to investigate problems on transition in compressible boundary layer on a flat plate. Code validation tests were performed, on linear and nonlinear stages of transition, on incompressible and compressible regime. The focus of the work is to investigate natural transition in subsonic boundary layer, modeled by wave packets and perform a preliminary study of transition induced by white noise. Three main problems were considered, numerical simulation of the experiment [54] on incompressible boundary layer, the influence of compressibility on wave packet evolution at subsonic Mach numbers and finally, a preliminary study of white noise evolution in a boundary layer at Mach 0.2 and 0.9.

Comparison between numerical and experimental results [54] are in a very good agreement in the linear and nonlinear stages, in both, spatial and Fourier spaces. Considering the higher grid resolution of the computational domain it was performed a nonlinear modal analysis in two bands, subharmonic and fundamental. A detailed analysis of this kind is not found in the literature for wave packets in the incompressible boundary layer. In the subharmonic band, nonlinear amplification was compared with the controlled case of H-type breakdown, several variables of selected modes were calculated. The growth rates, phase locking and threshold amplitude of the 2D wave of selected modes in wave packet, corresponds with this mechanism.

In the fundamental band it were selected two groups of modes, with the same spanwise wave number and varying their frequency. As reported by [13], both bands have strong nonlinear amplification. The effective amplitude of the 2D mode in the case of controlled transition is of the order of the amplitude of the wave packet. Finally, to investigate the origin of subharmonic modes, they were removed from the perturbation spectra. The resultant wave packet from this disturbance, presents almost an identical subharmonic band as in previous case, then, subharmonic modes are generated by nonlinear interaction.

Also, phase locking process is observed between the primary and secondary waves, evidencing the presence of K-type and H-type breakdown. Comparison of the amplification curves for modes with high spanwise wave numbers in the experimental domain, shows good agreement in the growth rates, but the intensity level is underestimated in the the DNS simulation. To attempt determine the cause of this discrepancy, in the DNS simulation it were included two effective experimental conditions. The experimental pressure gradient and experimental asymmetry, last one, added by performing a calibration on each mode in an experimental linear position, in the Fourier space.

Results of these simulations show no influence of these factors on the intensity levels of the modes in the fundamental band. Finally disturbance amplitude was increased in 20% to study amplitude effect on the wave packet. In relation with the previous case, main differences are in the fundamental modes, which have

higher levels, similar to the observed experimentally, however subharmonic growth rates now are overestimated. Amplitude have a stronger effect on the fundamental modes.

Influence of compressibility in wave packet evolution was investigated in the boundary layer at Mach 0.7 and Mach 0.9. In the linear regime, in both cases were observed lower growth rates, than in the incompressible boundary layer, DNS simulations shows that linear growth rates at Mach 0.9 are 10 times lower than for Mach 0.2. The frequency of the mode 2D most linearly unstable, decays with Mach number.

At Mach 0.9 the most amplified linearly mode is oblique, as is evidenced in the spectral evolution.

At Mach 0.7 two disturbance amplitude were considered, at the highest amplitude, all the selected modes in separated bands have nonlinear amplification. With the lower disturbance amplitude, only modes in the subharmonic band have nonlinear growth. Results suggest that nonlinear mechanisms triggered in the transition process, depends on the disturbance amplitude. Wave packet at Mach 0.9 shows a more stable character, only have amplification in the subharmonic bands. No higher amplitude could be considered because the resultant wave packet was nonlinear from the source.

To represent a closer scenario to natural transition, wave packet interaction of a pair of wave packets were considered at Mach 0.9. This value of Mach number was chosen to be typical of aircraft passenger at cruise. For the wave packet interaction, two pairs of wave packets were simulated, varying the relative distance between them. In contrast to the isolated wave packet case, both packet pair have strong nonlinear amplification in several bands. The stationary modes nonlinearly amplified, suggest the presence of oblique resonance. Closer packets have a strong nonlinear behavior than the packets more distant. In general, it was found that packet interaction have a more unstable character than isolated wave packet.

Finally evolution of a disturbance generated by white noise was performed, by phase randomization. In the linear regime spectral evolution is identical to the linear wave packet, as expected, because the phase has no influence in this regime. Nonlinear results for Mach 0.2 and Mach 0.9 are completely different. In the incompressible boundary layer are observed localized lambda vortex structures, that could be associated to the local presence of H-type and/or K-type resonance. In the compressible boundary layer, from a position in downstream, longitudinal vortex are generated, they are distributed across the entire domain. By comparison of the results at Mach 0.9, for isolated wave packet, the packet pair interaction and the transition generated by white noise, the wave packet interaction is a better representation of white noise transition, because has an destabilizing effect and develops longitudinal vortex, as occurs for the the transition induced by white noise. However, it is needed a localized analysis to investigate in detail this kind of transition. As a general conclusion, in white noise evolution, compressibility has an stronger effect that in wave packet evolution.

7.2 Suggested work

In the wave packet evolution there are several parameters that deserve a systematic investigation, to identify their role separately in the transition process. From the results of the present work, some factors seem to be interesting, as the disturbance amplitude and disturbance spectra. It is known that the wall temperature have an important influence on the stability in the compressible boundary layer, at subsonic Mach numbers there are no works of this kind for wave packets. In Chapter 6, it were presented preliminary results for transition generated by white noise, a more deep investigation can be done for this problem, considering several random perturbations and performing some local analysis techniques. Also, the impact of low level white noise disturbance on the wave packet evolution may help to link features of nonlinear stages observed in wave packet with natural transition.

Bibliography

- [1] 2decomp&fft. <http://www.2decomp.org/>.
- [2] J. Anderson. *Hypersonic and High Temperature Gas Dynamics*. AIAA Education, 1989.
- [3] Knut H. Bech, Dan S. Henningson, and Ruud A. W. M. Henkes. Linear and nonlinear development of localized disturbances in zero and adverse pressure gradient boundary-layers. *Physics of Fluids*, 10(6), 1998.
- [4] Leandro F. Bergamo, Elmer M. Gennaro, Vassilis Theofilis, and Marcello A.F. Medeiros. Compressible modes in a square lid-driven cavity. *Aerospace Science and Technology*, 44:125 – 134, 2015. Instability and Control of Massively Separated Flows.
- [5] Leandro Fernandes BERGAMO. Instabilidade hidrodinamica linear do escoamento compressivel em uma cavidade. Master’s thesis, Universidade de Sao Paulo, Escola de Engenharia de São Carlos, Universidade de São Paulo, 2013.
- [6] F. P. Bertolotti, T. Herbert, and P. R. Spalart. Linear and nonlinear stability of the Blasius boundary layer. *J. Fluid Mech.*, 242:441–474, 1992.
- [7] H. Bestek, A. Thumm, and H. Fasel. *Thirteenth International Conference on Numerical Methods in Fluid Dynamics: Proceedings of the Conference Held at the Consiglio Nazionale delle Ricerche Rome, Italy, 6–10 July 1992*, chapter Direct numerical simulation of the three-dimensional breakdown to turbulence in compressible boundary layers, pages 145–149. Springer Berlin Heidelberg, Berlin, Heidelberg, 1993.
- [8] V I Borodulin, Y S Kachanov, and D B Koptsev. Experimental study of resonant interactions of instability waves in a self-similar boundary layer with an adverse pressure gradient: I. tuned resonances. *Journal of Turbulence*, 3:N62, 2002.
- [9] V I Borodulin, Y S Kachanov, D B Koptsev, and A P Roschekhtayev. Experimental study of resonant interactions of instability waves in self-similar boundary layer with an adverse pressure gradient: Ii. detuned resonances. *Journal of Turbulence*, 3:N63, 2002.
- [10] LUCA BRANDT, PHILIPP SCHLATTER, and DAN S. HENNINGSON. Transition in boundary layers subject to free-stream turbulence. *Journal of Fluid Mechanics*, 517:167–198, 9 2004.
- [11] Kenneth S. Breuer, Jacob Cohen, and Joseph H. Haritonidis. The late stages of transition induced by a low-amplitude wavepacket in a laminar boundary layer. *J. Fluid Mech.*, 340:395–411, 1997.
- [12] Chau-Lyan Chang, Mujeeb Malik, Gordon Erlebacher, and M. Hussaini. *Compressible stability of growing boundary layers using parabolized stability equations*. Fluid Dynamics and Co-located Conferences. American Institute of Aeronautics and Astronautics, June 1991. doi:10.2514/6.1991-1636.

- [13] J. Cohen. The initial evolution of a wave packet in a boundary layer. *Phys. Fluids*, 6(3):1133–1143, March 1994.
- [14] J. Cohen, K. S. Breuer, and J. H. Haritonidis. On the evolution of a wave packet in a laminar boundary layer. *J. Fluid Mech.*, 225:575–606, 1991.
- [15] W. O. Criminale, T. L. Jackson, and R. D. Joslin. *Theory and Computation in hydrodynamic stability*. Cambridge University Press, 2003.
- [16] I. B. de Paula, W. Würz, E. Krämer, V. I. Borodulin, and Y. S. Kachanov. Weakly nonlinear stages of boundary-layer transition initiated by modulated tollmien schlichting waves. *Journal of Fluid Mechanics*, 732:571–615, 10 2013.
- [17] Shutian Deng, Jiangang Cai, Hua Shan, and Chaoqun Liu. *DNS for K- and H-Type flow transition over a flat plate*. Aerospace Sciences Meetings. American Institute of Aeronautics and Astronautics, January 2005. doi:10.2514/6.2005-666.
- [18] Paolo Dini, MICHAEL S SELIG, and MARK D MAUGHMER. Simplified linear stability transition prediction method for separated boundary layers. *AIAA journal*, 30(8):1953–1961, 1992.
- [19] El-Hady Nabil M. Spatial three-dimensional secondary instability of compressible boundary-layer flows. *AIAA Journal*, 29(5):688–696, 1991. doi: 10.2514/3.10642.
- [20] H. Fasel. Investigation of the stability of boundary layers by a finite-difference model of the Navier-Stokes equations. *J. Fluid Mech.*, 78:355–383, 1976.
- [21] H. Fasel. Numerical simulation of nonlinear growth of wave packets in a boundary layer. In T. Tatsumi, editor, *Turbulence and Chaotic Phenomena in Fluids*. IUTAM, Elsevier, 1984.
- [22] H. Fasel and U. Konzelmann. Non-parallel stability of a flat-plate boundary layer using the complete Navier-Stokes equations. *J. Fluid Mech.*, 221:311–347, 1990.
- [23] HERMANN F. FASEL. Numerical investigation of the interaction of the klebanoff-0mode with a tollmien-schlichting wave. *Journal of Fluid Mechanics*, 450:1–33, 1 2002.
- [24] Alexander Fedorov. Transition and stability of high-speed boundary layers. *Annual Review of Fluid Mechanics*, 43:79–95, 2011.
- [25] Eric Forgoston and Anatoli Tumin. Three-dimensional wave packets in a compressible boundary layer. *Physics of Fluids*, 18(10), 2006.
- [26] Kenneth J. Franko and Sanjiva K. Lele. Breakdown mechanisms and heat transfer overshoot in hypersonic zero pressure gradient boundary layers. *Journal of Fluid Mechanics*, 730:491–532, 9 2013.
- [27] S. A. Gaponov, A. D. Kosinov, A. A. Maslov, and I. V. Semenov. Development of small perturbations in a slightly nonparallel supersonic flow. *Journal of Applied Mechanics and Technical Physics*, 23(3):398–401, 1982.
- [28] M. Gaster. A theoretical model of a wave packet in the boundary layer on a flat plate. *Proc. R. Soc. London A*, 347:271–289, 1975.
- [29] M. Gaster and I. Grant. An experimental investigation of the formation and development of a wavepacket in a laminar boundary layer. *Proc. Royal Soc. of London A*, 347:253–269, 1975.

- [30] Michael Gaster. *New Approaches and Concepts in Turbulence*, chapter The Origins of Turbulence, pages 235–250. Birkhäuser Basel, Basel, 1993.
- [31] Robert M. Kirby II George Em Karniadakis. *Parallel Scientific Computing in C++ and MPI: A Seamless Approach to Parallel Algorithms and their Implementation*. Cambridge University Press, 1st edition edition, 2003.
- [32] R. D. Joslin, C. L. Streett, and C.-L. Chang. 1993.
- [33] Yu. S. Kachanov. On the resonant nature of the breakdown of a laminar boundary layer. *J. Fluid Mech.*, 184:43–74, 1987.
- [34] Yu. S. Kachanov. Physical mechanisms of laminar boundary layer transition. *Ann. Rev. Fluid Mech.*, 26:411–482, 1994.
- [35] Yu. S. Kachanov, V. V. Kozlov, and V. Ya. Levchenko. Nonlinear development of waves in a boundary layer. *Izv. Akad. Nauk SSSR, Mekh. Zhidk. Gaza*, 3:49–53, 1977. In Russian.
- [36] Yu. S. Kachanov and V. Ya. Levchenko. The resonant interaction of disturbances at laminar-turbulent transition in a boundary layer. *J. Fluid Mech.*, 138:209–247, 1984.
- [37] Ünver Kaynak and Emre Gürdamar. *Boundary-Layer Transition Under the Effect of Compressibility for the Correlation Based Transition Model*. Aerospace Sciences Meetings. American Institute of Aeronautics and Astronautics, January 2008. doi:10.2514/6.2008-774.
- [38] A. V. Kazakov, M. N. Kogan, and V. A. Kuparev. The stability of the subsonic boundary layer during heating of the surface of a flat plate near the leading edge. *Fluid Dynamics*, 20(3):394–398, 1985.
- [39] P. S. Klebanoff, K. D. Tidstrom, and L. M. Sargent. The three-dimensional nature of boundary layer instability. *J. Fluid Mech.*, 12:1–34, 1962.
- [40] U. Konzelmann and H. Fasel. Numerical simulation of a three-dimensional wave packet in a growing flat plate boundary layer. In *Boundary layer Transition and Control*, pages 24.1–24.11, Cambridge – UK, 1991. The Royal Aeronautical Society.
- [41] Takuji Kurotaki, Takahiro Sumi, Takashi Atobe, and Jun Hiyama. *Numerical Simulation around Airfoil with Natural Transition in High Reynolds Numbers*. Fluid Dynamics and Co-located Conferences. American Institute of Aeronautics and Astronautics, June 2007. doi:10.2514/6.2007-3841.
- [42] lapack. <http://www.netlib.org/lapack/>.
- [43] S. K. Lele. Compact finite difference schemes with spectral-like resolution. *J. Comp. Phys.*, 103:16–42, 1992.
- [44] Zhining Liu, Wei Zhao, Chaoqun Liu, Zhining Liu, Wei Zhao, and Chaoqun Liu. *Direct numerical simulation of transition in a subsonic airfoil boundary layer*. Aerospace Sciences Meetings. American Institute of Aeronautics and Astronautics, January 1997. doi:10.2514/6.1997-752.
- [45] Leslie Mack. Linear Stability Theory and the Problem of Supersonic Boundary- Layer Transition. *AIAA Journal*, 13(3):278–289, 1975. doi: 10.2514/3.49693.
- [46] Leslie M. Mack. *Stability of Time Dependent and Spatially Varying Flows: Proceedings of the Symposium on the Stability of Time Dependent and Spatially Varying Flows Held August 19–23, 1985, at NASA Langley Research Center, Hampton, Virginia*, chapter Review of Linear Compressible Stability Theory, pages 164–187. Springer New York, New York, NY, 1987.

- [47] J.-P. Marec. *Aerodynamic Drag Reduction Technologies: Proceedings of the CEAS/DragNet European Drag Reduction Conference, 19–21 June 2000, Potsdam, Germany*, chapter Drag Reduction: a Major Task for Research, pages 17–27. Springer Berlin Heidelberg, Berlin, Heidelberg, 2001.
- [48] Andres G. Martinez, Elmer M. Gennaro, and Marcello A.F. Medeiros. Wavepackets in boundary layers close to transonic speeds. *Procedia IUTAM*, 14:374 – 380, 2015. IUTAM-ABCM Symposium on Laminar Turbulent Transition.
- [49] J. A. Masad and A. H. Nayfeh. Effect of heat transfer on the subharmonic instability of compressible boundary layers. *Physics of Fluids A*, 3(9):2148–2163, 1991.
- [50] CHRISTIAN S. J. MAYER, DOMINIC A. VON TERZI, and HERMANN F. FASEL. Direct numerical simulation of complete transition to turbulence via oblique breakdown at mach 3. *Journal of Fluid Mechanics*, 674:5–42, 5 2011.
- [51] CHRISTIAN S. J. MAYER, STEFAN WERNZ, and HERMANN F. FASEL. Numerical investigation of the nonlinear transition regime in a mach 2 boundary layer. *Journal of Fluid Mechanics*, 668:113–149, 2 2011.
- [52] M. A. F. Medeiros. The nonlinear evolution of a wavetrain emanating from a point source in a boundary layer. *J. Fluid Mech.*, 508:287–317, 2004.
- [53] M. A. F. Medeiros and M. Gaster. The influence of phase on the nonlinear evolution of wavepackets in boundary layers. *J. Fluid Mech.*, 397:259–283, 1999.
- [54] M. A. F. Medeiros and M. Gaster. The production of sub-harmonic waves in the nonlinear evolution of wavepackets in boundary layers. *J. Fluid Mech.*, 399:301–318, 1999.
- [55] Marcello A.F. Medeiros, Julio R. Meneghini, Homero Ghioti da Silva, and Marcello A.F. Medeiros. Iutam abcm symposium on laminar turbulent transition nonlinear spanwise modulated waves in channel flow. *Procedia IUTAM*, 14:355 – 363, 2015.
- [56] Parviz Moin and Krishnan Mahesh. Direct numerical simulation: a tool in turbulence research. *Annual review of fluid mechanics*, 30(1):539–578, 1998.
- [57] Lian L. Ng and Gordon Erlebacher. Secondary instabilities in compressible boundary layers. *Physics of Fluids A*, 4(4):710–726, 1992.
- [58] Xavier Normand and Marcel Lesieur. Direct and large-eddy simulations of transition in the compressible boundary layer. *Theoretical and Computational Fluid Dynamics*, 3(4):231–252, 1992.
- [59] Holger Opfer. *Active cancellation of 3D Tollmien-Schlichting waves in the presence of sound and vibrations*. PhD thesis, DLR, 2002.
- [60] Serkan Özgen and Senem Atalayer Kircali. Linear stability analysis in compressible, flat-plate boundary-layers. *Theoretical and Computational Fluid Dynamics*, 22(1):1–20, 2007.
- [61] Sergio Pirozzoli, Matteo Bernardini, and Francesco Grasso. Direct numerical simulation of transonic shock/boundary layer interaction under conditions of incipient separation. *Journal of Fluid Mechanics*, 657:361–393, 8 2010.
- [62] T. J. Poinot and S. K. Lele. Boundary conditions for direct simulations of compressible viscous flows. *Journal of Computational Physics*, 101:104–129, 1992.

- [63] O. Reynolds. On the experimental investigation of the circumstances which determine whether the motion of water shall be direct or sinuous, and the law of resistance in parallel channels. *Phil. Trans. Roy. Soc.*, 174:935–982, 1883.
- [64] Pierre Ricco, Duc-Luan Tran, and Ganda Ye. Wall heat transfer effects on klebanoff modes and tollmien schlichting waves in a compressible boundary layer. *Physics of Fluids*, 21(2), 2009.
- [65] PIERRE RICCO and XUESONG WU. Response of a compressible laminar boundary layer to free-stream vortical disturbances. *Journal of Fluid Mechanics*, 587:97–138, 9 2007.
- [66] U. Rist and H. Fasel. Direct numerical simulation of controlled transition in a flat plate boundary layer. *J. Fluid Mech.*, 298:211–248, 1995.
- [67] Taraneh Sayadi, Curtis W. Hamman, and Parviz Moin. Direct numerical simulation of complete h-type and k-type transitions with implications for the dynamics of turbulent boundary layers. *Journal of Fluid Mechanics*, 724:480–509, 6 2013.
- [68] H. Schlichting. Zur Entstehung der Turbulenz bei der Plattenströmung. In *Math. Phys. Klasse*, pages 182–208. Mitt. Nachr. Ges. Wiss. Göttingen, 1933.
- [69] Herrmann Schlichting and Klaus Gersten. *Boundary-layer theory*. Springer Science & Business Media, 2003.
- [70] Peter J. Schmid and Dan S. Henningson. *Stability and transition in shear flows*. Springer-Verlag, 2001.
- [71] P.J. Schmid and D. S. Henningson. A new mechanism for rapid transition involving a pair of oblique waves. *Phys. Fluids A*, 9:1986–1989, 1992.
- [72] Steven P Schneider. Effects of high-speed tunnel noise on laminar-turbulent transition. *Journal of Spacecraft and Rockets*, 38(3):323–333, 2001.
- [73] G. B. Schubauer and H. K. Skramstad. Laminar boundary layer oscillations and transition on a flat plate. Technical report, NACA Rep.909, April 1943.
- [74] N. V. Semionov, A. D. Kosinov, and A. A. Maslov. *Transition Control of Supersonic Boundary Layer on Flat Plate*, pages 323–328. Springer Netherlands, Dordrecht, 1999.
- [75] T.K. Sengupta, A. Dipankar, and A. Kameswara Rao. A new compact scheme for parallel computing using domain decomposition. *Journal of Computational Physics*, 220(2):654 – 677, 2007.
- [76] Michael Severin. Direct numerical simulations of three-dimensional wavepackets in a flat-plate boundary-layer. Master’s thesis, University of Arizona, 2012.
- [77] F. N. Shaikh. Investigation of transition to turbulence using white noise excitation and local analysis techniques. *J. Fluid Mech.*, 348:29–83, 1997.
- [78] B. SINGER, J. FERZIGER, and H. REED. *Investigation of the effects of initial disturbances on plane channel transition*. Aerospace Sciences Meetings. American Institute of Aeronautics and Astronautics, January 1986. doi:10.2514/6.1986-433.
- [79] Jayahar Sivasubramanian and Hermann F. Fasel. Numerical investigation of the development of three-dimensional wavepackets in a sharp cone boundary layer at mach 6. *Journal of Fluid Mechanics*, 756:600–649, 10 2014.

- [80] Jayahar Sivasubramanian and Hermann F. Fasel. Direct numerical simulation of transition in a sharp cone boundary layer at mach 6: fundamental breakdown. *Journal of Fluid Mechanics*, 768:175–218, 4 2015.
- [81] P. R. Spalart and Kyung-Soo Yang. Numerical study of ribbon-induced transition in Blasius flow. *J. Fluid Mech.*, 178:345–365, 1987.
- [82] Stemmer Christian, Kloker Markus J., and Wagner Siegfried. Navier-Stokes Simulation of Harmonic Point Disturbances in an Airfoil Boundary Layer. *AIAA Journal*, 38(8):1369–1376, 2000. doi: 10.2514/2.1136.
- [83] J.J Thibert and D Arnal. A review of {ONERA} aerodynamic research in support of a future super-sonic transport aircraft. *Progress in Aerospace Sciences*, 36(8):581 – 627, 2000.
- [84] A. Thumm, W. Wolz, and H. Fasel. *Laminar-Turbulent Transition: IUTAM Symposium Toulouse/France September 11–15, 1989*, chapter Numerical Simulation of Spatially Growing Three-Dimensional Disturbance Waves in Compressible Boundary Layers, pages 303–308. Springer Berlin Heidelberg, Berlin, Heidelberg, 1990.
- [85] W. Tollmien. über die Entstehung der Turbulenz. In *Math. Phys. Klasse*, pages 21–44. Mitt. Nachr. Ges. Wiss. Göttingen, 1929.
- [86] ANATOLI TUMIN. Three-dimensional spatial normal modes in compressible boundary layers. *Journal of Fluid Mechanics*, 586:295–322, 9 2007.
- [87] Adam P. Tunney, James P. Denier, Trent W. Mattner, and John E. Cater. A new inviscid mode of instability in compressible boundary-layer flows. *Journal of Fluid Mechanics*, 785:301–323, 12 2015.
- [88] J. van Ingen. *The eN Method for Transition Prediction. Historical Review of Work at TU Delft*. Fluid Dynamics and Co-located Conferences. American Institute of Aeronautics and Astronautics, June 2008. doi:10.2514/6.2008-3830.
- [89] B. R. Vasudeva. Boundary-layer instability experiment with localized disturbance. *Journal of Fluid Mechanics*, 29:745–763, 9 1967.
- [90] Miguel R Visbal and Datta V Gaitonde. On the use of higher-order finite-difference schemes on curvilinear and deforming meshes. *Journal of Computational Physics*, 181(1):155 – 185, 2002.
- [91] B. Wasistho, B.J. Geurts, and J.G.M. Kuerten. Simulation techniques for spatially evolving instabilities in compressible flow over a flat plate. *Computers and Fluids*, 26(7):713 – 739, 1997.
- [92] Frankl White. *Vicous Fluid Flow*. McGraw-Hill, 1974.
- [93] X. Wu, P. A. Stewart, and S. J. Cowley. On the catalytic role of the phase locked interaction of tollmien schlichting waves in boundary-layer transition. *J. Fluid Mech.*, 590:265 –294, 2007.
- [94] Xuesong Wu and Philip A Stewart. Interaction of phase-locked modes: a new mechanism for the rapid growth of three-dimensional disturbances. *Journal of Fluid Mechanics*, 316:335–372, 1996.
- [95] Kyung-Soo Yang, Philippe R. Spalart, and Joel H. Ferziger. Numerical studies of natural transition in a decelerating boundary layer. *Journal of Fluid Mechanics*, 240:433–468, 7 1992.
- [96] K. S. Yeo, X. Zhao, Z. Y. Wang, and K. C. Ng. DNS of wavepacket evolution in a Blasius boundary layer. *J. Fluid Mech.*, 652:333–372, 2010.

- [97] Lian Yongsheng and Shyy We. Laminar - Turbulent Transition of a Low Reynolds Number Rigid or Flexible Airfoil. *AIAA Journal*, 45(7):1501–1513, 2007. doi: 10.2514/1.25812.